UNIVERSITEIT VAN PRETORIA
UNIVERSITY OF PRETORIA
YUNIBESITHI YA PRETORIA

PATTERN SYNTHESIS AND DESIGN OF A MICROSTRIP WIRE GRID MONOPULSE ANTENNA

by

Reinart Johan Moraal

Submitted in partial fulfilment of the requirements for the degree
Master of Engineering (Electronic Engineering)

in the

Department of Electrical, Electronic and Computer Engineering
Faculty of Engineering, Built Environment and Information Technology

UNIVERSITY OF PRETORIA

October 2016

SUMMARY

PATTERN SYNTHESIS AND DESIGN OF A MICROSTRIP WIRE GRID MONOPULSE ANTENNA

by

Reinart Johan Moraal

Supervisor: Prof J. Joubert

Co-supervisor: Prof J.W. Odendaal

Department: Electrical, Electronic and Computer Engineering

University: University of Pretoria

Degree: Master of Engineering (Electronic Engineering)

Keywords: Microstrip, wire, grid, array, sequential, quadratic, programme, genetic, algorithm, monopulse, antenna.

The design of a monopulse microstrip wire grid antenna array is presented with simultaneously low side lobe levels in the sum pattern as well as both azimuth difference and elevation difference patterns. Monopulse antennas are a class of antennas used for direction finding in radar systems, and the control of side lobe levels is important to help with clutter rejection. The microstrip wire grid array is ideally suited to monopulse applications, and it has been shown in the literature that side lobes can be lowered by implementing an excitation taper across the aperture. Although it has been demonstrated in the literature that side lobes could be lowered for the sum pattern by applying a Taylor taper to the element excitation, it has not been shown that the antenna can be designed to produce an exact side lobe level. This work develops a synthesis method to design an excitation taper that would produce simultaneously low side lobes for the sum and both difference patterns. The resulting side lobe levels are a compromise between the patterns, since it is not possible to have arbitrarily low side lobe levels in all the antenna patterns without using complex feed structures and incorporating sub-arraying. This is true for monopulse antennas in general. The result of this work shows that it is quite difficult to achieve an exact side lobe requirement with a specific excitation taper, since mutual

coupling and the current distribution at the feed affect the current distribution across the entire antenna in different ways depending on the antenna mode, or pattern generated.

LIST OF ABBREVIATIONS

AZ	Azimuth
CST	Computer Simulation Technology
EL	Elevation
EM	Electromagnetic
FFT	Fast Fourier Transform

TABLE OF CONTENTS

LIST OF FIGURES

LIST OF TABLES

CHAPTER 1 INTRODUCTION

1.1 PROBLEM STATEMENT

1.1.1 Context of the problem

Monopulse antennas are a class of antennas used mainly in radar for angular measurements towards the target. The term monopulse refers to the concept that the angular measurements are made in a single radar sample, by comparing the response on multiple simultaneous antenna patterns. This is in contrast with other techniques such as sequential lobing or conical scanning, where the angular information is obtained by taking multiple samples at different times. The monopulse antenna basically performs angular measurements by comparing the received signal levels on a sum pattern and one or more difference patterns. Many antenna arrays such as microstrip patch arrays or slot arrays has been made into monopulse antennas, but one particularly interesting array, known as a microstrip wire grid array has received little attention in the literature. The microstrip wire grid array was first proposed by Kraus [1] in 1964, and involves the arraying of multiple wire loops in a “brick wall” formation. These wire loops can easily be adapted to microstrip by simply printing these loops on an appropriate substrate. This adaption to Kraus’s wire grid antenna was first proposed by Tuiri et al. [2]. Palmer [3] has proposed a method for the design of the microstrip grid array which results in optimum phasing to all the array elements, and yields larger bandwidths than what could be achieved by Kraus’s methods.

Pattern synthesis of monopulse antennas are of great importance, as unwanted side lobes can result in high levels of clutter entering the radar receiver. Conti et al. [4] has first shown that the microstrip wire grid antenna array can be used as a monopulse antenna, and a design was proposed where the side lobe levels of the sum channel was lowered by applying a Taylor amplitude taper to the radiating elements of the microstrip wire grid array. They did not design the aperture taper for a specific required side lobe level, but simply applied the aperture taper and lived with the resultant side lobe level. Since lowering the side lobes of the sum channel of a monopulse antenna usually leads to degraded side lobes in the difference patterns, many techniques has been proposed to

provide simultaneously low side lobes for the sum and difference patterns. These techniques usually rely on sub arraying [5] and [6]. There are however antenna arrays where the feed network does not allow the use of complex sub arrays, and where the difference patterns are obtained by feeding half of the antenna in phase, and the other half of the antenna in anti-phase. These monopulse antennas are known as two-section monopulse antennas, and the microstrip wire grid array fits into this category of monopulse antennas. McNamara [7] proposed a method to arrive at the optimum compromised sum and difference pattern side lobe levels for a monopulse antenna. He has shown that his optimization method works for simple equally spaced linear arrays, but did not apply the resultant weights for the element to any real antennas. Only linear array factor analysis was done to determine the side lobe levels that could be achieved.

1.1.2 Research gap

Little research has been done on the pattern synthesis of wire grid antenna arrays, especially when used as monopulse antennas. Conti et al. [4] has shown that it is possible to lower the side lobe levels of the sum pattern for a monopulse microstrip wire grid array antenna. However, no research was done on the feasibility of exact synthesis on side lobe levels. The only research on the simultaneous optimization of two-section monopulse patterns was done by McNamara [7]. This was shown to work for simple equally spaced linear arrays having only a sum and difference pattern, not complex two dimensional arrays of arbitrary arrangement and having a sum and two difference patterns.

1.2 APPROACH

The method that McNamara [7] proposed which is basically a sequential quadratic programme optimization is first expanded to work for 2D planar antenna arrays of arbitrary arrangement. The array factor for each pattern is determined, but the integrals to calculate the directivity for each pattern are done numerically. Also included in the quadratic programme is a simple expression for the element pattern. The sequential quadratic programme is extended to optimize side lobe levels in the sum and both difference patterns by having compromised constraints for each pattern. The quadratic programme and the weights for each pattern are then weighed and combined similar to what McNamara has

done for the simple equally spaced linear array. A simple genetic algorithm was implemented to perform the same optimization as a control. For the genetic algorithm, the cost function was not optimized, although simple adjustments were made to yield better results. Using three dimensional array factor analyses the side lobe levels for a monopulse antenna array are verified. A microstrip wire grid antenna with equal excitation is then designed using the methods proposed by Palmer [3]. Once the rough arrangement of the antenna array is known, the aperture excitation is determined that would result in the lowest simultaneous side lobe levels for the sum and difference patterns. The antenna elements that would result in the required excitation vector are derived and the tapered microstrip wire grid antenna is designed. The antenna is simulated using CST (Computer Simulation Technology) Studio Suite, which is a full wave 3D electromagnetic solver. The resultant side lobe levels are evaluated before a physical antenna is manufactured and measured.

1.3 RESEARCH GOALS

The goal of this research is to establish a way of designing amplitude tapers for two dimensional monopulse antenna arrays of arbitrary arrangement. A further goal is to determine the feasibility of applying this amplitude taper to a microstrip wire grid array by verifying the resultant side lobe levels that can be achieved.

1.4 RESEARCH CONTRIBUTION

This work aims to expand McNamara's work from the simple equally spaced linear array to a 2D antenna array of arbitrary arrangement, specifically aimed at the arrangement of a wire grid monopulse antenna array with a circular aperture, such as what could be used for the radar seeker in missiles. The work of Conti et al. [4] does not design an excitation taper for any required side lobe level. Rather a taper is specified and whatever resultant side lobe level was simply reported on. This excitation taper was also meant to lower the side lobe levels for the sum channel only. This work aims to design an aperture excitation taper that would result in the lowest simultaneous side lobe levels for the sum pattern as well as the azimuth and elevation difference patterns of a microstrip wire grid antenna with a circular aperture. Lastly, this work expands somewhat on the design methodology proposed by

Palmer [3]. Palmer only proposes design for phase relationships between what he calls modules. This work found that it is desirable to stay away from non-symmetrical modules and that for all two port modules, the dipole lengths are easily found by checking the resonant frequency of the module. The feed lines are then later adjusted for the phase relationships.

1.5 STRUCTURE OF THE DISSERTATION

Chapter 2 of this dissertation embarks on a literature study of monopulse antennas, the design of wire grid antenna arrays, and also antenna array factor analysis equations. It also gives information on how the sequential quadratic programme can be used to optimize the side lobe levels of a two-section linear monopulse array simultaneously. Lastly, the genetic algorithm is researched that will serve as the control optimization towards the sequential quadratic programme. Chapter 3 starts with the design of an equally excited monopulse microstrip wire grid antenna and shows the simulated results for input match and side lobe level. Next, the array factor and directivity expressions for a monopulse antenna are derived. These expressions are used to construct the sequential quadratic programme and genetic algorithms. Using these algorithms the same antenna geometry is used to optimize the side lobe levels. Deviations from the required side lobe levels and the resulting levels are shown. Lastly, a comparator network for the generation of the sum and two difference patterns is discussed, together with the construction of the final array. Chapter 4 deals with the simulated and measured results of the final monopulse microstrip wire grid antenna, while Chapter 5 discuss the differences observed between the realised side lobe levels and the required side lobe levels. Chapter 6 provides a conclusion to this dissertation.

CHAPTER 2 LITERATURE STUDY

2.1 INTRODUCTION

This chapter presents a literature study on monopulse antennas and their key properties. It also highlights the background and design of microstrip wire grid antennas. Lastly, two methods for the simultaneous optimization of side lobe levels for the sum and difference patterns of monopulse antennas are presented.

2.2 THE MONOPULSE ANTENNA

2.2.1 Two-section monopulse antennas

Monopulse is a radar measurement technique where the angular information of the target is found by comparing the measurements made from two or more simultaneous antenna patterns [8], p. 275. Shown in Figure 2.1 is a planar monopulse antenna, which can form sum, elevation difference and azimuth difference patterns. This antenna can be referred to as a two-section monopulse antenna, because the difference patterns are simply form when one half of the antenna is fed in anti-phase with the other half of the antenna [7]. Examining Figure 2.1 it can be seen that for a planar antenna generating sum and two orthogonal difference patterns, the antenna is divided into four quadrants. To generate a sum pattern, all four quadrants are fed in-phase. To generate the elevation difference pattern, quadrant *A* and *B* are fed in-phase, while quadrants *C* and *D* are fed in anti-phase. Lastly, to generate the azimuth difference pattern, quadrant *A* and *C* are fed in-phase, while quadrants *B* and *D* are fed in anti-phase. To calculate the angle towards a target, the radar needs to calculate what is known as the monopulse ratio. In amplitude comparison monopulse [8], p. 277 this monopulse ratio is simply the received power on one of the difference channels, divided by the received power by the sum channel. If this is done in both azimuth and elevation planes then the azimuth angle and elevation angle towards the target can be calculated. It is important to note that although the magnitude of the difference patterns are symmetrical around boresight (θ=0°), their phases are anti-symmetrical. For example, the phase of the azimuth pattern in the direction

(ϕ, θ) = (0, 10)° is 180° out of phase with the pattern in the direction (ϕ , θ) = (180,10)° even though their magnitudes are equal.

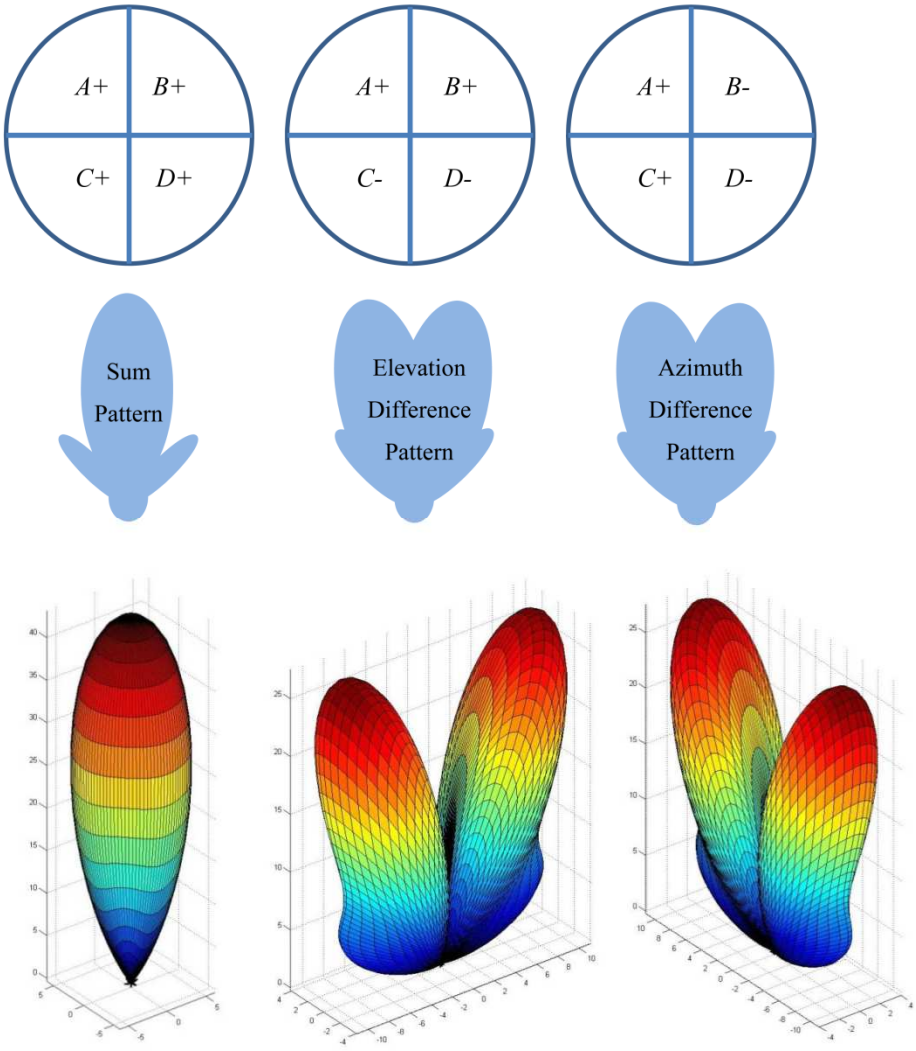

Figure 2.1. Antenna sum and difference patterns.

It is also easy to see that if the target is located at boresight (θ = 0°) then the monopulse ratio is zero, because the received power on the difference pattern is 0.

Figure 2.2 shows the monopulse ratio for either the azimuth or elevation difference plane of a typical monopulse antenna. The monopulse ratio is basically the received power of the difference pattern divided by the received power on the sum channel. Once the target measurements are made and the monopulse ratio is calculated, the angle towards the target

can be found by comparing the measurement result to the known monopulse ratio of the particular antenna.

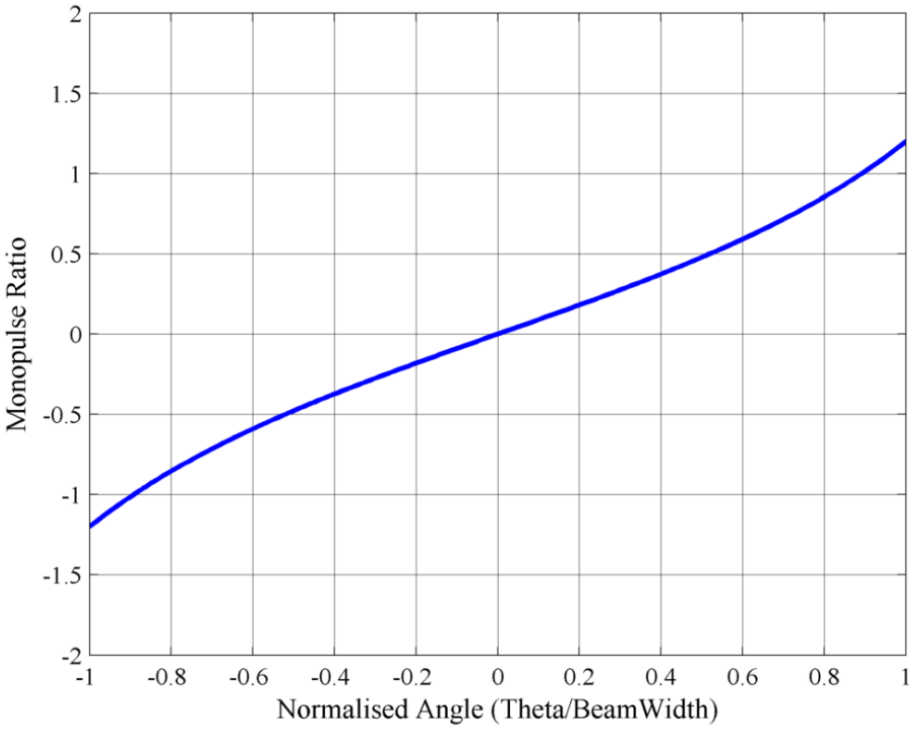

Figure 2.2. The monopulse ratio in a single plane.

2.2.2 The monopulse comparator

Many techniques exist to create the sum and difference patterns of a monopulse antenna simultaneously. One elegant technique is by the use of 90° hybrids formed into what is called a monopulse comparator [9]. The monopulse comparator can be thought of as a black box which on one side connects to the four antenna quadrants. On the other side of this black box are the three channels (sum, azimuth difference and elevation difference channels). When the comparator is fed on the sum channel, then all four antenna quadrants are excited in-phase. When the comparator is fed on the azimuth difference channel, then quadrants *A* and *C* are excited in anti-phase with quadrant *B* and *D*. Lastly, when the comparator is fed on the elevation difference channel, then quadrants *A* and *B* are fed in anti-phase with quadrants *C* and *D*.

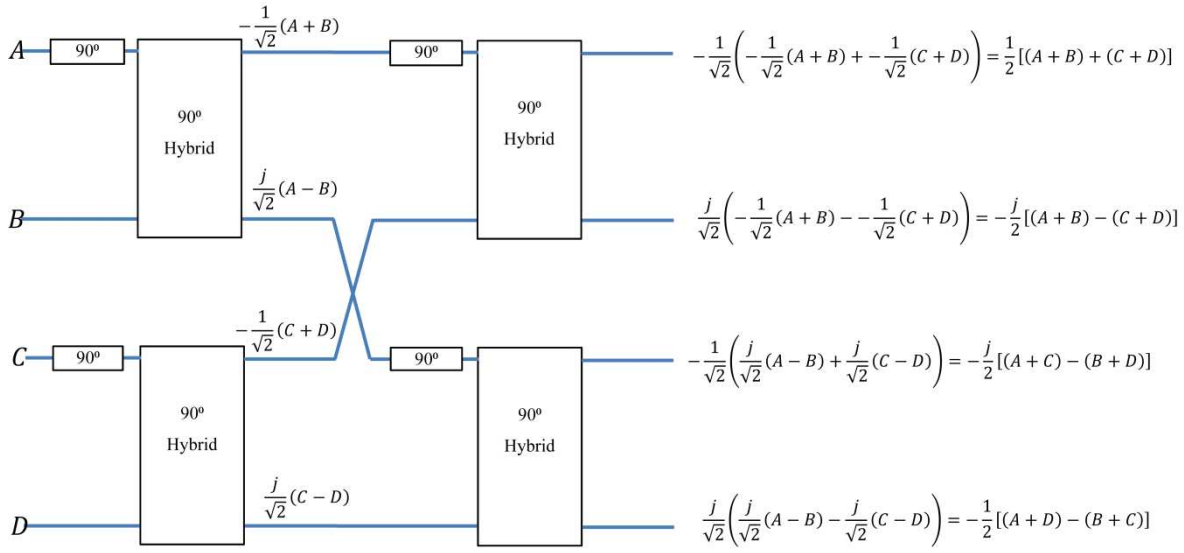

Figure 2.3. The block diagram of a monopulse comparator created from 90° hybrids.

The four antenna quadrants are connected on the left side of the monopulse comparator in Figure 2.3. On the right side are the three channels. The top port is the sum channel, second from top is the elevation difference channel and third is the azimuth difference channel. The last port is rarely used, and is known as the double difference channel. This port is usually just terminated.

2.3 THE MICROSTRIP WIRE GRID ANTENNA

Kraus [1] proposed an antenna configuration consisting of multiple loops of wire. For the resonant form of this antenna, the loops are arranged in a “brick wall” formation as shown in Figure 2.4.

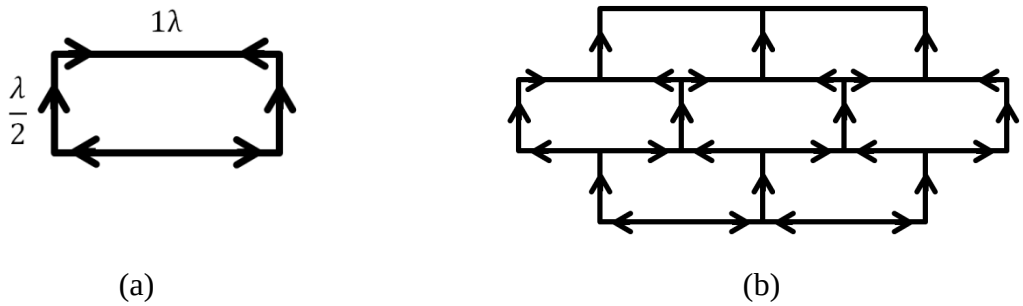

(a) (b)

Figure 2.4. The wire grid antenna as proposed by Kraus [1]. A single loop is shown in (a) while an array of loops in a brick wall configuration is shown in (b).

The dimensions of these loops are essentially one wavelength by half a wavelength and the arrows indicate the direction of the current flow. From this it is clear that the horizontal currents are opposite in sign, thereby cancelling the radiated far field caused by these currents. The vertical currents are always in the same direction as the loops are arrayed, and therefore their contribution to the far field is added. This type of antenna should therefore offer good co-polarization while having low cross-polarization.

The wire grid antenna can easily be adapted to microstrip, by printing the loops on a substrate. This implementation was first proposed by Tiuri et al. [2] and the conductors are then made of microstrip lines. The loop dimensions will then be one wavelength by half a wavelength in the substrate. The wire grid antenna is a very elegant array antenna, where the feed network is integrated with the antenna array which is entirely unlike other arrays such as an array of patch antennas, where a feed network needs to be designed to connect to all the patches in the array. Furthermore, Conti et al. [4] and later Hildebrandt [10] has shown that it is possible to synthesize the radiation pattern of the microstrip wire grid array, by adjusting the width of the vertical elements. In particular, Conti et al. [4] have presented a wire grid monopulse antenna, where the sum pattern had a Taylor illumination taper implemented on the width of the vertical elements, thereby achieving side lobes better than those that could be obtained with equal width, or equally excited vertical elements. Palmer [3] has shown that the radiation at all the discontinuities can be represented by an equivalent radiation resistance as shown in Figure 2.5. Since all these radiation resistances are spaced in multiples of half a wavelength around the wire grid

array, the input impedance to the wire grid array at any node is essentially the parallel sum of all the radiation resistances.

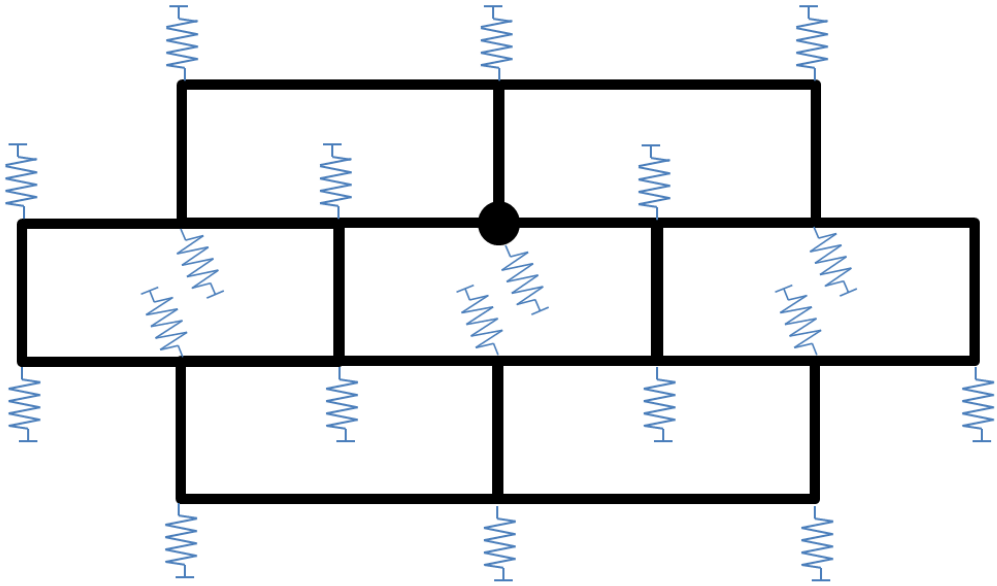

Figure 2.5. Radiation resistances at discontinuities of the wire grid antenna.

The same argument holds for the voltage level at each of these discontinuities or nodes. The magnitudes of the voltages at the nodes are all equal. Since the voltage magnitude is the same at all nodes, decreasing the radiation resistance at the discontinuities will mean that more power is radiated from that node.

The vertical conductors, when implemented in microstrip represent narrow patches fed by horizontal microstrip lines, which is usually much thinner than the vertical microstrip lines [3]. The radiation resistance of a microstrip patch is easily controlled by their widths and analytic models exist to determine the radiation resistance from microstrip patches [11], p.80. However, in general and for electrically thick substrates, a full wave code is required to determine the width of the patch for a given radiation resistance. Therefore, varying the widths of the vertical conductors should present an easy way of producing an amplitude taper across the aperture. Another source of radiation is the surface current of the vertical dipoles. Here, again, since the characteristic impedance of the conductor decreases with increasing conductor width, the current that flows in these lines will also increase with

increasing conductor width. This is because the voltage magnitudes at the nodes are equal across the microstrip wire grid array.

2.3.1 Narrow band design

Palmer [3] describes what he calls a narrow band design method. The basic idea is that instead of an array of loops, the microstrip wire grid array is seen as an array of wide vertical dipoles connected by narrow half wavelength microstrip lines. The design procedure can then be summarised as follows:

- Determine the dipole widths, so that the parallel sum of their radiation resistances equal the required antenna input impedance.
- Calculate the dipole lengths to be half a wavelength in the substrate.
- The width of the horizontal feeds can be chosen arbitrarily, although it was shown that the bandwidth improves if the characteristic impedance of these lines is as high as possible [3].
- Calculate the feed lengths so that their lengths are also half a wavelength in the substrate.

The problem with this design approach, as noted by Palmer [3] is that the fields are not well behaved in the vicinities of the discontinuities. So breaking the microstrip wire grid array into dipoles and horizontal feed arms leads to inaccurate phasing once the microstrip wire grid array is assembled. The problem is compounded when the substrate is electrically thick.

2.3.2 Broadband design

Instead of breaking up the microstrip wire grid array into wide vertical dipoles and narrow horizontal feed lines, Palmer [3] proposes to break up the microstrip wire grid array at the centres of the feed lines, therefore creating what he calls modules.

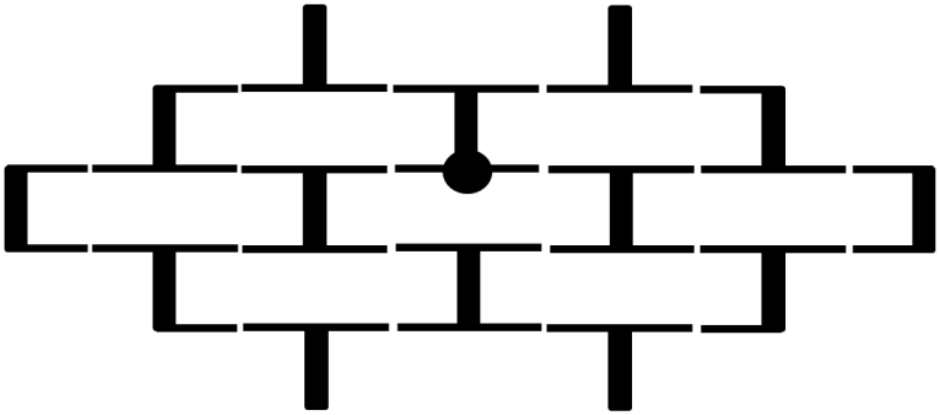

Figure 2.6. The microstrip wire grid array broken up into modules.

The phase is much better behaved at the centre of the feed lines than at the junction of the feed lines and the vertical dipoles. The design still first determines the module dipole widths based on the radiation resistances and the desired input impedance. The feed arms are still made as narrow as possible, but then each module is optimised on its own to provide the correct phasing between its ports. Specifically, Palmer proposes the H-module, the U-module, the T-module and the L-module.

2.3.2.1 The H-Module (Feed)

This module is shown in Figure 2.7 below. Here, the feed to the antenna is located at port 1. After the dipole and feed arm widths have been determined, the phasing of the s-parameters needs optimization as follows:

- $\angle S_{41}$ and $\angle S_{51}$ are equal,
- $\angle S_{21}$ and $\angle S_{31}$ are equal,
- the difference between $\angle S_{41}$ and $\angle S_{21}$ is 180°,
- the difference between $\angle S_{51}$ and $\angle S_{31}$ is 180°,
- $\angle S_{32}$ is 180°,
- $\angle S_{42}$ and $\angle S_{52}$ are 0°,
- $\angle S_{54}$ is 180°,
- $\angle S_{24}$ and $\angle S_{34}$ are 0°.

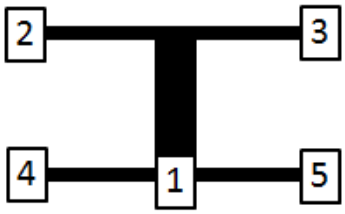

Figure 2.7. The H-module Feed.

For this module, it is not possible to satisfy all the above requirements and keep the module symmetrical. So a compromise between the requirements must be reached. It is however more important to satisfy the first two requirements above. If the first two requirements are not met, then the symmetry is lost between the top half of the array and the bottom half of the array. This will result in poor E-plane pattern performance, especially for larger arrays [3].

2.3.2.2 The H-module

The non-feed H-module is show in Figure 2.8. Here the module is symmetrical, and the optimization involves:

- $\angle S_{21}$ must be 180°,
- $\angle S_{31}$ and $\angle S_{41}$ must be 0°.

Figure 2.8. The H-module.

These objectives can easily be met for the non-feed H-module.

2.3.2.3 The T-module

Optimization of the T-module requires the phase of S_{21} to be 180°. The T-module is shown in Figure 2.9.

Figure 2.9. The T-module.

2.3.2.4 The U-module

Optimization of the U-module requires the phase of S_{21} to be 0°. The U-module is shown in Figure 2.10.

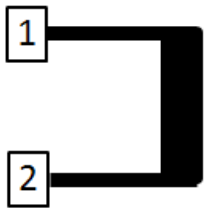

Figure 2.10. The U-module.

2.3.2.5 The L-module

Optimization of the L-Module requires the following relationships:

- $\angle S_{21}$ and $\angle S_{31}$ must be 0°,
- $\angle S_{32}$ and $\angle S_{23}$ must be 180°,
- $\angle S_{12}$ and $\angle S_{13}$ must be 0°,

Figure 2.11. The L-module.

2.3.2.6 Assembly of the complete wire grid antenna

After all the modules have been individually optimized, the wire grid antenna can be assembled. Because the modules will have differing horizontal dimensions, the feed can either be bent to fit it all together, or Palmer [3] suggests that the feed lengths for the centre modules can be constrained to those of the feed module, and only the dipole lengths are adjusted for the consequent modules.

2.3.3 Results of the module design approach

Palmer [3] reports good impedance bandwidth for his 9 element dipole array of around 17%. The array was manufactured on a λ/10 thick Styrofoam substrate with a unity relative dielectric constant (ε_r=1). The array has an efficiency of 82%. Good cross polarization is reported, however, the feed used in this electrically thick substrate severely degraded the expected side lobe levels.

2.4 ANTENNA ARRAY FACTOR

The Array Factor for a planar array with arbitrary element positions is given by [12], p.46:

$$AF(\theta,\phi) = \sum_{i=1}^{I} w_i e^{j\psi_i} \tag{2.1}$$

where:

w_i is the complex excitation weight of each antenna element

$\psi_i = k(x_i u + y_i v)$

x_i and y_i are the element positions

$u = sin\theta cos\phi$

$v = sin\theta sin\phi$

$k = \frac{2\pi}{\lambda_0}$

λ_0 is the free space wavelength

We can write (2.1) in matrix form as

$$AF(\theta,\phi) = J^T F_s \tag{2.2}$$

where J is a vector containing the element excitations and F_s is a vector containing the phase factors to each element due to their positions.

$$J = \begin{bmatrix} w_1 \\ w_2 \\ w_3 \\ \vdots \\ w_I \end{bmatrix} \tag{2.3}$$

$$F_s = \begin{bmatrix} e^{j\psi_1} \\ e^{j\psi_2} \\ e^{j\psi_3} \\ \vdots \\ e^{j\psi_I} \end{bmatrix} \tag{2.4}$$

The directivity is defined as the ratio of the power density in a specific direction, to the average power density [12] p.78. It is given as

$$D = 4\pi \frac{|AF(\theta,\phi)|^2}{\iint_{0\,0}^{2\pi\,\pi} |AF(\theta,\phi)|^2 sin\theta d\theta d\phi} \tag{2.5}$$

Since it is known that for any matrix M the magnitude square is equal to its outer product

$$|M|^2 = MM^T \tag{2.6}$$

We can write the power density term of (2.5) as

$$|AF(\theta,\phi)|^2 = J^T F_s (J^T F_s)^T = J^T F_s F_s^T J = J^T A J \tag{2.7}$$

We can then write equation (2.5) as

$$D = \frac{J^T A J}{\frac{1}{4\pi}\iint_{0\,0}^{2\pi\,\pi} J^T A J sin\theta d\theta d\phi} \tag{2.8}$$

Since J is constant, these can be taken out of the integrals and the equation for directivity becomes

$$D = \frac{J^T A J}{J^T \left(\frac{1}{4\pi}\iint_{0\,0}^{2\pi\,\pi} A sin\theta d\theta d\phi\right) J} \tag{2.9}$$

And if we define a matrix B as follows:

$$B = \frac{1}{4\pi} \int_0^{2\pi} \int_0^{\pi} A sin\theta d\theta d\phi \tag{2.10}$$

Then the equation for directivity can be written as the ratio of two quadratic hermetic forms as [13]:

$$D = \frac{J^T A J}{J^T B J} \tag{2.11}$$

2.5 SIMULTANEOUS PATTERN SYNTHESIS FOR TWO-SECTION MONOPULSE ARRAYS

In the last few years, many techniques have been investigated to optimize the sum and difference patterns of monopulse antennas. Weights designed from Taylor and Chebyshev distributions can be used for sum pattern synthesis, while McNamara has proposed the Zolotarev distribution for the synthesis of difference patterns [14]. Botha [15] outlines a procedure for the synthesis of difference patterns for arbitrarily shaped arrays based on the Zolotarev polynomials. Many techniques for the simultaneous synthesis of sum and difference patterns focus on sub-arraying such as what was done in [5] and [6]. There are however certain instances where sub-arraying is not feasible, because of space constraints with the feed network. The monopulse antennas of this class are known as a two-section monopulse, and the whole array is fed in phase to obtain the sum pattern. The difference patterns are obtained by feeding one half of the array 180 degrees out of phase with the other half [7]. McNamara [7] has shown that it is possible to use Sequential Quadratic Programming to optimize the sum and difference patterns for equally spaced linear two-section monopulse antennas. A more modern technique is the genetic algorithm which can be used for the optimization of many different problems. It can therefore also be used for the simultaneous optimization of sum and difference patterns for two-section monopulse antennas. More recently, Mohammed [16] has proposed a method where an iterative fast Fourier transform (FFT) is used to synthesize optimal sum and difference patterns, while

forcing some percentage of common element excitations on the difference patterns to obtain simultaneously low side lobe levels in the sum and difference patterns.

2.5.1 The sequential quadratic programme optimization

In equation (2.11) A and B are both hermitian, meaning $a_{mn}=a_{nm}$ and $b_{mn}=b_{nm}$. Furthermore, [13] has shown that $\boldsymbol{x}^T\boldsymbol{B}\boldsymbol{x} > 0$ for any x where x cannot be a zero vector, and therefore B is positive definite. Maximizing the directivity of the antenna array is equivalent to minimizing the quadratic quantity [17]

$$Q[J] = J^T B J - J^T F_0 \tag{2.12}$$

subject to constraints, where the constraints are the side lobe levels defined as follows

$$J^T(\pm F_s - cF_0) \leq 0 \tag{2.13}$$

Here, c is the side lobe level, and we make no assumption regarding the sign of the side lobe level in order to keep the constraints linear. $J^T F_0$ is the array factor value at its scan angle. Equation (2.13) shows that the array factor at any coordinate (ϕ,θ) should be less than the array factor at its scan angle (which is located at (0,0) for the sum pattern) multiplied by the constraint level. So, if 20 dB side lobe levels are required, c would be 0.01. Equations (2.12) and (2.13) can be solved by a Sequential Quadratic Programme.

Generally, any quadratic function $x^T M x + x^T b + c$ is strictly convex and has a unique global minimum when M is hermitian and positive definite. Since B is positive definite, equation (2.12) is convex and the minimum of $Q[J]$ is also a global minimum. McNamara [7] has shown that a multi-objective approach can work for 2 section linear arrays to minimize both sum and difference patterns. Specifically, minimizing the quadratic quantity

$$Q_{COMBINED}[J] = J^T B_{COMBINED} J - J^T F_{0\,COMBINED} \tag{2.14}$$

where

$$\begin{aligned} Q_{COMBINED}[J] &= \beta Q_{SUM}[J] + (1-\beta) Q_{DIFF}[J], \\ B_{COMBINED} &= \beta B_{SUM} + (1-\beta) B_{DIFF}, \\ F_{0\,COMBINED} &= \beta F_{0SUM} + (1-\beta) F_{0\,DIFF}. \end{aligned} \tag{2.15}$$

Here, β is a value between 0 and 1, and represents the relative weight of each quadratic quantity. McNamara has found that a value of 0.5 actually works the best, since the constraints are listed for each pattern of the monopulse antenna separately as:

$$J^T(\pm F_{SUM} - cF_{0SUM}) \leq 0 \qquad (2.16)$$
$$J^T(\pm F_{DIFF} - cF_{0DIFF}) \leq 0$$

2.5.2 The Genetic Algorithm

A more modern search and optimization method is the Genetic Algorithm. The basic flow of the Genetic Algorithm can be summarized as follows [18], p. 30:

- find the cost for each chromosome in the population,
- select mates,
- mating,
- mutation,
- convergence check.

2.5.2.1 Create an initial random population of chromosomes

Each chromosome in the population is basically a random excitation vector for the array. The directivity is evaluated over (ϕ, θ) for each chromosome in the population.

2.5.2.2 Find the cost for each chromosome in the population

The directivity of each chromosome in the population is then compared to a mask M over the (ϕ, θ) plane. A "penalty" or cost is given everywhere where the directivity for a particular chromosome exceeds the mask. The higher this cost, the worst choice the particular chromosome is. The way in which the penalty is calculated is known as the cost function, and is a very important driver in the performance of the Genetic Algorithm [19], p.83.

2.5.2.3 Mate Selection

The chromosomes in the population is ranked from lowest cost (best performing chromosomes to highest cost (worst performing chromosomes) [19], p.36. Then only a fraction of the best performing chromosomes is selected for mating, while the rest is discarded.

2.5.2.4 Mating

Pairs of chromosomes are first selected for mating from the pool of mates. Various ways of selecting mates can be implemented, like random pairing, tournament selection or top to bottom pairing [19], pp.38-40. “Offspring” is then produced from the mated pairs. In its simplest form, the offspring is generated by simply swapping out the genes of the two chromosomes [19], p.57. For instance, a given chromosome is the excitation vector J with 8 weights (or genes), while the mating chromosome is the excitation vector K also with 8 genes. A random amount of these genes are then simply swapped between vector K and J. Another method involves blending the genes between chromosomes J and K [19], p.57. A random variable β is defined between 0 and 1, and the genes of the offspring chromosome L are found as follows:

$$L = \beta J + (1 - \beta)K \tag{2.17}$$

2.5.2.5 Mutation

To avoid converging into a local minimum, a random amount of genes in the entire pool of offspring is mutated. Typically, the particular gene, or weight within the offspring excitation vector is replaced by a random weight [19], p.60.

2.5.2.6 Convergence Check

The mating pairs together with the newly formed offspring is then again evaluated for cost, as explained above, and the whole process is repeated indefinitely until either the cost function has reached convergence, or a maximum amount of iterations has been reached.

2.6 CHAPTER CONCLUSION

This chapter presented an overview of the current applicable theory on which the rest of this work is based. Important concepts presented are monopulse antennas in general and their uses, the history of the microstrip wire grid array antenna, a method for the design thereof and some basic array theory for the analysis of antenna arrays of arbitrary arrangement. The chapter concludes with two methods for the synthesis of antenna arrays. The sequential quadratic programme will be used further in this work to design an antenna, while the genetic algorithm will be used as a check.

CHAPTER 3 ANTENNA SYNTHESIS AND DESIGN

3.1 INTRODUCTION

This chapter outlines the design procedure for a tapered monopulse microstrip wire grid array. It starts off with the derivation of the monopulse array factor and directivity for 2D monopulse array of arbitrary geometry. Then, an equally excited monopulse microstrip wire grid antenna is designed. The analytical equations for array factor are then used to compare the radiation patterns calculated with the radiation patterns obtained from a full wave solution for the equally excited antenna. These equations are further used to develop the sequential quadratic programme and genetic algorithm for simultaneous optimization of the side lobes of the sum and two difference patterns. An antenna with a tapered excitation is then designed. Preliminary results of the excitation taper are given. Lastly, a comparator network is designed, and the final antenna construction is shown.

3.2 DERIVATION OF THE MONOPULSE ARRAY FACTOR AND DIRECTIVITY

A two-section monopulse antenna has some special characteristics that can be exploited. These antennas have an even number of elements, and they are symmetrical around the x and y axis of the antenna. This symmetry is applicable to element arrangement, as well as element excitation.

These antennas therefore have $4N$ elements, where N is the amount of elements in one quadrant. To start, expressions for the directivity of such a monopulse antenna will be created, for an antenna of 4 elements, or 1 element in each quadrant of the antenna. Such an antenna is shown Figure 3.1. Notice from this figure, that we can have element i as a real element, while $i1$, $i2$ and $i3$ are just mirror images of i around the principal axes of the monopulse antenna.

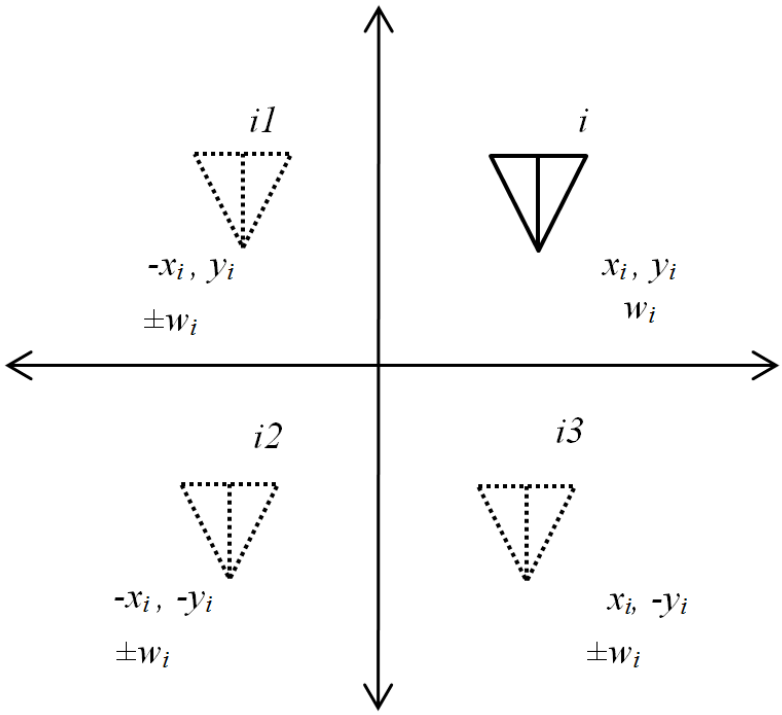

Figure 3.1. A Monopulse antenna with 1 element in each quadrant.

For the sum pattern, we have all element weights the same and the phase factor matrix can be written as:

$$J = \begin{bmatrix} w_i \\ w_i \\ w_i \\ w_i \end{bmatrix} \tag{3.1}$$

$$F_s = \begin{bmatrix} e^{jk(x_i u + y_i v)} \\ e^{-jk(x_i u - y_i v)} \\ e^{-jk(x_i u + y_i v)} \\ e^{jk(x_i u - y_i v)} \end{bmatrix} \tag{3.2}$$

The exponential terms of (3.2) can be rewritten by using the following identities, and if we replace kx_iu with α and ky_iv with β for simplicity of writing we obtain

$$e^{j(\alpha+\beta)} = e^{j\alpha}e^{j\beta} \tag{3.3}$$

and

$$e^{\pm j\alpha} = cos\alpha \pm jsin\alpha \tag{3.4}$$

Therefore

$$\begin{aligned} e^{j(\alpha+\beta)} &= (cos\alpha + jsin\alpha)(cos\beta + jsin\beta) \\ e^{-j(\alpha-\beta)} &= (cos\alpha - jsin\alpha)(cos\beta + jsin\beta) \\ e^{-j(\alpha+\beta)} &= (cos\alpha - jsin\alpha)(cos\beta - jsin\beta) \\ e^{j(\alpha-\beta)} &= (cos\alpha + jsin\alpha)(cos\beta - jsin\beta) \end{aligned} \tag{3.5}$$

Evaluating (2.2) with the above identities

$$J^T F_s = w_i e^{j(\alpha+\beta)} + w_i e^{-j(\alpha-\beta)} + w_i e^{-j(\alpha+\beta)} + w_i e^{j(\alpha-\beta)} \tag{3.6}$$

$$\begin{aligned} J^T F_s = w_i[&(cos\alpha + jsin\alpha)(cos\beta + jsin\beta) + (cos\alpha - jsin\alpha)(cos\beta + jsin\beta) \\ &+ (cos\alpha - jsin\alpha)(cos\beta - jsin\beta) \\ &+ (cos\alpha + jsin\alpha)(cos\beta - jsin\beta)] \end{aligned} \tag{3.7}$$

$$J^T F_s = w_i \begin{pmatrix} cos\alpha cos\beta + jsin\alpha cos\beta + jcos\alpha sin\beta - sin\alpha sin\beta + \\ cos\alpha cos\beta - jsin\alpha cos\beta + jcos\alpha sin\beta + sin\alpha sin\beta + \\ cos\alpha cos\beta - jsin\alpha cos\beta - jcos\alpha sin\beta - sin\alpha sin\beta + \\ cos\alpha cos\beta + jsin\alpha cos\beta - jcos\alpha sin\beta + sin\alpha sin\beta \end{pmatrix} \tag{3.8}$$

$$J^T F_s = 4w_i[cos\alpha cos\beta] \tag{3.9}$$

The expression for the sum pattern of the 4 element monopulse antenna is therefore.

$$AF_{SUM}(\theta, \phi) = 4w_i[cos(kx_i u)cos(ky_i v)] \tag{3.10}$$

The same reasoning can be used to find the difference patterns in the azimuth and elevation planes. For the azimuth difference pattern (2.2) is expanded as

$$J^T F_s = w_i e^{j(\alpha+\beta)} - w_i e^{-j(\alpha-\beta)} - w_i e^{-j(\alpha+\beta)} + w_i e^{j(\alpha-\beta)} \tag{3.11}$$

While for the elevation difference pattern (2.2) is expanded as

$$J^T F_s = w_i e^{j(\alpha+\beta)} + w_i e^{-j(\alpha-\beta)} - w_i e^{-j(\alpha+\beta)} - w_i e^{j(\alpha-\beta)} \tag{3.12}$$

It is easy to verify that these expressions reduce to the following expressions for the azimuth and elevation difference patterns of a 4 element monopulse array:

$$AF_{AZDIFF}(\theta,\phi) = 4jw_i[sin(kx_i u)cos(ky_i v)] \tag{3.13}$$

$$AF_{ELDIFF}(\theta,\phi) = 4jw_i[cos(kx_i u)sin(ky_i v)] \tag{3.14}$$

Extending this reasoning to planar array being symmetrical around the array centre in both azimuth and elevation planes, and having a total of $4N$ elements (where N is the amount of elements in a single quadrant) yields the array factors for the three modes of operation. These are given below as:

$$AF_{SUM}(\theta,\phi) = 4\sum_{n=1}^{N} w_n[cos(kx_n u)cos(ky_n v)] \tag{3.15}$$

$$AF_{AZDIFF}(\theta,\phi) = 4j\sum_{n=1}^{N} w_n[sin(kx_n u)cos(ky_n v)] \tag{3.16}$$

$$AF_{ELDIFF}(\theta,\phi) = 4j\sum_{n=1}^{N} w_n[cos(kx_n u)sin(ky_n v)] \tag{3.17}$$

If we look at equations (3.15) through (3.17), we can once again write them in the matrix form as was done with equations (2.2) through (2.4):

$$J = \begin{bmatrix} w_1 \\ w_2 \\ w_3 \\ w_4 \\ \vdots \\ w_N \end{bmatrix} \tag{3.18}$$

$$F_{SUM} = 4\begin{bmatrix} cos(kx_1u)cos(ky_1v) \\ cos(kx_2u)cos(ky_2v) \\ cos(kx_3u)cos(ky_3v) \\ cos(kx_4u)cos(ky_4v) \\ \vdots \\ cos(kx_Nu)cos(ky_Nv) \end{bmatrix} \tag{3.19}$$

$$F_{DAZ} = 4j\begin{bmatrix} sin(kx_1u)cos(ky_1v) \\ sin(kx_2u)cos(ky_2v) \\ sin(kx_3u)cos(ky_3v) \\ sin(kx_4u)cos(ky_4v) \\ \vdots \\ sin(kx_Nu)cos(ky_Nv) \end{bmatrix} \tag{3.20}$$

$$F_{DEL} = 4j\begin{bmatrix} cos(kx_1u)sin(ky_1v) \\ cos(kx_2u)sin(ky_2v) \\ cos(kx_3u)sin(ky_3v) \\ cos(kx_4u)sin(ky_4v) \\ \vdots \\ cos(kx_Nu)sin(ky_Nv) \end{bmatrix} \tag{3.21}$$

We can obtain the A matrix entries by calculating the outer product of equations (3.19) through (3.21)

$$a_{mn(sum)} = cos(kx_nu)cos(ky_nv)cos(kx_mu)cos(ky_mv) \tag{3.22}$$

$$a_{mn(daz)} = sin(kx_nu)cos(ky_nv)sin(kx_mu)cos(ky_mv) \tag{3.23}$$

$$a_{mn(del)} = cos(kx_nu)sin(ky_nv)cos(kx_mu)sin(ky_mv) \tag{3.24}$$

with m,n = 1,2,3,4…., and the entries to the B matrix given in (2.11) are then

$$b_{mn(sum)} = \frac{1}{4\pi}\int_0^{2\pi}\int_0^{\pi} a_{mn(sum)}\sin(\theta)\, d\theta d\phi \tag{3.25}$$

$$b_{mn(daz)} = \frac{1}{4\pi}\int_0^{2\pi}\int_0^{\pi} a_{mn(daz)}\sin(\theta)\, d\theta d\phi \tag{3.26}$$

$$b_{mn(del)} = \frac{1}{4\pi}\int_0^{2\pi}\int_0^{\pi} a_{mn(del)}\sin(\theta)\, d\theta d\phi \tag{3.27}$$

with m,n = 1,2,3,4….

Evaluation of the integrals given in equations (3.25) to (3.27) is best kept numerical. Computational power today is powerful enough to evaluate the integrals very quickly. This has the advantage that no assumption has to be made on the element arrangement. Of course there are rare element arrangements for which an exact solution to the integrals can be found, but in general only a numerical solution will exist for these integrals.

3.3 ANTENNA DESIGN FOR EQUAL EXCITATION

3.3.1 Antenna Requirements

The antenna requirements are briefly summarized below.

Antenna gain:	>23 dBi
Operating frequency:	18 GHz
Side Lobes:	As low as possible simultaneously in all patterns

3.3.2 Initial estimate on antenna size

At first we have to estimate the aperture size

$$A_e = \frac{{\lambda_0}^2}{4\pi} G \tag{3.28}$$

Here, λ_0 is the free space wavelength, A_e is the effective aperture, and G is the antenna gain.

From this we have an effective aperture of 4400 mm^2. The active area for a microstrip wire grid antenna confined within a circular area is roughly hexagonal. So to fit a hexagon with an area of 4400 mm^2 into a circle, the circle radius would need to be 42 mm. The above equation is valid for 100% aperture illumination efficiency. In [3] it was found that the radiation efficiencies of microstrip grid antennas are typically around 80%, so the effective aperture area is initially scaled by 1.25. This yields a circular area with a radius of 46mm.

3.3.3 Chosen Substrate

The substrate chosen is Rogers RT Duroid 5880 with a thickness of 0.787 mm. The main driver for the substrate choice is availability. RT Duriod has a relative dielectric constant of 2.2 and a loss tangent of 0.0009 at 10 GHz.

3.3.4 Initial estimate on dipole and feed arm arrangements

To start the layout of the geometry, the guided wavelength within the substrate must first be determined. At this stage, the feed arms widths will be chosen to have a characteristic impedance as high as possible, which can still be manufactured with good tolerances. This equates to line widths of 0.2 mm, or Z_0=154 Ω. The dipole widths are not possible at this stage to determine, since it is not known how many dipoles will fit into the antenna aperture. The amount of dipoles, together with the antenna input impedance will yield the dipole widths. Since the dipoles are wider than the feed arms, their guided wavelengths in the substrate should be a bit shorter. The guided wavelength of the feed arms is calculated to be 12.81 mm while the estimated guided wavelength of the dipoles is 12.3 mm. The result is shown in Figure 3.2.

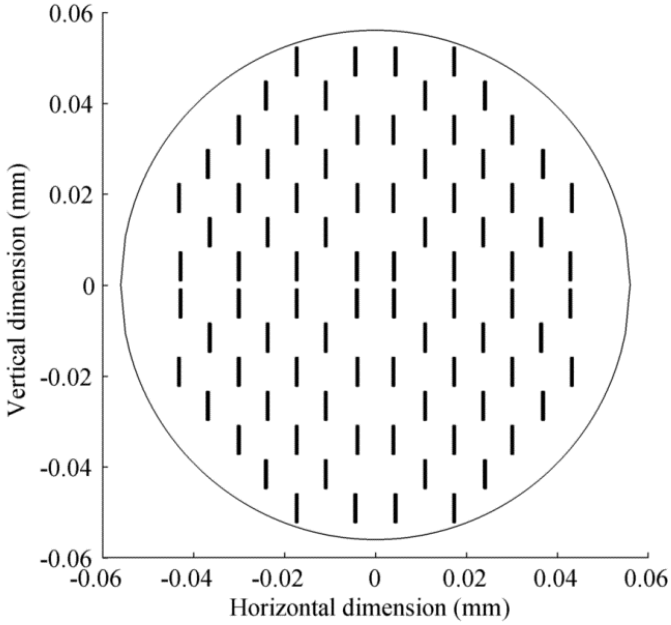

Figure 3.2. First estimate on the monopulse wire grid antenna.

Each quadrant contains 21 dipoles. The vertical spacing between the quadrants is initially set at 0.325λ and the horizontal spacing is set to 0.1λ. These values are based on the work done by [4]. Since each quadrant will be fed on its own, the input impedance for each quadrant must be 50 Ω. Therefore, the radiation resistance presented by each dipole is 21 x 50 Ω = 1050 Ω. The resonant length of the dipole and its corresponding radiation resistance is found by 3D electromagnetic simulation using CST. The geometry is shown in Figure 3.3. It was experimentally found that the measured resistance at the edge of the patch should be exactly half of the calculated radiation resistance presented by the dipole. This is done by feeding the patch with a piece of microstrip the same width as the feed arm width. The port extension is then adjusted so the measured impedance is at the edge of the patch. The resulting patch dimensions are then:

- Length: 5.335 mm
- Width: 1.663 mm

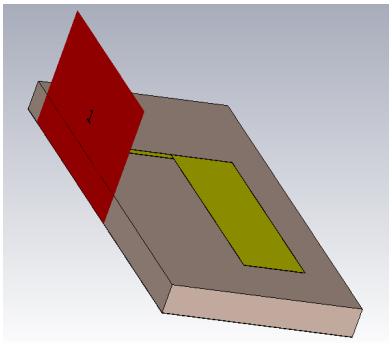

Figure 3.3. Determining the patch dimensions for free resonant length and radiation resistance.

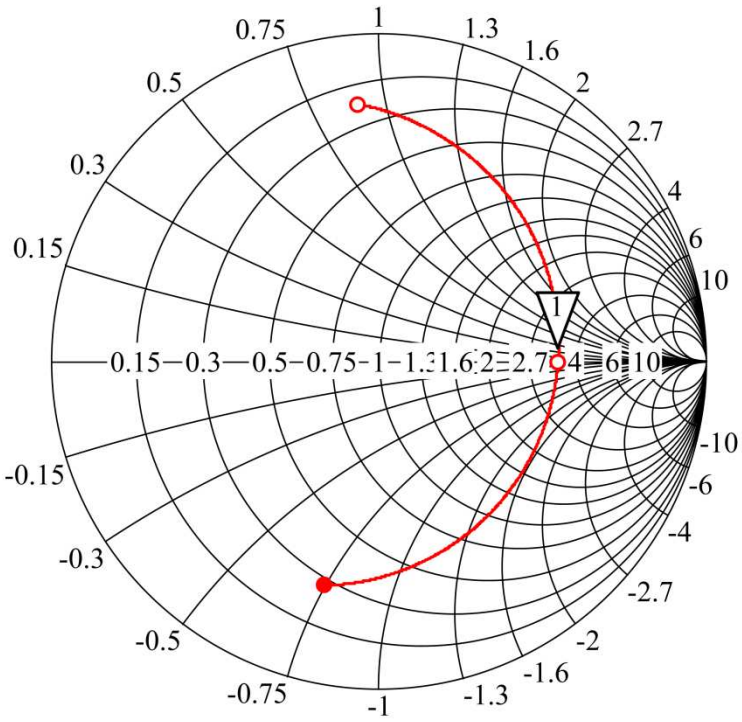

Figure 3.4. Resulting input impedance at the edge of the patch. (524.8 +j0) Ω, 18 GHz.

The next step is to construct the different modules that are going to be used in building up the entire grid array. The modules to be used will be:

- H-module (Feed),
- H-modules,
- T-modules,
- I-modules,
- U-modules.

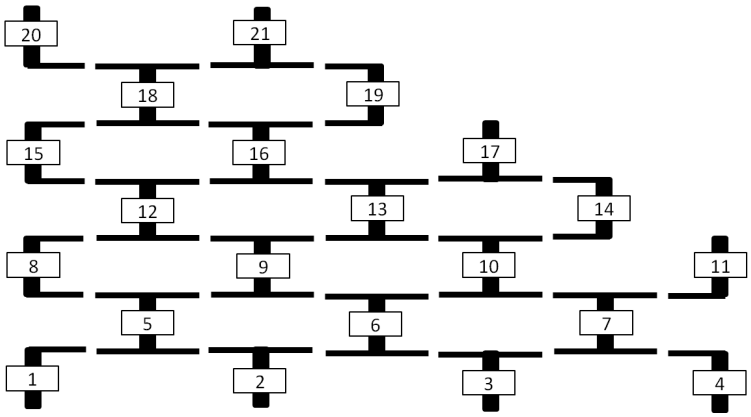

Figure 3.5. A single quadrant of the wire grid antenna broken into individual modules. The dipoles are numbered as indicated. The feed module is module 9.

This work has found that modules which are not symmetrical (like the feed module) cannot be optimized entirely, instead a compromise must always be found. Therefore, this work does not use the L-module as proposed by Palmer [3]. Instead, the L-module is made up from different combinations of U-modules, T-modules and a newly proposed module called the I-module. The I-modules are simply the same as the dipole fed by a quarter wave feed line as shown in Figure 3.3.

3.3.5 Module Design

3.3.5.1 H-module (Feed) design

This module is optimized first, since it was shown by [3] that phasing errors in the feed module has the most effect on the impedance bandwidth. This module also needs to be matched to the antenna. To do this, the antenna impedance needs to be represented at ports 2-5 as shown in Figure 3.6. The requirement for a 50 Ω impedance (Z_0) at port 1 means that port 2 and 3 should result in an impedance of 100 Ω at the top dipole edge, and port 4 and 5 should similarly result in an impedance of 100 Ω at port 1. These two 100 Ω impedances will then result in an impedance of 50 Ω presented at port 1. This effectively means that port 2-5 should present 200 Ω each to the module at the dipole top and bottom edges respectively. Since the feed arms are essentially quarter wave transformers with Z_0 equal to 154.1 Ω, we can use the quarter wave equation to determine the port impedances.

$$Z_{port} = \frac{Z_0^2}{Z_{dipole}} \tag{3.29}$$

Therefore, the port impedances are calculated to be 118.7 Ω.

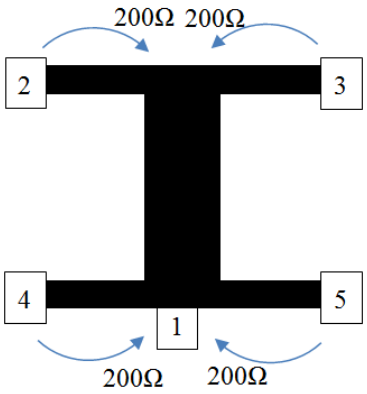

Figure 3.6. H-Module (feed) with presented port impedances at the dipole edges.

The way this is implemented in the CST environment is shown in in Figure 3.7. Ports 2 to 5 are waveguide ports, and the microstrip width is chosen so that Z_0 is 118.7 Ω. The lengths of these microstrip lines are 2 mm, and the port extension of ports 2-5 is also chosen as 2 mm.

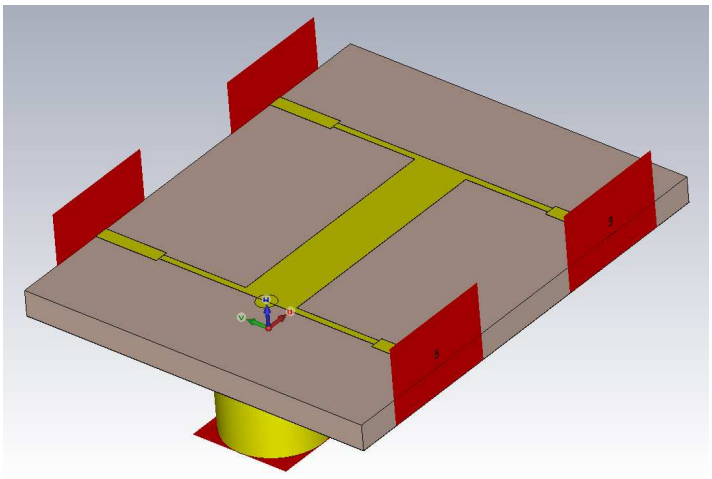

Figure 3.7. H-module (Feed) implemented in the CST environment. Port extensions equal the length of the 118.7 Ω microstrip lines.

The H-module must further be optimized so that the phase of the s-parameters is:

- $\angle S_{32}$ is equal to 180°,
- $\angle S_{42}$ and $\angle S_{52}$ are equal to 0°,
- $\angle S_{24}$ and $\angle S_{34}$ are equal to 0°,
- $\angle S_{54}$ is equal to 180°,
- $\angle S_{41}$ and $\angle S_{51}$ are equal, but 180° out of phase with $\angle S_{21}$ and $\angle S_{31}$.

To do this, the initial dimensions of the H-module need to be set. Since it is required to have an electrical length of 180° (which is 6.405 mm in the substrate for the feed arm) between port 1 and port 2, we have the initial feed arm length at

$$L_{feed} = \frac{\left(\frac{\lambda_{dielectric}}{2} - W_{dipole}\right)}{2}, \tag{3.30}$$

$$L_{feed} = \frac{\left(\frac{12.81mm}{2} - 1.677mm\right)}{2},$$

$$L_{feed} = 2.36mm.$$

Next, the length of the dipole is adjusted so that $\angle S_{41}$ and $\angle S_{51}$ are equal, but 180° out of phase with $\angle S_{21}$ and $\angle S_{31}$. The dipole and feed arm lengths are then further adjusted to meet the first 4 requirements. In reality it is impossible for this H-module to meet all 5 requirements, so a compromise must be reached. Using the optimizer of CST microwave studio, the module is optimized as much as possible to yield the phasing for Port1 as driving port:

$\angle S_{21}$	59.5°	Marker1
$\angle S_{31}$	59.4°	Marker2
$\angle S_{41}$	251.0°	Marker3
$\angle S_{51}$	251.0°	Marker4
Therefore, $\angle S_{21}$ - $\angle S_{41}$	191.5°	
Therefore, $\angle S_{31}$ - $\angle S_{51}$	191.6°	

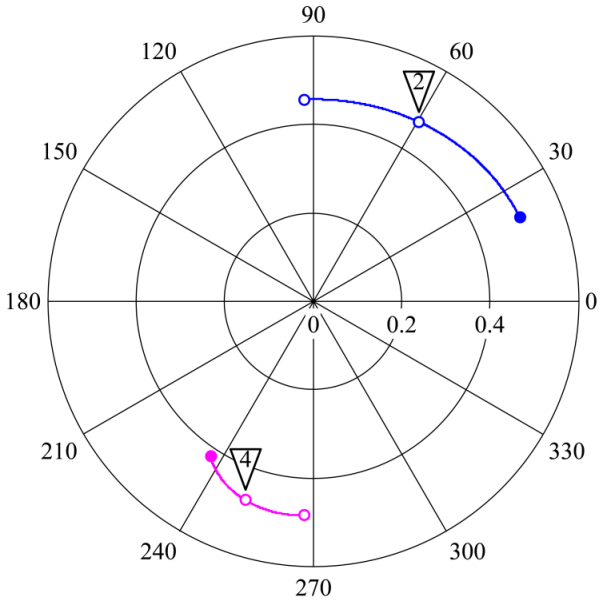

Figure 3.8. Phasing for Port 1 as driving port. Marker 1 coincides with Marker 2 and Marker 3 coincides with Marker 4.

Similarly, the phasing for Port 2 as driving port:

$\angle S_{32}$	178.4°	Marker1
$\angle S_{42}$	9.0°	Marker2
$\angle S_{52}$	12.4°	Marker3

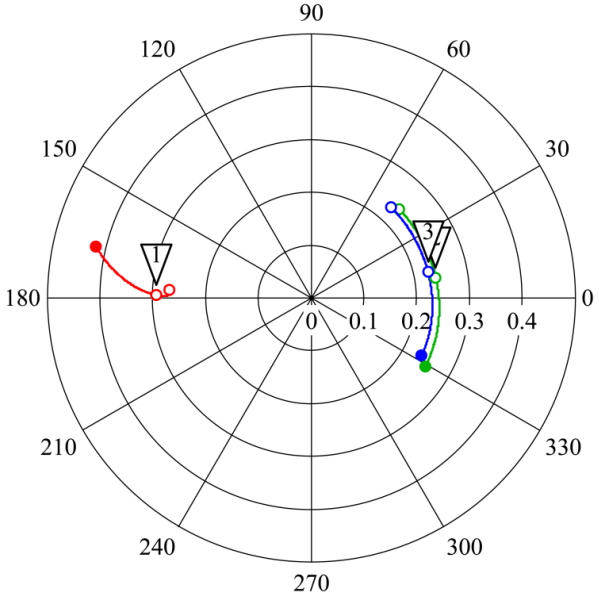

Figure 3.9. Phasing for port 2 as driving port.

Next, for Port 4 as driving port:

$\angle S_{24}$	8.7°	Marker1
$\angle S_{34}$	12.1°	Marker2
$\angle S_{54}$	159.8°	Marker3

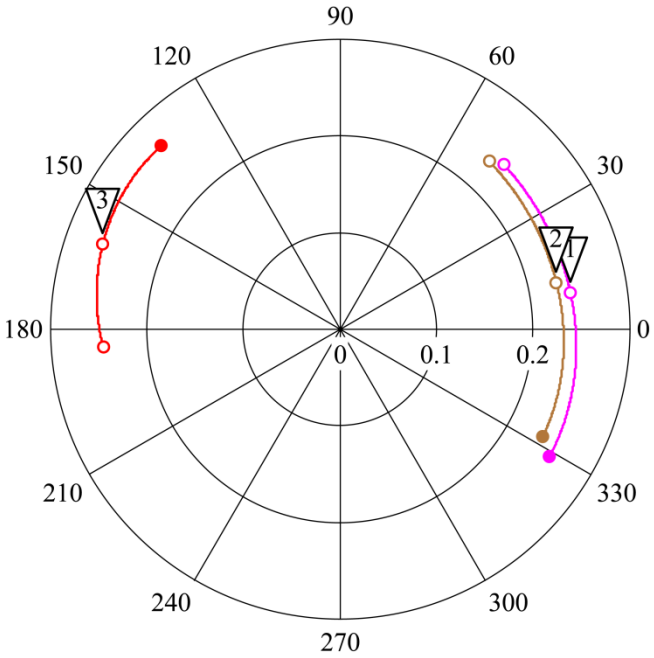

Figure 3.10. Phasing for port 4 as driving port.

The above results are obtained with the following module dimensions:

L_{dipole}	7.3 mm
W_{dipole}	1.663 mm
$L_{feed\ arm}$	2.7 mm
$W_{feed\ arm}$	0.2 mm

Lastly, the input impedance as seen by port 1 is verified. It is clear that there is some inductance present from the probe feed. This can be matched on the feed side at a later stage when the complete antenna is realized. The input match or S_{11} on the smith chart is 54.2+j7.2 Ω, and corresponds to a match of 22 dB.

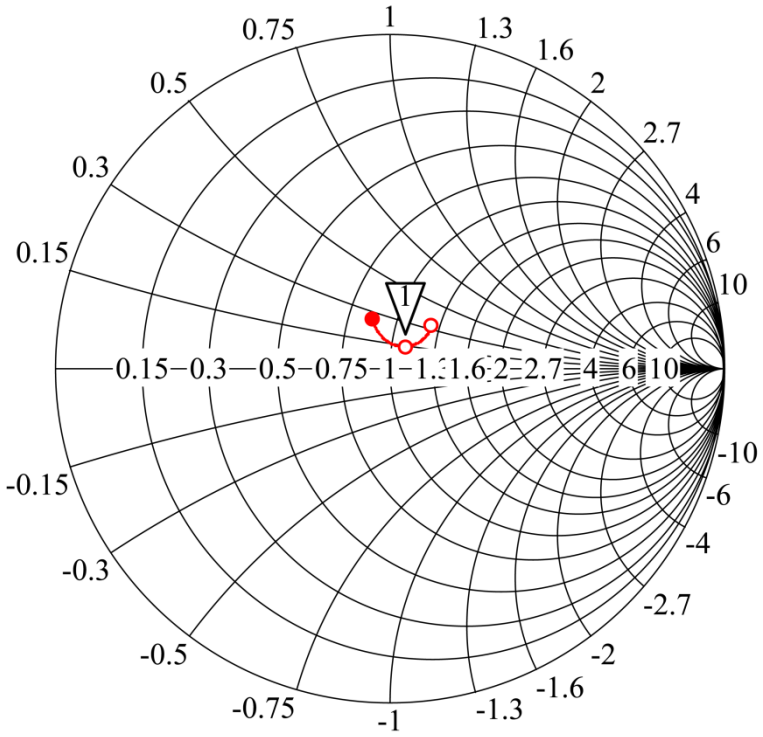

Figure 3.11. Input Impedance at port 1.

3.3.5.2 H-module Design

The same procedure is done for the optimization of the rest of the H-modules within the antenna. These modules don't have a feed port as the feeding H-module, so the rest of the H-modules can generally be optimized so that:

- $\angle S_{21}$ is equal to 180°
- $\angle S_{31}$ and $\angle S_{41}$ are equal to 0°

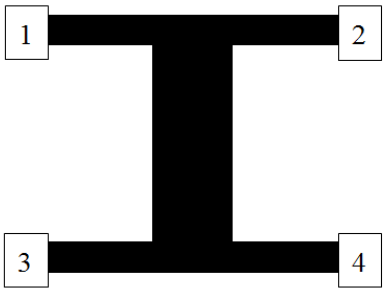

Figure 3.12. H-modules for the rest of the antenna array.

The module is symmetrical, so the above requirements will mean that for any driving port, the phasing to the other ports is also 180° or 0°. This H-module is shown in Figure 3.12. For this module, the required phasing to the ports can be optimized exactly. This is shown in Figure 3.13.

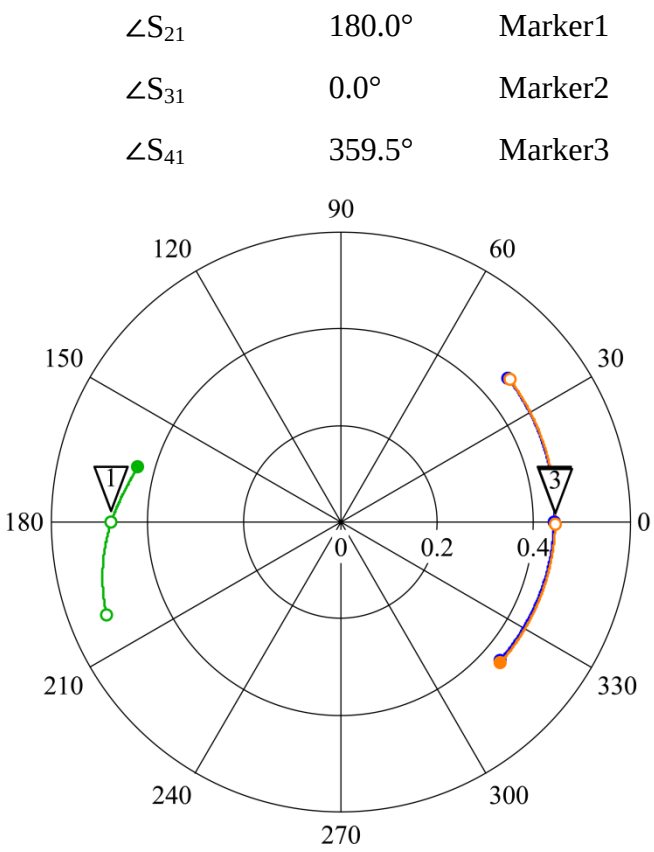

Figure 3.13. Phasing for the h-module. Marker 2 coincides with Marker 3

The key dimensions for the H-module are

L_{dipole}	7.825 mm
W_{dipole}	1.663 mm
$L_{feed\ arm}$	2.315 mm
$W_{feed\ arm}$	0.2 mm

3.3.5.3 Compromised H-module feed arm lengths

Lastly, a compromise for the feed arm lengths must be found between the H-modules and H-module (Feed). This is only really true for the horizontal spacing of the complete grid antenna. The vertical lengths of the dipoles can vary without affecting the realization of the grid antenna layout. The compromised feed arm length is therefore set at 2.5 mm. The results of the port phasing for both H-module (feed) and H-modules are then as follows:

For the H-module (feed) with port 1 as driving port:

$\angle S_{21} - \angle S_{41}$	191.9°
$\angle S_{31} - \angle S_{51}$	191.9°

For the H-module (feed) with port 2 as driving port:

$\angle S_{32}$	189.5°
$\angle S_{42}$	19.3°
$\angle S_{52}$	22.4°

For the H-module (feed) with port 4 as driving port:

$\angle S_{24}$	19.0°
$\angle S_{34}$	22.1°
$\angle S_{54}$	170.2°

For the H-modules:

$\angle S_{21}$	169.4°
$\angle S_{31}$	349.4°
$\angle S_{41}$	348.8°

3.3.5.4 T-modules design

The T-module is shown in Figure 3.14 below. The feed arm length is found to be 2.643 mm, while the dipole length is found to be 5.875 mm. The result is the phase of S_{21} is equal to 179.9°.

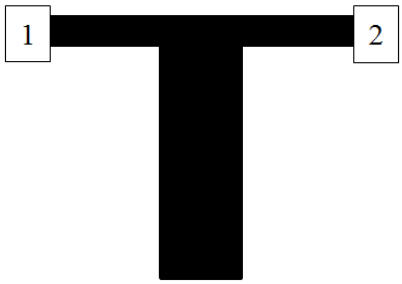

Figure 3.14. The T-Module.

The dipole length is first found by examining $|S_{11}|$ and adjusting the dipole length until resonance is achieved at the operating frequency. Thereafter, the feed arm lengths are adjusted until the correct port phasing is achieved. This method gets rid of ambiguity when trying to optimize the single phase relationship between port 1 and port 2, while having two variables (feed arm length and dipole length) to tune.

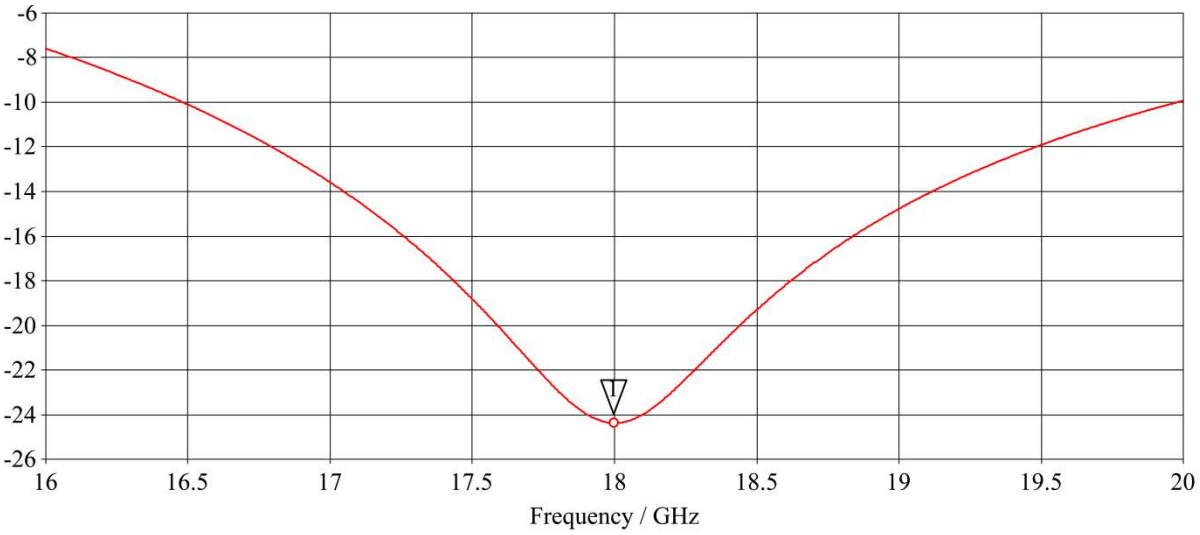

Figure 3.15. T-module dipole resonance ($|S_{11}|$=-24.3 dB at 18 GHz).

The resultant port phasing for the T-module is shown in Figure 3.16 below.

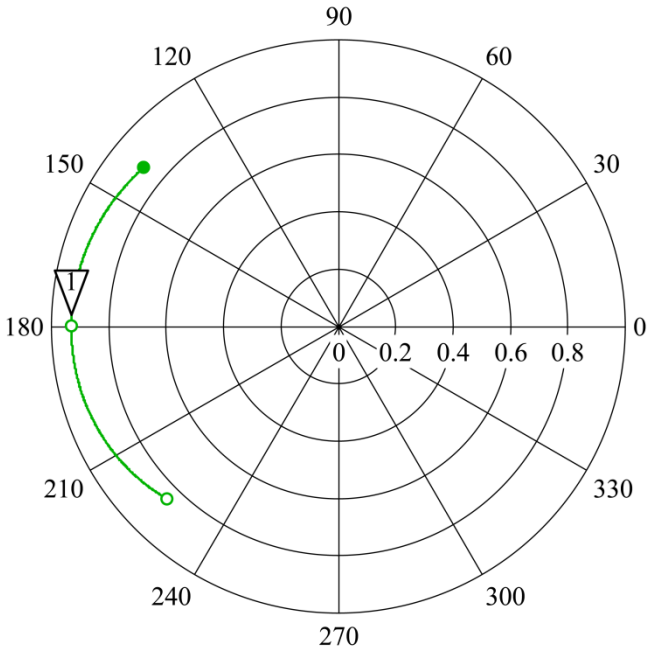

Figure 3.16. Phasing for the T-module (S_{21}=0.93 ∠179.9° at 18 GHz).

3.3.5.5 U-Modules design

The U-module is optimized in the same way as was done for the T-module. First the dipole length is found be examining the resonance frequency, and then the feed arm lengths are adjusted to achieve the required port phasing. The required port phasing for the U-module is 0°.

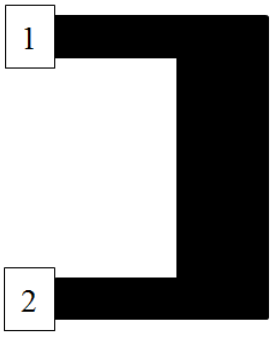

Figure 3.17. The U-module.

After optimization, the U-module dipole length is 5.5 mm long, and the feed arm lengths are 3.08 mm long. The resultant S-parameters are shown below, with the phasing (359.6°) shown in Figure 3.18 and the dipole resonance shown in Figure 3.19.

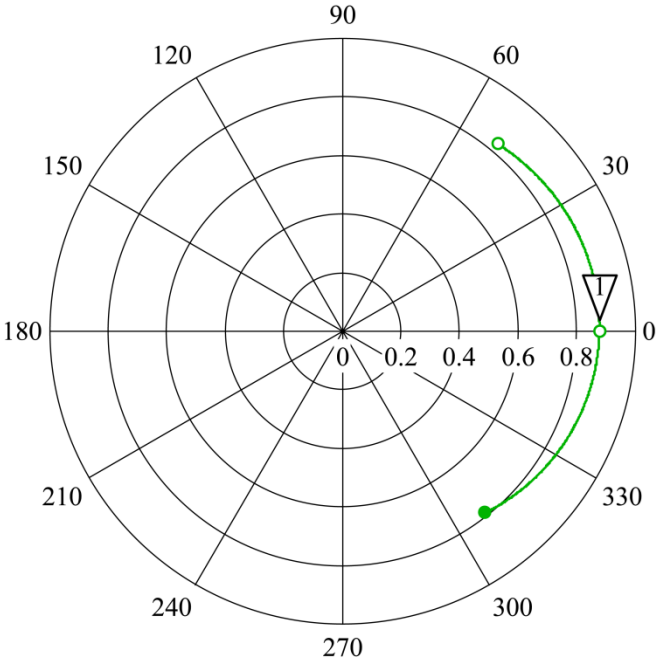

Figure 3.18. Phasing for the U-module (S_{21}=0.88 ∠359.6° at 18 GHz).

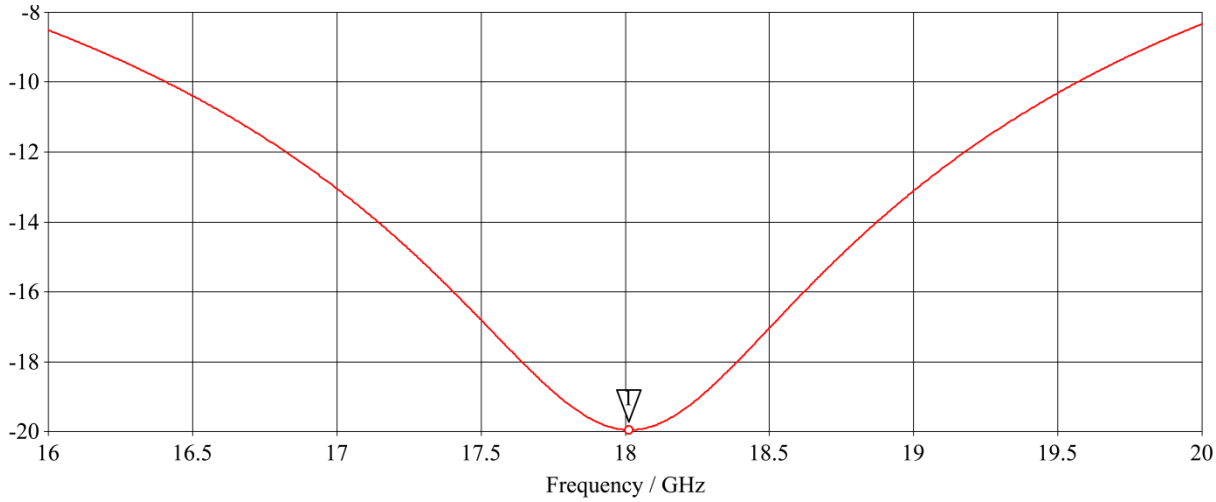

Figure 3.19. U-module dipole resonance ($|S_{11}|$=-19.9 dB at 18 GHz).

3.3.5.6 I-modules design

The last module to be designed is the I-module. This module looks exactly like the free resonance dipole simulation done to determine the initial dipole length and width. Therefore, it is not necessary to further optimize on the dipole length for this module. Only the feed arm length needs to be adjusted, so that the phase of S_{11} is equal to 180°. After optimization, the feed arm length is 3.15mm, and the phase of S_{11} for the I-module is 180°.

3.3.5.7 Summary of module dimensions

The table below shows a summary of the module dimensions required to yield the best overall phasing between the ports of each module

Table 3.1. Summary of the module dimensions.

	Dipole Length [mm]	Dipole Width [mm]	Feed Arm Length [mm]	Feed Arm Width [mm]
H-module(feed)	7.3	1.663	2.7	0.2
H-module	7.825	1.663	2.315	0.2
T-module	5.875	1.663	2.643	0.2
U-module	5.5	1.663	3.08	0.2
I-module	5.335	1.663	3.15	0.2

3.3.6 Construction of the Microstrip Wire Grid Antenna

The microstrip wire grid array is constructed in CST for simulation. The way in which this is done is to first place the dipoles at certain calculated coordinates, and then connect them with the horizontal feed lines. Referring to Figure 3.5 for the dipole numbering, and Figure 3.20 for the coordinates, dipole 1 is placed such that its centre is at coordinate (0,0). Dipole 2 is places at the same vertical coordinate as dipole 1, but at a specific offset in the horizontal dimension. This coordinate is defined as $D_{x1} + 1.5D_x$. Here, D_{x1} is horizontal distance from the centre of dipole 1 to the edge of its horizontal feed line as used in the individual module optimization step. D_x is the average horizontal dimension of the H-

modules as was found in 3.3.5.3. It is made up of twice the compromise feed arm length plus the H-module dipole width as per the individual module optimization step. The horizontal offset between dipole 2 and dipole 3 is $2D_x$ and the last dipole in the bottom row, dipole 4 is offset from dipole 3 by $D_{x4} + 1.5D_x$. The vertical spacing D_y is determined by the average height of the H-modules, dipole 5 is therefore located at coordinate ($D_{x1} - D_{x8}$, D_y). The rest of the coordinates of the dipoles is given in Table 3.2.

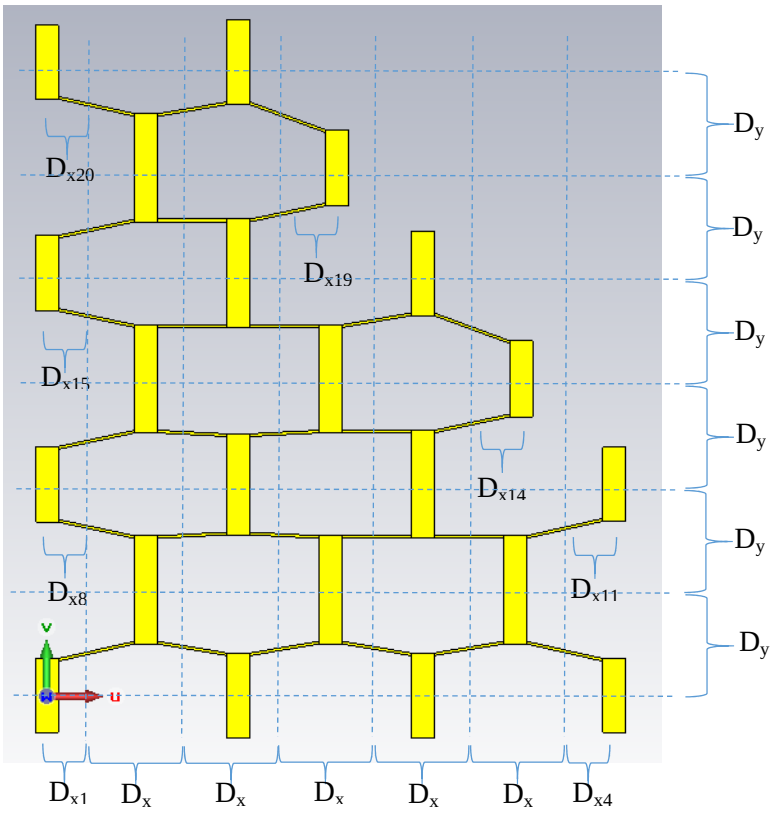

Figure 3.20. Wire grid array with the dipole spacing concept shown.

At first, all of the horizontal spacings D_{x1}, D_{x4}, D_{x8}, D_{x11}, D_{x14}, D_{x15}, D_{x19} and D_{x20} are set equal to $0.5D_x$ which is 2.5 mm. D_y is equal to the average H-module length (including the feed module), or 7.767 mm.

Table 3.2. Coordinates of the dipoles.

Dipole Number	x-coordinate	y-coordinate
1	0	0
2	$D_{x1}+1.5D_x$	0
3	$D_{x1}+3.5D_x$	0
4	$D_{x1}+5D_x+D_{x4}$	0
5	$D_{x1}+0.5D_x$	D_y
6	$D_{x1}+2.5D_x$	D_y
7	$D_{x1}+4.5D_x$	D_y
8	$D_{x1}- D_{x8}$	$2D_y$
9	$D_{x1}- D_{x8}+1.5D_x$	$2D_y$
10	$D_{x1}- D_{x8}+3.5D_x$	$2D_y$
11	$D_{x1}- D_{x8}+5D_x+D_{x11}$	$2D_y$
12	$D_{x1}+0.5D_x$	$3D_y$
13	$D_{x1}+2.5D_x$	$3D_y$
14	$D_{x1}+4D_x+D_{x14}$	$3D_y$
15	$D_{x1}- D_{x15}$	$4D_y$
16	$D_{x1}- D_{x15}+1.5D_x$	$4D_y$
17	$D_{x1}- D_{x15}+3.5D_x$	$4D_y$
18	$D_{x1}+0.5D_x$	$5D_y$
19	$D_{x1}+2D_x+ D_{x19}$	$5D_y$
20	$D_{x1}- D_{x20}$	$6D_y$
21	$D_{x1}- D_{x20}+1.5D_x$	$6D_y$

Due to the different dipole lengths, the feed arm lengths are longer than those obtained during the individual dipole optimization. Therefore T-, U-, and I-modules need to be re-evaluated. Referring to Figure 3.21 the first modules to be re-evaluated are the T-modules. Measuring the feed length section between module 5 and module 2 yields a distance of 5.123 mm. This section is circled in green on Figure 3.21. During the individual module optimization, the H-modules had a compromised feed length of 2.5 mm while the T-modules had a feed length of 2.643 mm. This equals 5.143 mm. Since the measured distance is 5.123 mm and 2.5 mm of this distance is allocated to the feed arm of module 5, the feed arm of module 2 is only 2.623 mm long. This is a small enough difference, however, for this exercise we return to the individual module optimization for module 2. This new feed arm length is used, and the length of the dipole of module 2 is adjusted until the phase relationship is once again 180°. The re-optimization for module 3, 17 and 21 is done similarly by measuring the feed arm lengths on Figure 3.21 which is circled in green. For the equally excited antenna, all the T-module dipole lengths are therefore adjusted to 5.909 mm.

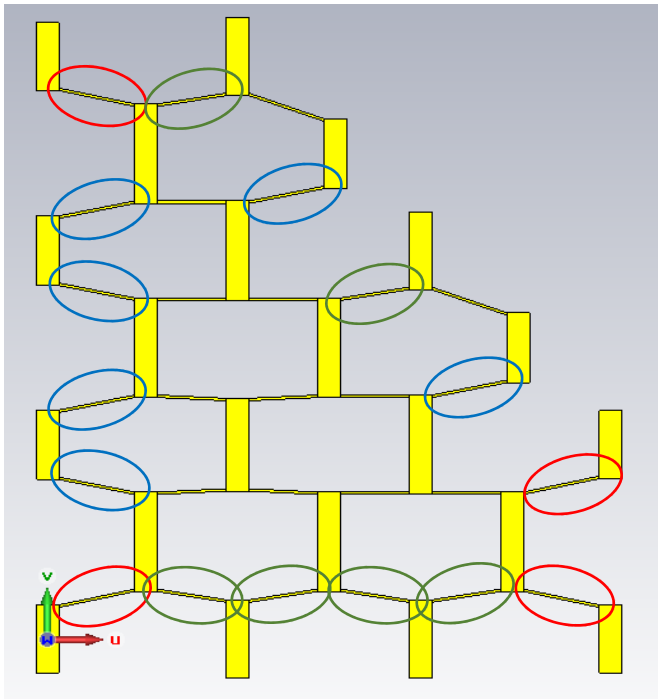

Figure 3.21. A single quadrant of the microstrip wire grid array.

Next, the U-modules are re-examined, by measuring the feed line distance on the wire grid antenna, and comparing that to what was found during the individual module optimization step. In this case however, the U-modules can simply be moved to correct the feed lengths, for instance, the feed line length between the dipoles of module 8 and 5 measures 5.167 mm. The feed line length between the dipoles of module 8 and 12 also measures 5.167 mm. This total length is 10.334 mm. Once again, the allocation of this length towards the H-modules is 5 mm, so the total feed length allocated to the U-module is 5.334 mm. During the individual module optimization step, the feed length of the U-module should be 6.16 mm (2 x 3.08 mm). Therefore, D_{x8} is adjusted until the total feed length between modules 5, 8 and 12 measures 6.16 mm + 5 mm, or 11.16 mm. D_{x8} therefore changes to 3.757 mm. The same reasoning leads to D_{x15} equals to 3.757 mm, while D_{x14} and D_{x19} equals to 3.666 mm.

The last modules to be re-examined are the I-modules. The I-module feed line was found to be 3.15 mm during the individual module optimization step. The expected feed line length is therefore 5.65 mm on the wire grid antenna. Therefore, D_{x1}, D_{x4}, D_{x11} and D_{x20} are adjusted to 3.81 mm. The final quadrant is shown below, inclusive of the probe feed.

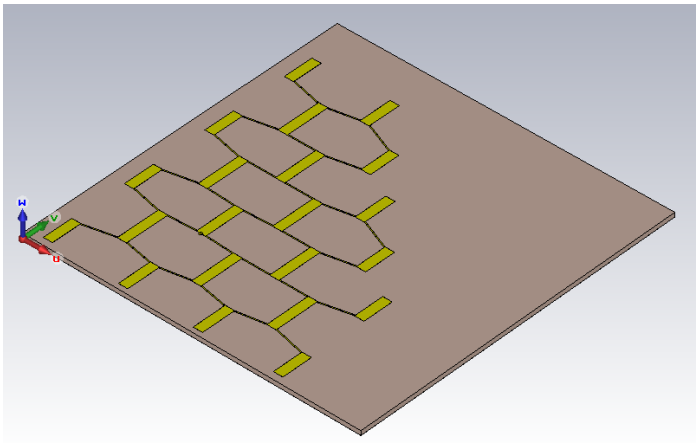

Figure 3.22. The completed quadrant of the monopulse wire grid antenna.

Finally, the entire microstrip wire grid antenna is moved, so that the horizontal spacing between the quadrants is $0.325\lambda_0$ and the vertical spacing between the quadrants is $0.1\lambda_0$.

The parameters describing the antenna are given below in Table 3.3.

Table 3.3. Parameters for the wire grid antenna with equal excitation. D_{xx} are horizontal spacings, D_y is the vertical spacing, L_{ii} and W represents dipole lengths and widths respectively

Parameter	Dimension [mm]
D_x	6.663
D_{x1}	3.810
D_{x4}	3.810
D_{x8}	3.757
D_{x11}	3.810
D_{x14}	3.666
D_{x15}	3.757
D_{x19}	3.666
D_{x20}	3.810
D_y	7.767
$W_{Dipoles}$	1.663
L_1,L_4,L_{11},L_{20}	5.335
L_8,L_{14},L_{15},L_{19}	5.5
L_2,L_3,L_{17},L_{21}	5.909
L_5,L_6,L_7,L_{10},L_{12},L_{13},L_{16},L_{18}	7.825
L_9	7.3
Feed Position *x*	17.3
Feed Position *y*	19.1

The resultant antenna geometry is somewhat larger than the original aperture, so the antenna gain is expected to be more than 23 dBi. This is shown in Figure 3.23.

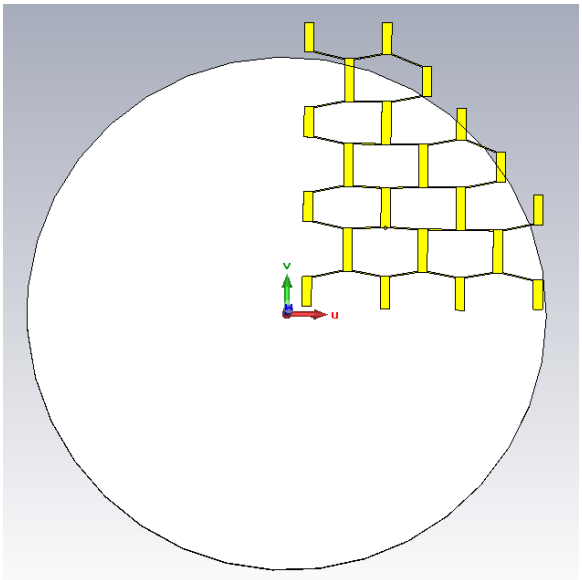

Figure 3.23. Antenna layout printed onto a circular area of radius 46mm.

The input match is shown in Figure 3.24. As can be seen, the antenna is resonant at 17.5 GHz, or 3% lower than the design frequency. Therefore, before the taper can be designed, the equal aperture antenna needs to be scaled to 18 GHz, so that the element positions are known a priori as accurately as possible. The scaling is done by adjusting the D_x and D_y parameters.

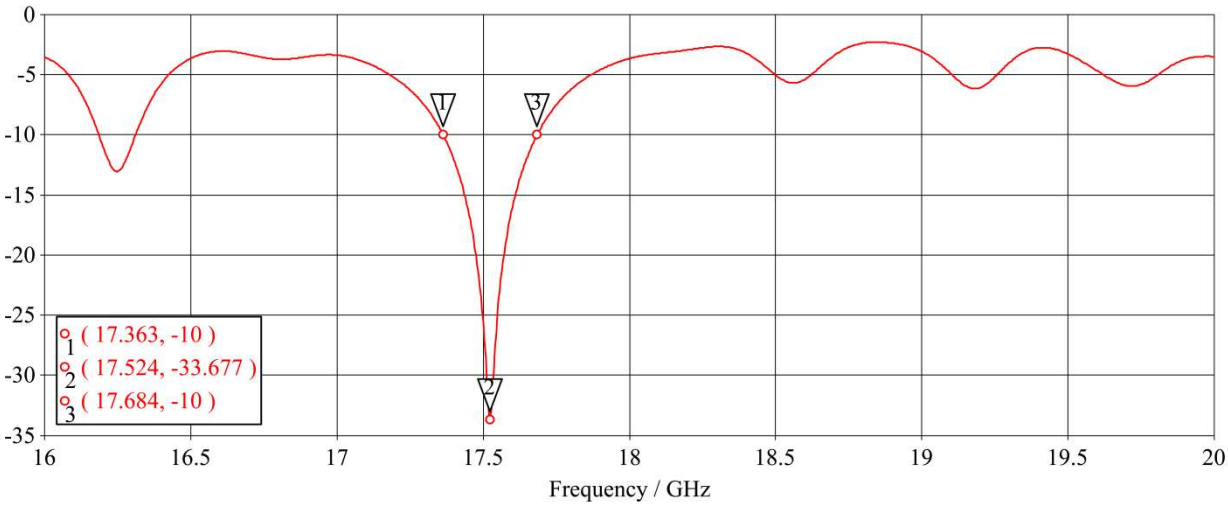

Figure 3.24. The input match of the single quadrant antenna ($|S_{11}|$ dB).

Table 3.4 shows the new parameters of the scaled equal excitation antenna. The scaled antenna is simulated again to check that resonance is now at the required 18 GHz. The result is shown in Figure 3.25. The Y-component current distribution is shown in Figure 3.26. As can be seen, all the dipoles are relatively "in-phase" meaning that the module design approach is valid.

Table 3.4. Dipole spacing parameters for the scaled wire grid antenna with equal excitation.

Parameter	Dimension [mm]
D_x	6.490
D_{x1}	3.709
D_{x4}	3.709
D_{x8}	3.658
D_{x11}	3.709
D_{x14}	3.569
D_{x15}	3.658
D_{x19}	3.569
D_{x20}	3.709
D_y	7.562
$W_{Dipoles}$	1.663
L_1,L_4,L_{11},L_{20}	5.194
L_8,L_{14},L_{15},L_{19}	5.355
L_2,L_3,L_{17},L_{21}	5.753
L_5,L_6,L_7,L_{10},L_{12},L_{13},L_{16},L_{18}	7.618
L_9	7.107
Feed Position *x*	17.3
Feed Position *y*	19.1

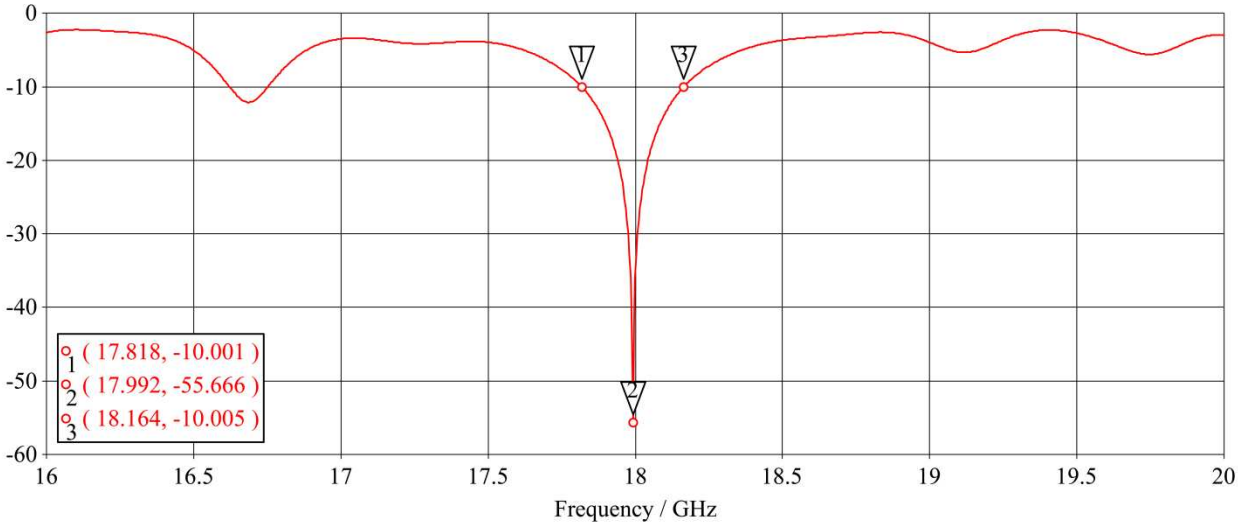

Figure 3.25. The input match of the scaled equally excited wire grid antenna ($|S_{11}|$ dB).

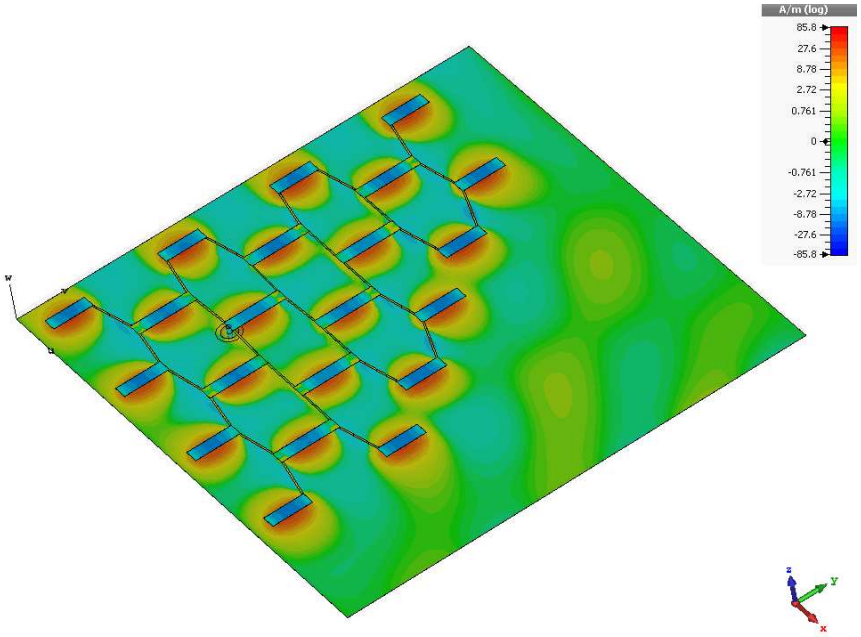

Figure 3.26. Dipole Y-component currents.

Next, the complete 4 quadrant monopulse wire grid antenna is simulated, to get an idea of the gain and what the side lobe levels are for the uniformly illuminated antenna. The geometry of the antenna is shown in Figure 3.27. The principal plane polar pattern reveals that for the sum channel, the side lobe levels are roughly 18 dB down. This is mainly due to the antenna geometry, as the weights are all equal.

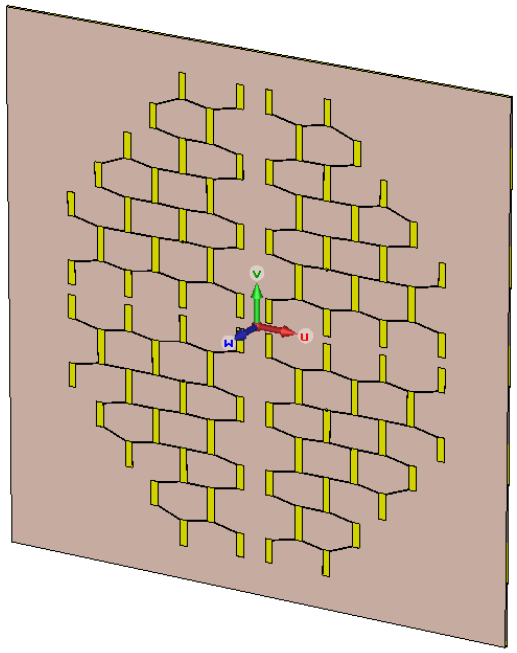

Figure 3.27. 4 Quadrant uniformly illuminated monopulse wire grid antenna.

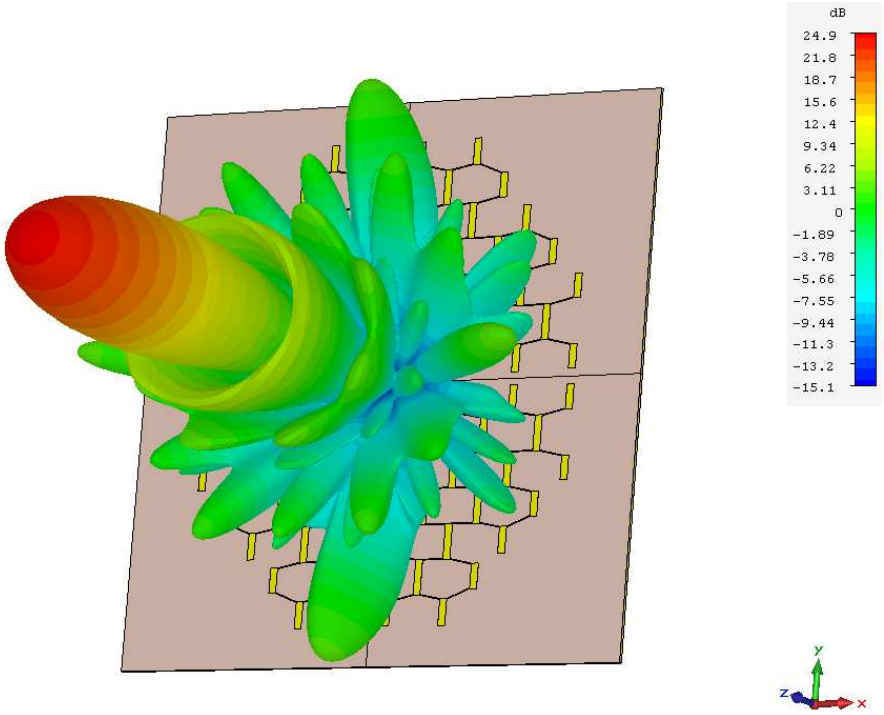

Figure 3.28. Sum 3D Far field pattern of the monopulse wire grid antenna.

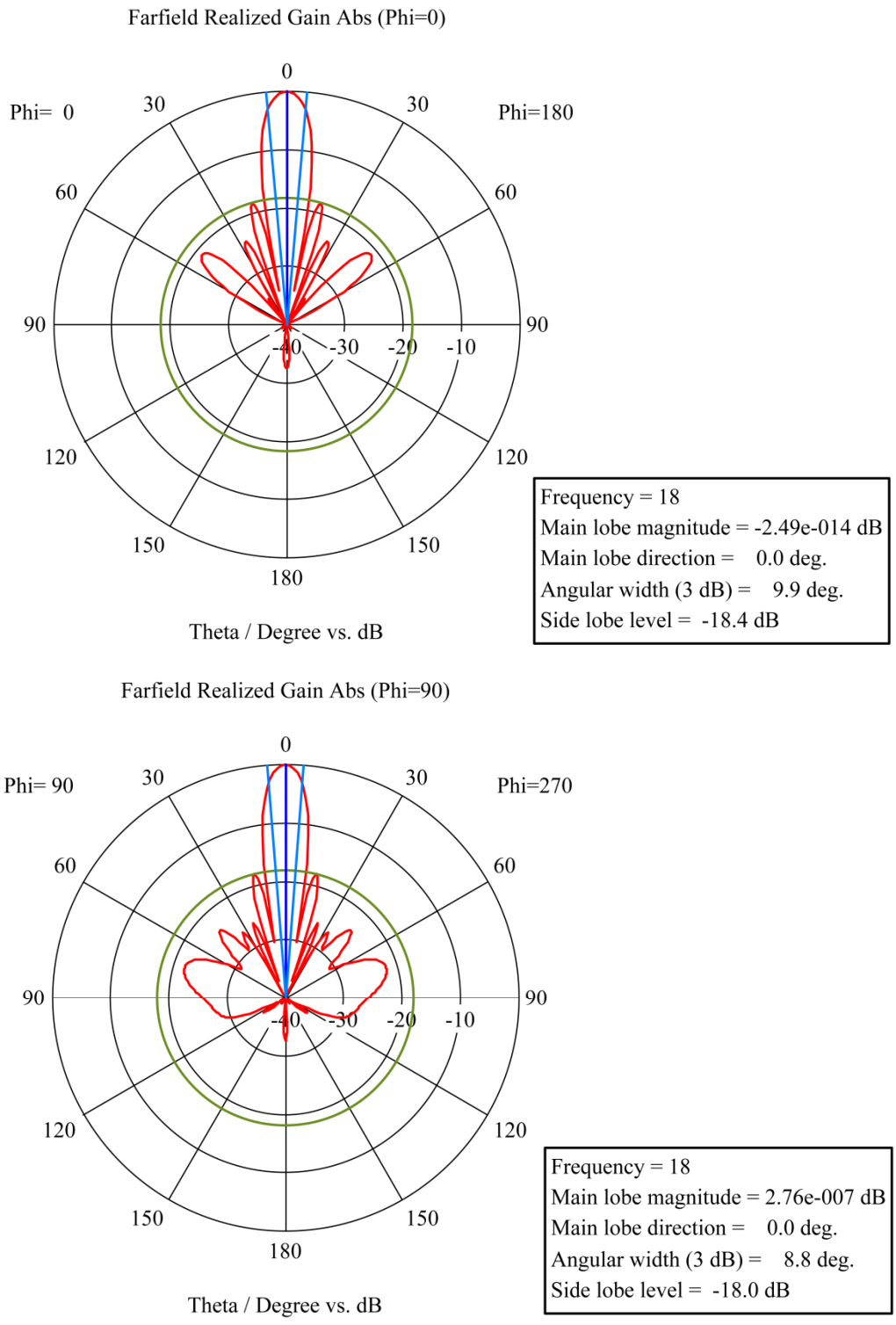

Figure 3.29. Principal planes of the sum far field pattern.

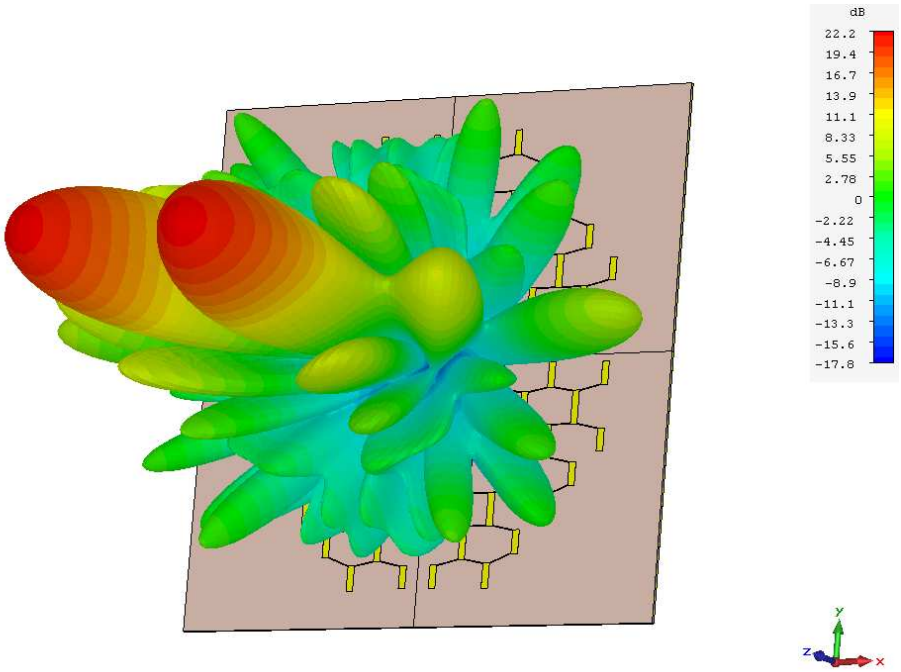

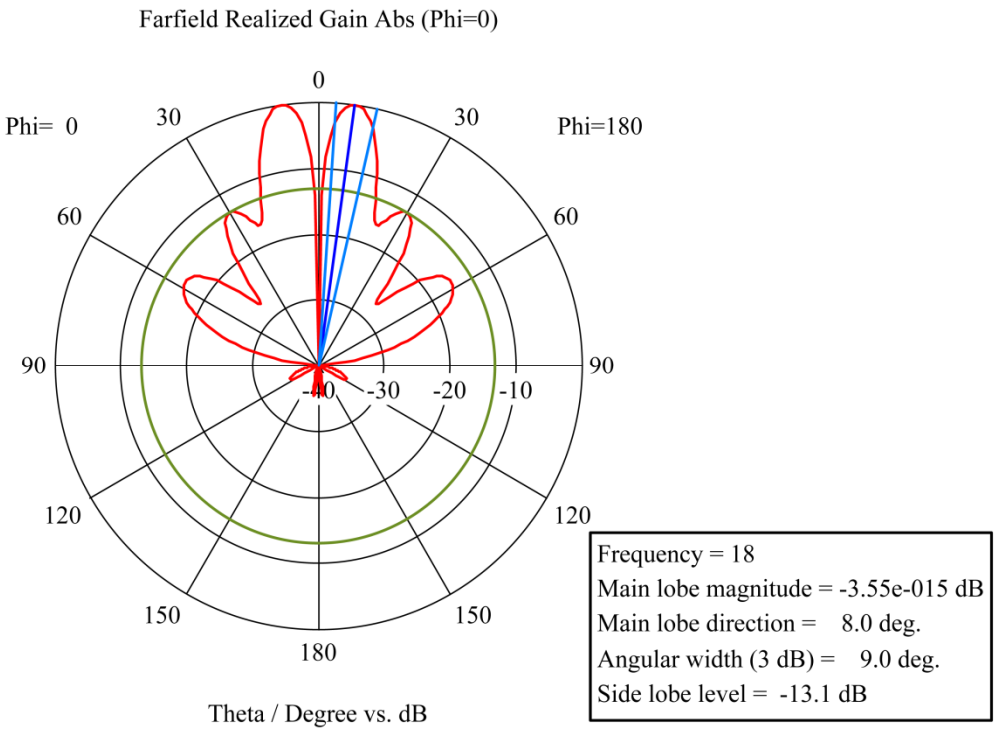

Figure 3.30. Azimuth Difference pattern, 3D (Top) and polar (Bottom).

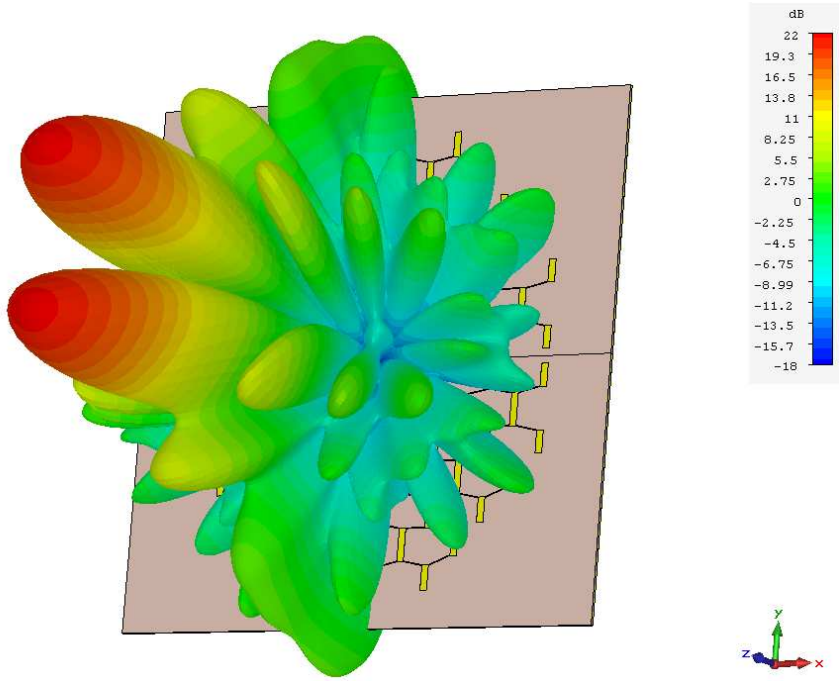

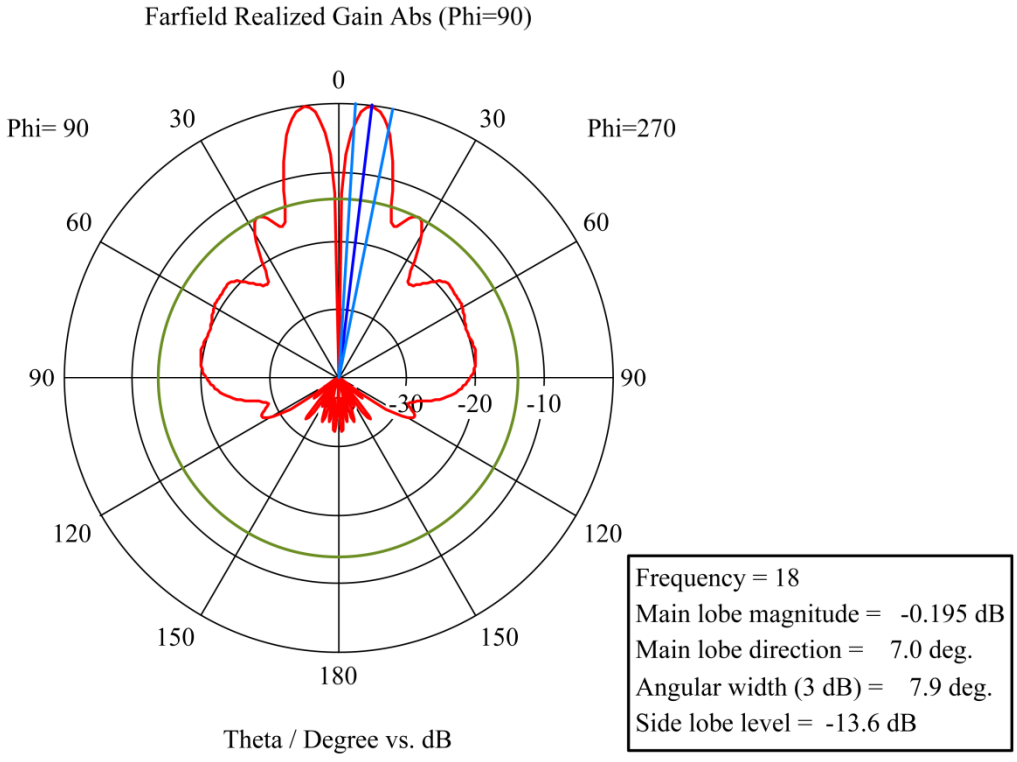

Figure 3.31. Elevation Difference pattern, 3D (Top) and polar (Bottom).

The measured gain for the sum mode is 24.9 dBi as shown in Figure 3.28. The layout of Figure 3.27 can be completely encapsulated within a circular area of 112 mm diameter, or $9.852e^{-3}$ m^2. The expected gain for an aperture of this size is 26.5 dBi. This indicates that the illumination efficiency is 70% for this aperture size.

3.4 COMPARISON BETWEEN 3D FULL WAVE SOLUTION AND ARRAY FACTOR

The equations of section 3.2 are used to calculate the radiation patterns of the array geometry as shown in Figure 3.32 and specified in Table 3.4. The element pattern is assumed to be cosine squared, and the excitation level to each element is set to unity. The calculated array patterns are compared to a full wave Electromagnetic (EM) simulation, and the results in the principal planes are shown in Figure 3.33. Detailed 3D pattern results are given in Figure 3.34 and Figure 3.35 where comparisons are made at a couple of key coordinates. These key coordinates are listed in Table 3.5. From Table 3.5 it can be seen that generally, the patterns are similar, but there are places, notably where the calculated directivity predicts side lobe levels lower than around 22 dB where there are significant differences. This would mainly be due to current phase distribution of the vertical dipoles, spurious radiation from the feed point, and mutual coupling between dipoles.

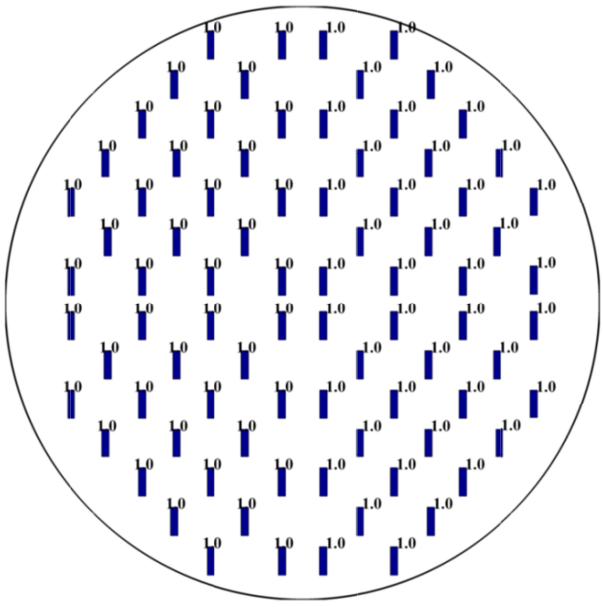

Figure 3.32. Geometry for directivity calculation of the equally excited monopulse antenna array.

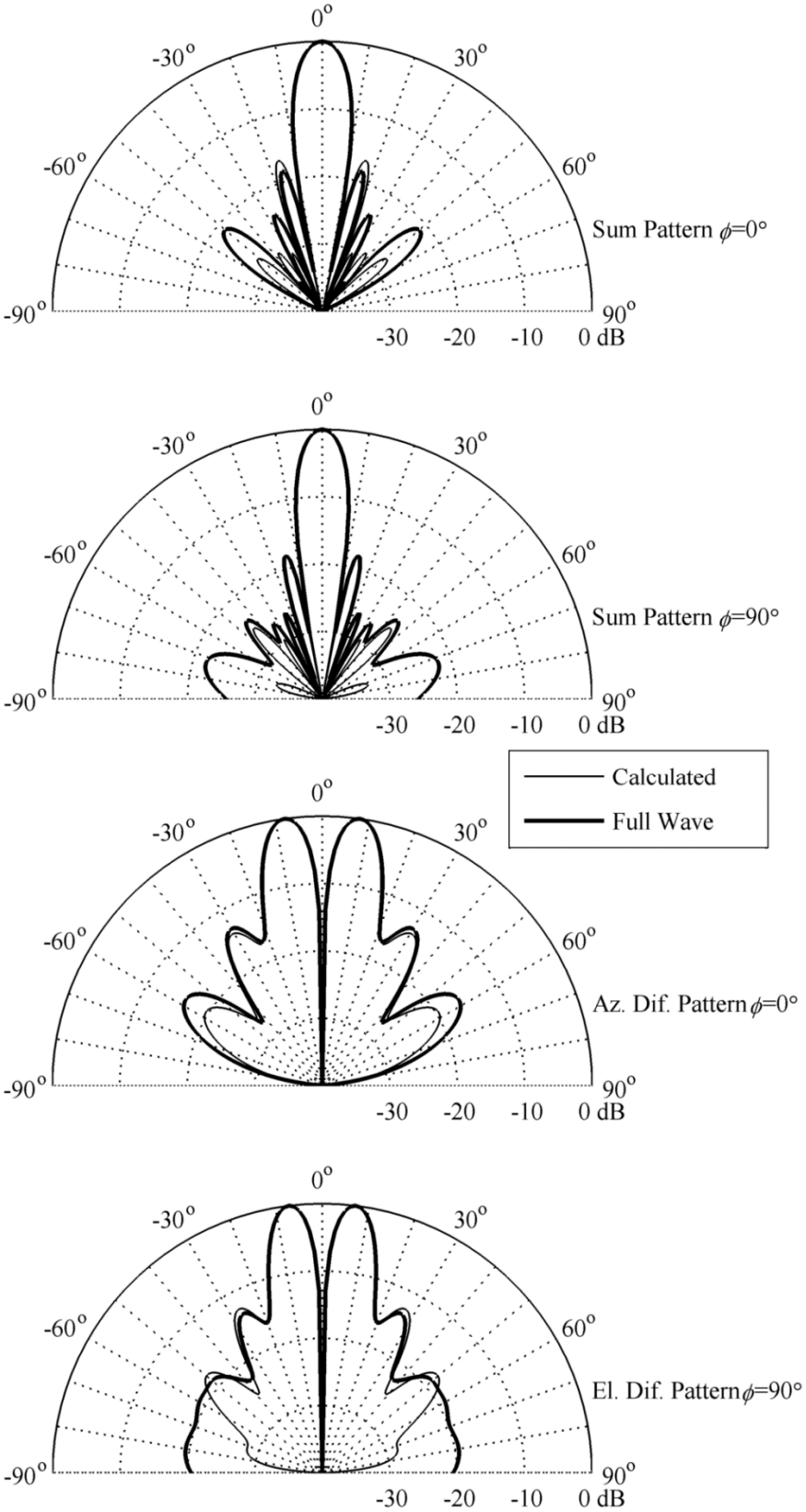

Figure 3.33. Principal plane calculated and full wave radiation patterns.

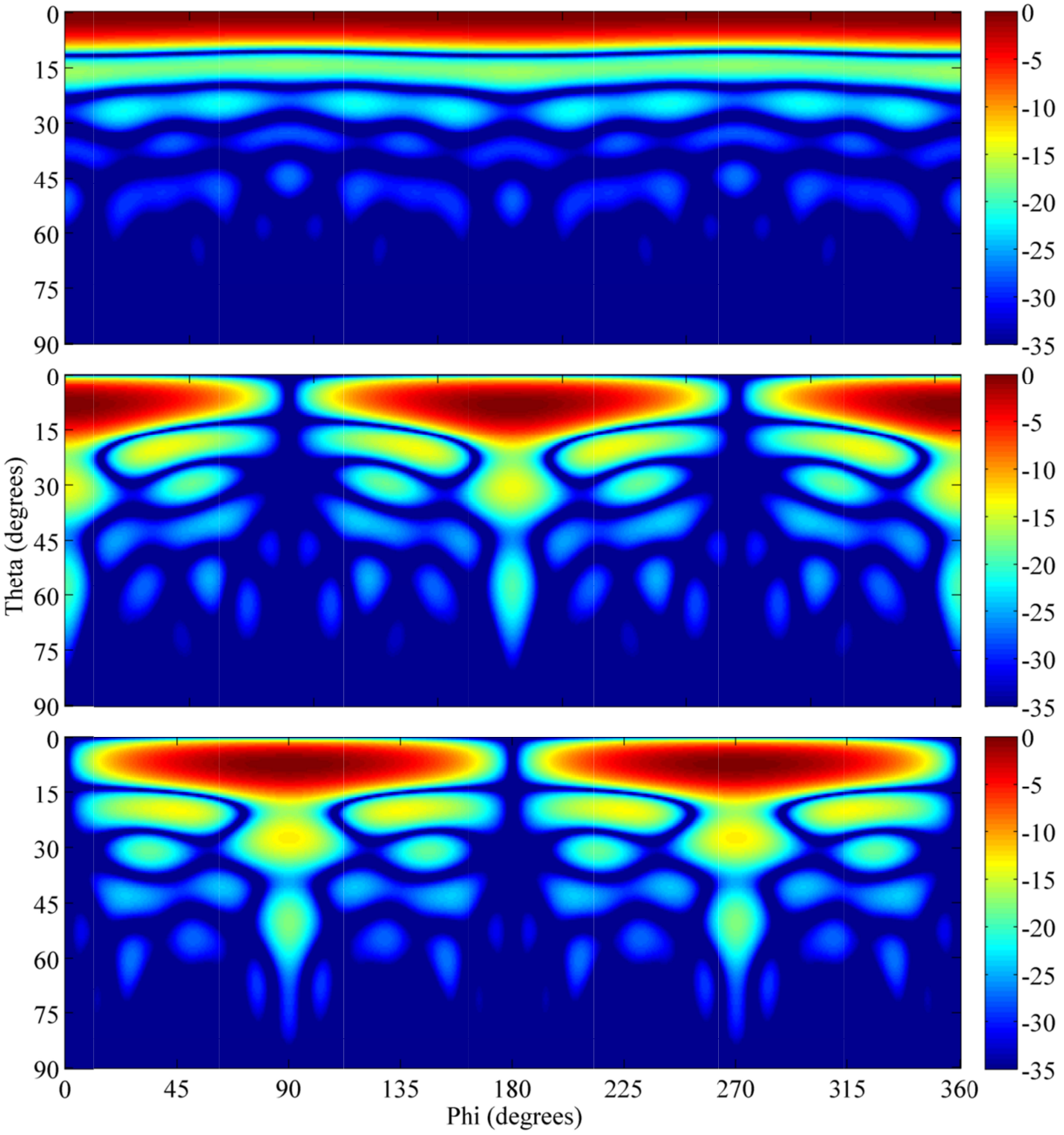

Figure 3.34. Resulting normalised radiation pattern calculated by a MATLAB script for the geometry and excitation of the monopulse antenna array of Figure 3.32. From top to bottom is sum, azimuth difference and elevation difference patterns. The colour bar is in dB.

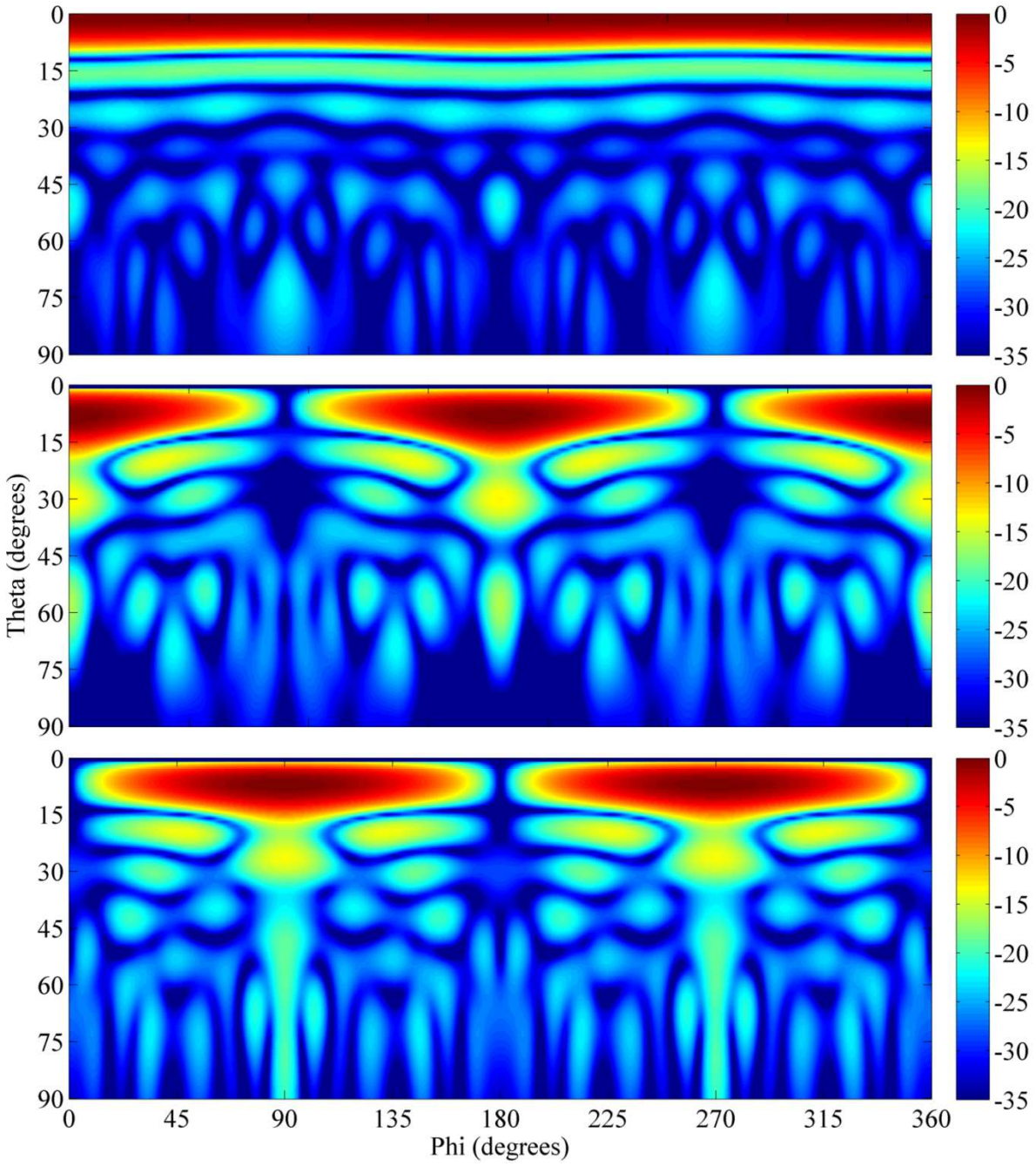

Figure 3.35. Full wave calculated normalised radiation pattern for the geometry and excitation of the monopulse antenna array of Figure 3.32. From top to bottom is sum, azimuth difference and elevation difference patterns. The colour bar is in dB.

At coordinate number 8, the calculated directivity level is -19.6 dB, while the full wave simulation results in a level of -16.1 dB. This level is high enough to indicate that effects such as mutual coupling and current phase distribution are causing degradation in the radiation pattern. It is therefore important to note that spurious feed radiation and mutual coupling might limit the ability to control side lobes lower than 22 dB on this electrically thick substrate. In terms of wavelengths, the substrate thickness is 0.07λ in the dielectric.

Table 3.5. Comparison between the full wave and calculated radiation patterns.

Nr.	Coordinate (ϕ, θ)°	Radiation pattern type	Full Wave Directivity (dB)	Calculated directivity (dB)
1	(45, 15)	Sum Pattern	-17.8	-17.9
2	(62, 24)	Sum Pattern	-21.6	-21.9
3	(0, 51)	Sum Pattern	-21.2	-27.7
4	(90, 44)	Sum Pattern	-23.9	-25.4
5	(90, 73)	Sum. Pattern	-22.0	-32.9
6	(118, 48)	Sum Pattern	-23.2	-27.8
7	(180, 30)	AZ. Dif. Pattern	-13.1	-13.9
8	(180, 58)	AZ. Dif. Pattern	-16.1	-19.6
9	(143, 20)	AZ. Dif. Pattern	-13.6	-13.7
10	(210, 60)	AZ. Dif. Pattern	-21.0	-28.0
11	(90, 26)	EL. Dif. Pattern	-13.6	-12.8
12	(90, 50)	EL. Dif. Pattern	-18.7	-17.6
13	(48, 20)	EL. Dif. Pattern	-13.7	-13.5
14	(35, 30)	EL. Dif. Pattern	-18.4	-18.9

3.5 MONOPULSE PATTERN SYNTHESIS USING THE SEQUENTIAL QUADRATIC PROGRAMME

The concept of McNamara [7] needs to be expanded to optimize for planar arrays in sum pattern, elevation difference pattern and azimuth difference pattern. The quadratic quantity to be minimized can be written as

$$Q[J] = \alpha Q_{SUM}[J] + \beta Q_{AZIMUTH\ DIFF}[J] + \gamma Q_{ELEVATION\ DIFF}[J] \tag{3.31}$$

The B matrix and F_0 in (2.12) can be written as

$$\begin{aligned} B &= \alpha B_{SUM} + \beta B_{AZIMUTH\ DIFF} + \gamma B_{ELEVATION\ DIFF} \\ F_0 &= \alpha F_{0SUM} + \beta F_{0AZIMUTH\ DIFF} + \gamma F_{0ELEVATION\ DIFF} \end{aligned} \tag{3.32}$$

And the constraints is written as

$$\begin{aligned} J^T(\pm F_{SUM} - cF_{0\ SUM}) &\leq 0 \\ J^T(\pm F_{AZIMUTH\ DIFF} - cF_{0\ AZIMUTH\ DIFF}) &\leq 0 \\ J^T(\pm F_{ELEVATION\ DIFF} - cF_{0\ ELEVATION\ DIFF}) &\leq 0 \end{aligned} \tag{3.33}$$

Here, α, β and γ are weights that are assigned to each quadratic quantity in forming the combined quadratic quantity for optimization. Following McNamara's [7] work, these weights are simply kept equal, while the constraints are individually applied to the sum and two difference patterns.

3.5.1 The sequential quadratic programme implemented in MATLAB

MATLAB code was developed to implement the sequential quadratic programme synthesis technique for simultaneous sum and difference pattern side lobe optimization. Before any optimization can be attempted, a rough idea of the antenna geometry is needed. The

antenna geometry of Figure 3.2 was used as the starting point. First the constraints need to be defined.

3.5.1.1 The sum constraints

The constraints are implemented in MATLAB. First, a mesh grid of the (ϕ,θ) coordinates at which the array factor will be evaluated is created

```
Phi0=0:1:90;
Theta0=0:0.5:90;

[Phi,Theta]=meshgrid(Phi0,Theta0)
C=zeros(size(Phi));
C(Theta>=15)=-17;
C(Theta>=23)=-20;
```

The code above shows that the constraints will only be evaluated over a single quadrant of ϕ and in the top hemisphere only. This is because the antenna is symmetrical, and enforcing the side lobe levels in this quadrant only will automatically have the same effect in all other quadrants. The lower half of the hemisphere is ignored, as the element pattern is essentially zero in this direction. For isotropic radiators, the bottom hemisphere will look exactly the same as the top hemisphere. C in the above code is the required maximum side lobe level at each (ϕ, θ). Initially it is set at 0 dB. Then, the sum pattern side lobe level constraints are set to be maximum -17 dB for all $\theta \geq 15°$ and -20 dB for all $\theta \geq 23°$.

It should be noted that these constraints were not found arbitrarily, but rather in an iterative process, where the constraints were lowered, and the angles at which these constraints apply were tightened until a solution could not be found.

Next, F_s is evaluated at each (ϕ, θ) within the constraints list

```
for phi=1:size(Phi,2);
  for theta=1:size(Theta,1);
    for n=1:N
      u=sin(Theta(theta,phi)*pi/180)*cos(Phi(theta,phi)*pi/180);
      v=sin(Theta(theta,phi)*pi/180)*sin(Phi(theta,phi)*pi/180);
      Fs(n,index)   =     cos(k*xn(n)*u)*...
                          cos(k*yn(n)*v)*...
                          cos(Theta(theta,phi)*pi/180);
     end;
    index=index+1;
  end;
end;
```

In the above code *N* is the amount of elements in a single quadrant of the antenna. The locations of each element on the antenna are given in the vectors *xn* and *yn*. The last cosine term in the calculation for F_s is associated with the element pattern, which is assumed to be cosine squared. F_s is therefore a matrix of *N* rows, and *index* columns. The amount of columns basically represents the amount of constraints in the (ϕ, θ) plane. Next, F_s is calculated at the antenna scan angle. This value is denoted as F_0. Once F_0 is calculated, the maximum value of the side lobe levels is calculated using F_0 and the *C* matrix.

```
for n=1:N
    u=sin(Max_Directivity_Theta*pi/180)*cos(Max_Directivity_Phi);
    v=sin(Max_Directivity_Theta*pi/180)*sin(Max_Directivity_Phi);
    F0(n,1)=    cos(k*xn(n)*u)*...
                cos(k*yn(n)*v)*...
                cos(Max_Directivity_Theta*pi/180);
end;


index=1;

for phi=1:size(Phi,2)
    for theta=1:size(Theta,1)

        cF0(:,index)=10^(C(theta,phi)/20).*F0;
        index=index+1;
    end;
end;

a1  =   (Fs-cF0)';
a2  =   (-Fs-cF0)';
a=cat(1,a1,a2);
b=zeros(size(a,1),1);
```

Finally, the *a* matrix is the implementation of $\pm F_s - cF_0$ in equation (2.13). The use of the *b* vector will become clear later on.

3.5.1.2 The azimuth and elevation difference constraints

The azimuth and elevation difference constraints are set up exactly as was done for the sum constraints, with the only difference being that F_0 occurs at different coordinates on the (ϕ, θ) plane. An initial guess on these coordinates is easily found be simply evaluating the array factor for the antenna geometry with the antenna weights *J* all equal to 1.

For the azimuth difference constraints, the coordinate was found to be:

```
Max_Directivity_Theta=8.5;
Max_Directivity_Phi=0;
```

While for the elevation difference constraints the coordinate was found to be:

```
Max_Directivity_Theta=8;
Max_Directivity_Phi=90;
```

The side lobe constraints are also iteratively found by starting with 0 dB constraint levels and systematically lowering the constraints and tightening the angles at which these constraints apply. This is all done simultaneously with the sum constraints until the sequential quadratic programme cannot find a solution that satisfies all the constraints anymore.

The lowest azimuth difference constraints were found to be:

```
Phi0=0:1:90;
Theta0=0:0.5:90;

[Phi,Theta]=meshgrid(Phi0,Theta0);
C=zeros(size(Phi));
C(Theta>=22.5)=-17;
C(Theta>=42)=-18;
C(Theta>=18 &  Phi>=45)=-19;
```

While the elevation difference constraints were found to be:

```
Phi0=0:1:90;
Theta0=0:0.5:90;

[Phi,Theta]=meshgrid(Phi0,Theta0);
C=zeros(size(Phi));
C(Theta>=22.5)=-17;
C(Theta>=42)=-18;
C(Theta>=18 &  Phi<=45)=-19;
```

F_s and F_0 for the azimuth difference constraints is calculated as

```
index=1;
for phi=1:size(Phi,2);
  for theta=1:size(Theta,1);
    for n=1:N
      u=sin(Theta(theta,phi)*pi/180)*cos(Phi(theta,phi)*pi/180);
      v=sin(Theta(theta,phi)*pi/180)*sin(Phi(theta,phi)*pi/180);
      Fs(n,index)   =     sin(k*xn(n)*u)*...
                          cos(k*yn(n)*v)*...
                          cos(Theta(theta,phi)*pi/180);
     end;
     index=index+1;
   end;
 end;



for n=1:N
   u=sin(Max_Directivity_Theta*pi/180)*cos(Max_Directivity_Phi);
   v=sin(Max_Directivity_Theta*pi/180)*sin(Max_Directivity_Phi);
   F0(n,1)=    sin(k*xn(n)*u)*...
               cos(k*yn(n)*v)*...
               cos(Max_Directivity_Theta*pi/180);
end;
```

while F_s and F_0 for the elevation difference constraints is calculated as

```
index=1;

for phi=1:size(Phi,2);
  for theta=1:size(Theta,1);
    for n=1:N
      u=sin(Theta(theta,phi)*pi/180)*cos(Phi(theta,phi)*pi/180);
      v=sin(Theta(theta,phi)*pi/180)*sin(Phi(theta,phi)*pi/180);
      Fs(n,index)   =     cos(k*xn(n)*u)*...
                          sin(k*yn(n)*v)*...
                          cos(Theta(theta,phi)*pi/180);
     end;
     index=index+1;
   end;
 end;


for n=1:N
   u=sin(Max_Directivity_Theta*pi/180)*cos(Max_Directivity_Phi);
   v=sin(Max_Directivity_Theta*pi/180)*sin(Max_Directivity_Phi);
   F0(n,1)=    cos(k*xn(n)*u)*...
               sin(k*yn(n)*v)*...
               cos(Max_Directivity_Theta*pi/180);
end;
```

3.5.1.3 The Sequential Quadratic Programme

MATLAB has a built in function called *quadprog* which is part of its optimization toolbox. It is outside the scope of this work to develop a sequential quadratic code, so the built-in function is used instead. Calling the function quadprog(*B,F0,a,b*) attempts to minimize *Q* by finding the appropriate vector *J*.

$$Q[J] = \frac{1}{2}J^T BJ + J^T F_0 \tag{3.34}$$

Subject to

$$Ja \leq b \tag{3.35}$$

It can now be seen why b is for the purposes of this work set to a vector of zeros. With *a* calculated as discussed in section 3.5.1.1, equation (3.35) is the direct implementation of equation (2.13). Since there is a factor of 0.5 in (3.34), the *B* matrix as calculated in equations (3.25) to (3.27) is simply multiplied by 2. Lastly, we have to multiply $J^T F_0$ by -1 to get equation (2.12) into the form of (3.34). The code below shows how the sequential quadratic programme is implemented in MATLAB. The weights of (3.32) were kept equal similar to what McNamara [7] has done, and the constraints were just individually adjusted for the sum and difference patterns.

```
%%%%%%%%%%%%%%%%%%%%%%%%%%%%%%%%%%%%%%%%%%%%%%%%%%%%%%%%%%%%%%%%
% CONSTRAINT ANGLES AND CONSTRAINT LEVELS
[asum,bsum,F0sum]=Sum_Constraints(N,k,xn,yn);
[adaz,bdaz,F0daz]=Azimuth_Difference_Constraints(N,k,xn,yn);
[adel,bdel,F0del]=Elevation_Difference_Constraints(N,k,xn,yn);

%%%%%%%%%%%%%%%%%%%%%%%%%%%%%%%%%%%%%%%%%%%%%%%%%%%%%%%%%%%%%%%%
% QUADRATIC PROGRAM

sum_weight=1;
az_difference_weight=1;
el_difference_weight=1;

a=cat(1,asum,adaz,adel);
b=cat(1,bsum,bdaz,bdel);

B=2.*sum_weight.*Bsum   +   2.*az_difference_weight.*Bdaz   +
2.*el_difference_weight.*Bdel;
```

```
F=-sum_weight.*F0sum'   -   az_difference_weight.*F0daz'    -
el_difference_weight.*F0del';

opts = optimoptions('quadprog','Algorithm','interior-point-
convex','Display','iter');

[J fval eflag output lambda] =
quadprog(B,F,a,b,[],[],zeros(1,N),ones(1,N),[],opts);
```

3.6 MONOPULSE PATTERN SYNTHESIS USING THE GENETIC ALGORITHM

The genetic algorithm was included in this work, as a comparison to the sequential quadratic programme to finding the weights that would lead to optimal side lobe levels in the sum and difference patterns of a 2D monopulse array. As has been alluded to in section 2.5.2 the cost function for a genetic algorithm is critical to the performance of the algorithm. Although finding the best cost function for the simultaneous optimization of the sum and difference pattern side lobes for a monopulse antenna is outside the scope of this work, some experimentation has been done to find a cost function that works reasonably well. Initially the cost function is simply given as

$$C = \sum J^T F(\phi,\theta) - M(\phi,\theta) \tag{3.36}$$

$$J^T F(\phi,\theta) - M(\phi,\theta) = 0 \; if \; J^T F(\phi,\theta) - M(\phi,\theta) < 0 \tag{3.37}$$

Here, M is the constraints masks defined over (ϕ,θ), and is identical to the constraints applied with the quadratic programme.

This cost function works, but the genetic algorithm can easily provide a solution where the side lobe level is reached everywhere except at a single point, where there could be a large difference between the side lobe level requirement (mask) and the actual side lobe level achieved. Since this happens at only a single point, the total cost function is relatively low. It is much better to achieve a radiation pattern that fails to meet the mask at many points, but only by say 0.1 dB than to have a radiation pattern that fails to meet the mask at 2 or three points only, but by 3 dB. Therefore, a way is found that will add proportionally

higher cost to the side lobe level of a specific chromosome if it fails to meet the mask at increasing values. A simple way of doing this is to modify equation (3.36) to

$$C = \sum [J^T F(\phi,\theta) - M(\phi,\theta)]^4 \tag{3.38}$$

$$J^T F(\phi,\theta) - M(\phi,\theta) = 0 \; if \; J^T F(\phi,\theta) - M(\phi,\theta) < 0 \tag{3.39}$$

This way, a single point failing to meet the mask by 3 dB will be penalised more than 12 points failing to meet the mask by 1 dB. The rest of the Genetic algorithm parameter is given in Table 3.6 below.

Table 3.6. Genetic Algorithm Parameters.

Parameter	Value
Population Size	100
Natural Selection Method	Cost Ranking
Size of population after Natural Selection	50%
Mating	Pairing Top to Bottom
Mutation Rate (Cost Function>2)	3%
Mutation Rate (Cost Function<2)	1%

3.6.1 The genetic algorithm implemented in MATLAB

The genetic algorithm starts with generating a random population of chromosomes as follows.

```
for i=1:npop

     J=rand(N_Elements,1);
% 16 Elements in Q1 of the 64 Element ]Array
```

```
Sum_Cost          =     Calculate_Cost(J,xn,yn,B_SUM,B_AZD,B_ELD,f0,1,...
                                       angular_resolution,pi/2,pi/2);
Az_Diff_Cost      =     Calculate_Cost(J,xn,yn,B_SUM,B_AZD,B_ELD,f0,2,...
                                       angular_resolution,pi/2,pi/2);
El_Diff_Cost      =     Calculate_Cost(J,xn,yn,B_SUM,B_AZD,B_ELD,f0,3,...
                                       angular_resolution,pi/2,pi/2);

 Total_Cost=Sum_Cost+Az_Diff_Cost+El_Diff_Cost;
population=[population; J',Total_Cost];

end;

population=sortrows(population,N_Elements+1);
```

The function Calculate_Cost basically calculates the relevant directivity pattern for each chromosome in the population, and compares this to the mask. It applies equations (3.38) and (3.39) to arrive at the cost for the particular chromosome. The total cost is then calculated by simply adding the costs from the three directivities for the antenna. The population is then arranged in a matrix with npop rows and the genes of each chromosome across the columns. The last column contains the total cost of the particular chromosome. The population matrix is then sorted with costs ranging from low to high.

The code snippet below shows how the function Calculate_Cost works.

```
%% Calculate the Directivity
[D_SUM,Max_SUM]=AF(J,xn,yn,B_SUM,f0,1,angular_resolution,...
                   theta_range,phi_range,35,0,0);
[D_AZD,Max_AFD]=AF(J,xn,yn,B_AZD,f0,2,angular_resolution,...
                   theta_range,phi_range,35,0,0);

[D_ELD,Max_ELD]=AF(J,xn,yn,B_ELD,f0,3,angular_resolution,...
                   theta_range,phi_range,35,0,0);

D_SUM=D_SUM-max(max(D_SUM));
D_AZD=D_AZD-max(max(D_AZD));
D_ELD=D_ELD-max(max(D_ELD));


%% Calculate the Cost
Cost=[];
if (Channel==1)
    C_Sum=Sum_Mask(angular_resolution,theta_range,phi_range,0,0);
    Cost=D_SUM-C_Sum;
    Cost(Cost<0)=0;
    Cost=sum(sum(Cost.^4));
end;
```

```
if (Channel==2)
    C_AZD=Azimuth_Difference_Mask(angular_resolution,theta_range,...
                                  phi_range,0,0);
    Cost=D_AZD-C_AZD;
    Cost(Cost<0)=0;
    Cost=sum(sum(Cost.^4));
end;

if (Channel==3)
    C_ELD=Elevation_Difference_Mask(angular_resolution,theta_range,...
                                    phi_range,0,0);
    Cost=D_ELD-C_ELD;
    Cost(Cost<0)=0;
    Cost=sum(sum(Cost.^4));
end;
```

The function AF calculates the directivity over (ϕ, θ) by implementing equation (2.11). The mask functions are implemented below. For the sum mask we have

```
% CONSTRAINT ANGLES AND LEVELS

            Phi0=0:angular_resolution:phi_range;
            Theta0=0:angular_resolution:theta_range;

            [Phi,Theta]=meshgrid(Phi0,Theta0);
            C=zeros(size(Phi));

% SIMULTANEOUS CONSTRAINTS
               C(Theta>=15*pi/180)=-17;
               C(Theta>=23*pi/180)=-20;
```

For the azimuth difference mask we have

```
% CONSTRAINT ANGLES AND LEVELS

            Phi0=0:angular_resolution:phi_range;
            Theta0=0:angular_resolution:theta_range;

            [Phi,Theta]=meshgrid(Phi0,Theta0);
            C=zeros(size(Phi));

% COMMENT THESE IF ONLY SUM CONSTRAINTS ARE OPTIMIZED
              C(Theta>=22.5*pi/180)=-17;
              C(Theta>=42*pi/180)=-18;
              C(Theta>=18*pi/180 &  Phi>=45*pi/180)=-19;
```

And for the elevation difference mask we have

```
% Constraint Angles and Levels

            Phi0=0:angular_resolution:phi_range;
            Theta0=0:angular_resolution:theta_range;

            [Phi,Theta]=meshgrid(Phi0,Theta0);
            C=zeros(size(Phi));

% COMMENT THESE IF ONLY SUM CONSTRAINTS ARE OPTIMIZED
              C(Theta>=22.5*pi/180)=-17;
              C(Theta>=42*pi/180)=-18;
              C(Theta>=18*pi/180 &  Phi<=45*pi/180)=-19;
```

Once we have the initial random population with their associated costs sorted from low to high, only the top 50% of the population is selected for mating. The mates are also selected in pairs from top to bottom. The mating process is gene blending according to equation (2.17) with β equals to a random number between 0 and 1. The new population is then made up of the original 50% of parents, while the newly created offspring makes up the other 50% of the population. Lastly, some of the genes are mutated in the new population according to the mutation rate. Once the new population is created, the process repeats itself with calculating the costs for each chromosome in the population. The process continues for a maximum of 250 iterations, or until the cost function is 0.

```
% Random number that determines amount of genetic material
% passed from each parent
B=rand(1);

% Mating
for n=1:2:nkeep-1
    off_spring(n,1:N_Elements)=population(n,1:N_Elements)*B+...
                               population(n+1,1:N_Elements)*(1-B);
    off_spring(n+1,1:N_Elements)=population(n+1,1:N_Elements)*B+...
                                 population(n,1:N_Elements)*(1-B);
end;


% New Population

population=[population(1:nkeep,1:N_Elements);
off_spring(1:nkeep,1:N_Elements)];

% Mutation
x_indexes=ceil(rand(n_mutations,1)*N_Elements);
```

```
y_indexes=ceil(rand(n_mutations,1)*npop);
s=sub2ind([npop N_Elements+1],y_indexes(:,1),x_indexes(:,1));
population(s)=rand(1);
```

3.7 ANTENNA DESIGN FOR OPTIMUM SIDE LOBES

3.7.1 Optimization of excitations to produce simultaneously optimized sum and difference patterns

Knowing the general form of the directivity for the equally excited antenna, it is possible to use the sequential quadratic programme to find the element weights that will yield the directivities with optimal side lobe levels for the sum and difference patterns simultaneously. The constraints for each pattern are a function of its peak directivity, so it is important to know where the peak of the directivity is located. For the sum channel, peak directivity is a θ = 0°. For the azimuth difference pattern, the peak directivity is at (ϕ, θ) = (0, 8.5)°, while for the elevation difference pattern this is at (ϕ, θ) = (90, 7.5)°. The side lobe levels for the sum pattern is already quite favorable even for the equally excited case, so the sum constraints are at first constructed to match these side lobe levels. The side lobe levels for the two difference channels are then gradually reduced until the quadratic programme discussed in section 3.5 cannot find solutions anymore. The resulting constraints are shown in Figure 3.36 and the element weights that satisfy these constraints are shown in Figure 3.37. The resultant radiation patterns (shown in Figure 3.38) have side lobe levels that are at or below the constraint levels. This would be a first iteration of the tapered excitation design. In this first iteration, the antenna geometry for the equal excitation is used as input. Generally, the tapering will lead to differences in the dipole spacing or phase centers when designing the physical antenna. A second iteration will usually get good agreement between the antenna geometry used for the optimization, and the resultant geometry obtained from the 3D full wave design process. From the excitation taper and the required input impedance it is possible to derive each element's radiation resistance. The radiation resistance for element *i* of a total of *n* elements is calculated from the excitation taper and required input impedance as

$$Z_R(i) = \frac{Z_0}{J(i)} \sum_{k=1}^{n} J(k) \tag{3.40}$$

Here, Z_0 is the required input impedance of the complete array. Once again, these values are the radiation resistances that each dipole would present to the array. When the dipole lengths and width are determined in CST using the geometry shown in Figure 3.3, the measured impedance at the port is set to exactly half of the calculated values.

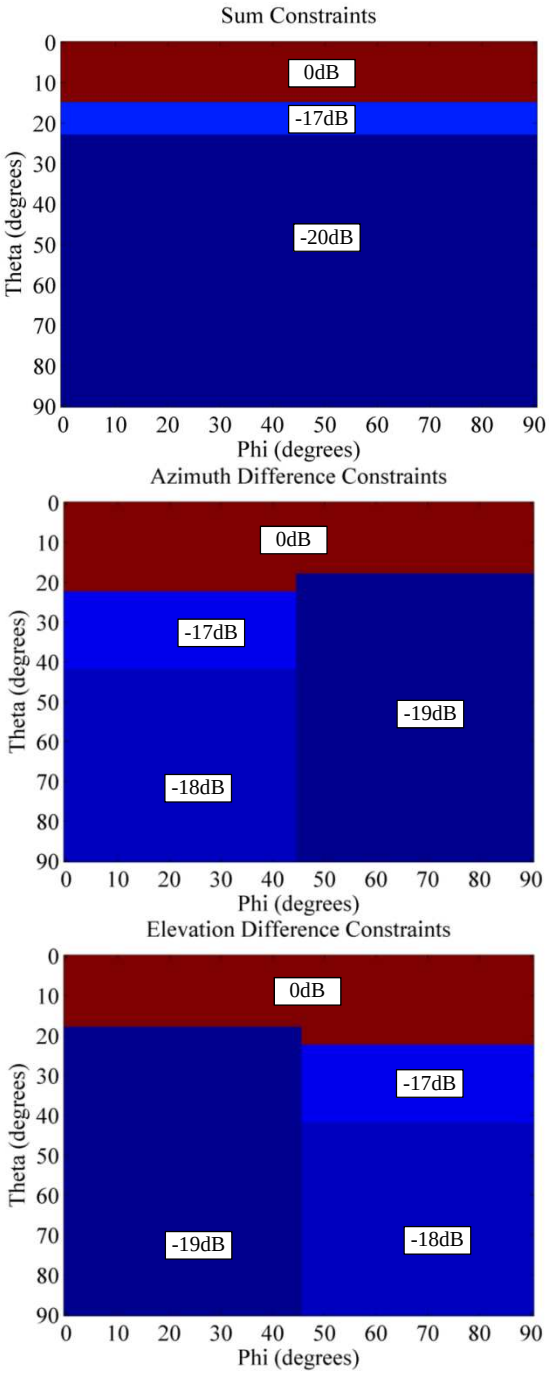

Figure 3.36: Sum Azimuth- and Elevation difference constraints for simultaneous optimized low side lobes.

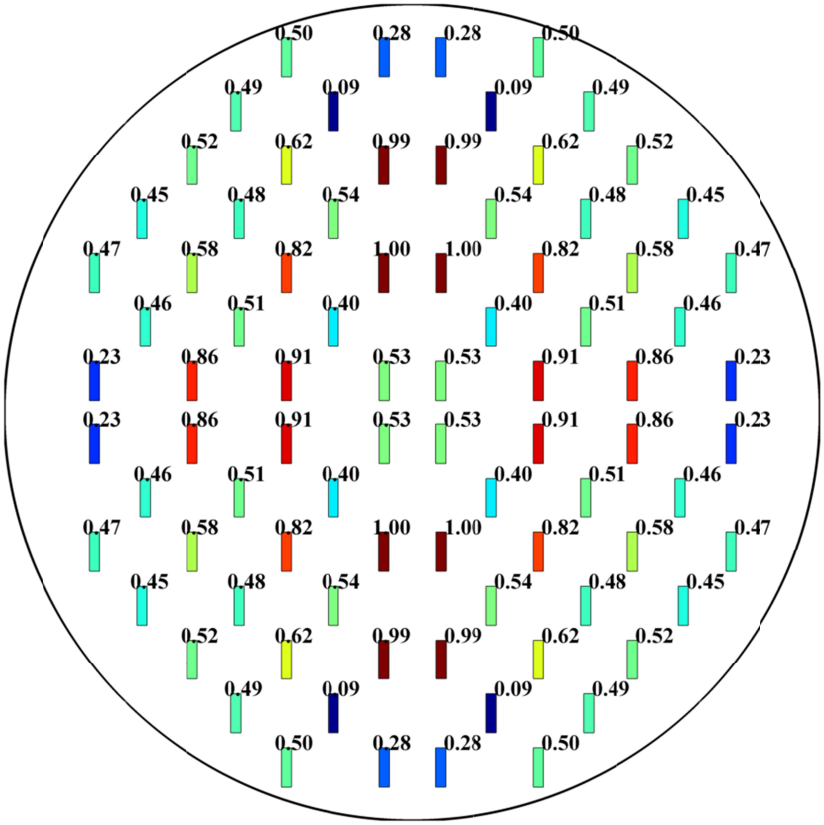

Figure 3.37. Optimized element weights for the geometry of Figure 3.32 and the constraints of Figure 3.36.

At this point, it is a good idea to check what the genetic algorithm can achieve. The same constraint levels were presented to the genetic algorithm. Fifty runs of the genetic algorithm were done, and each run was allowed 250 generations. On average the cost function was reduced by around 45 dB. This reduction is achieved in an average of around 100 generations. The best run reduced the cost function by 55 dB while the worst run reduced the cost function by 38 dB. This is shown in Figure 3.39. In none of these cases could the genetic algorithm achieve the solution which the sequential quadratic programme found.

It is important to note that the genetic algorithm came extremely close. And should the cost function and other genetic algorithm parameters be optimized, the solution could indeed be found. This is however good evidence that the sequential quadratic programme is indeed a very good choice for the optimization of simultaneous sum and difference side lobe levels for monopulse antennas.

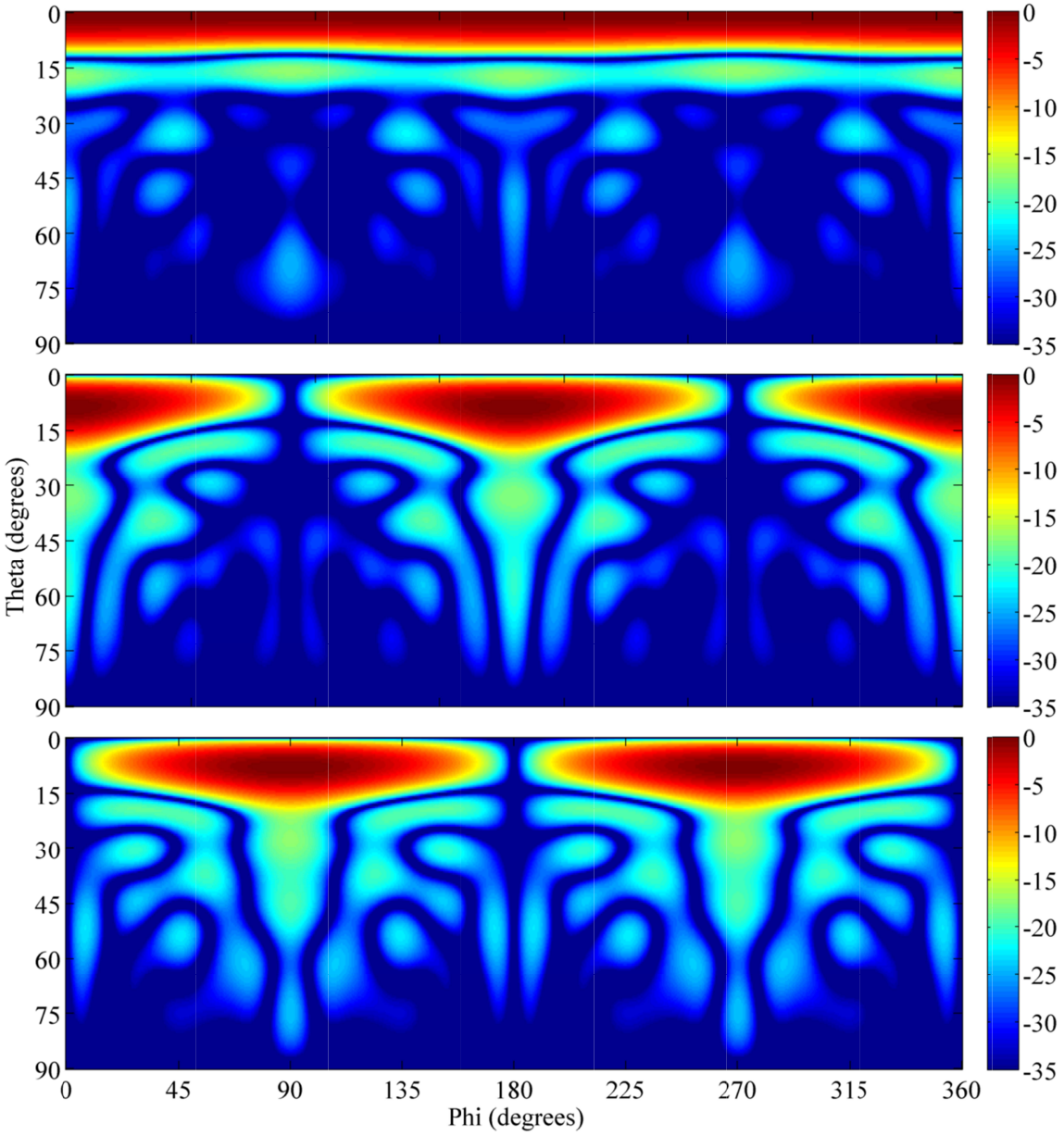

Figure 3.38. Resulting normalized radiation pattern calculated by a MATLAB script using the sequential quadratic programme for the geometry and excitation of the tapered monopulse antenna array of Figure 3.37. From top to bottom is sum, azimuth difference and elevation difference patterns. The colour bar is in dB.

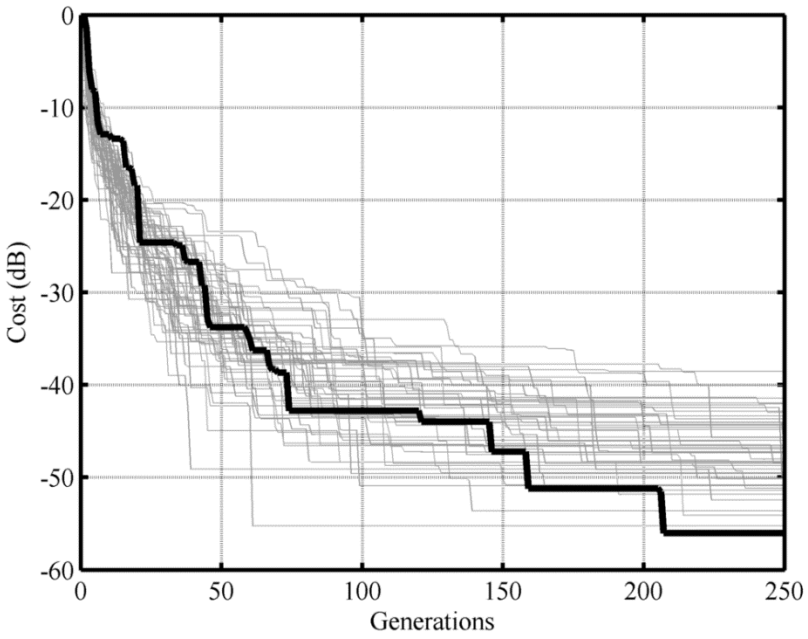

Figure 3.39. The cost function of 50 runs of the genetic algorithm as a function of generation.

As reference, the worst performing genetic algorithm solution is shown Figure 3.40. The grey areas are the areas on the (ϕ, θ) plane where the solution match or is better than the mask requirements. The red areas are the areas where the solution exceeds the mask requirements. It is obvious that these areas are few. The maximum value by which the sum mask is exceeded is 0.8 dB, the maximum value by which the azimuth difference mask is exceeded is 1.1 dB and the maximum value by which the elevation difference mask is exceeded is 0.9 dB. The best performing genetic algorithm result is shown in Figure 3.41. Here the sum mask exceeded by a maximum of 0.2 dB, the azimuth difference mask is exceeded by 1 dB and the elevation difference mask is exceeded by 0.5 dB.

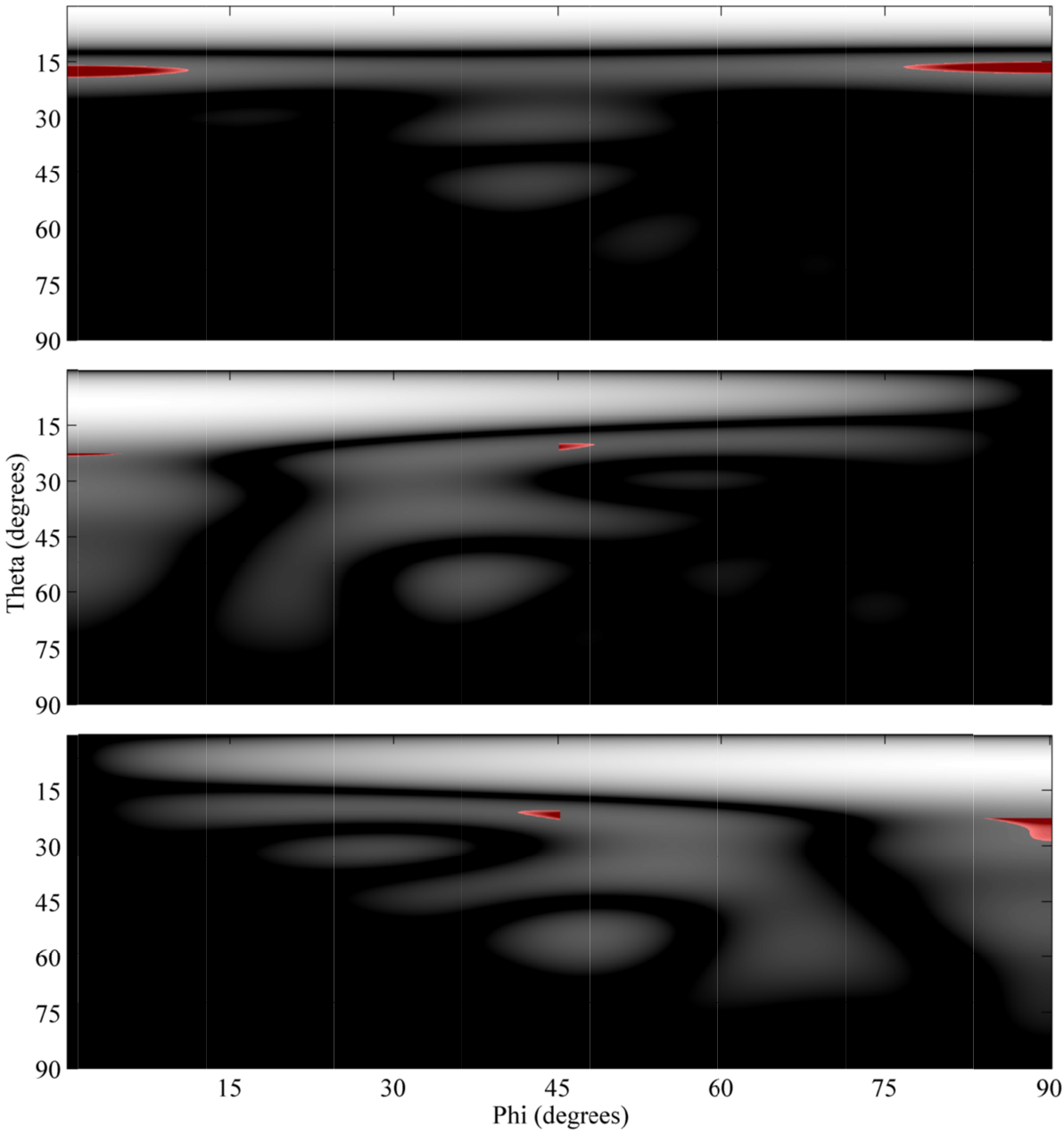

Figure 3.40. Areas where the worst performing genetic algorithm run failed to meet the mask requirements. From top to bottom is sum, azimuth difference and elevation difference patterns.

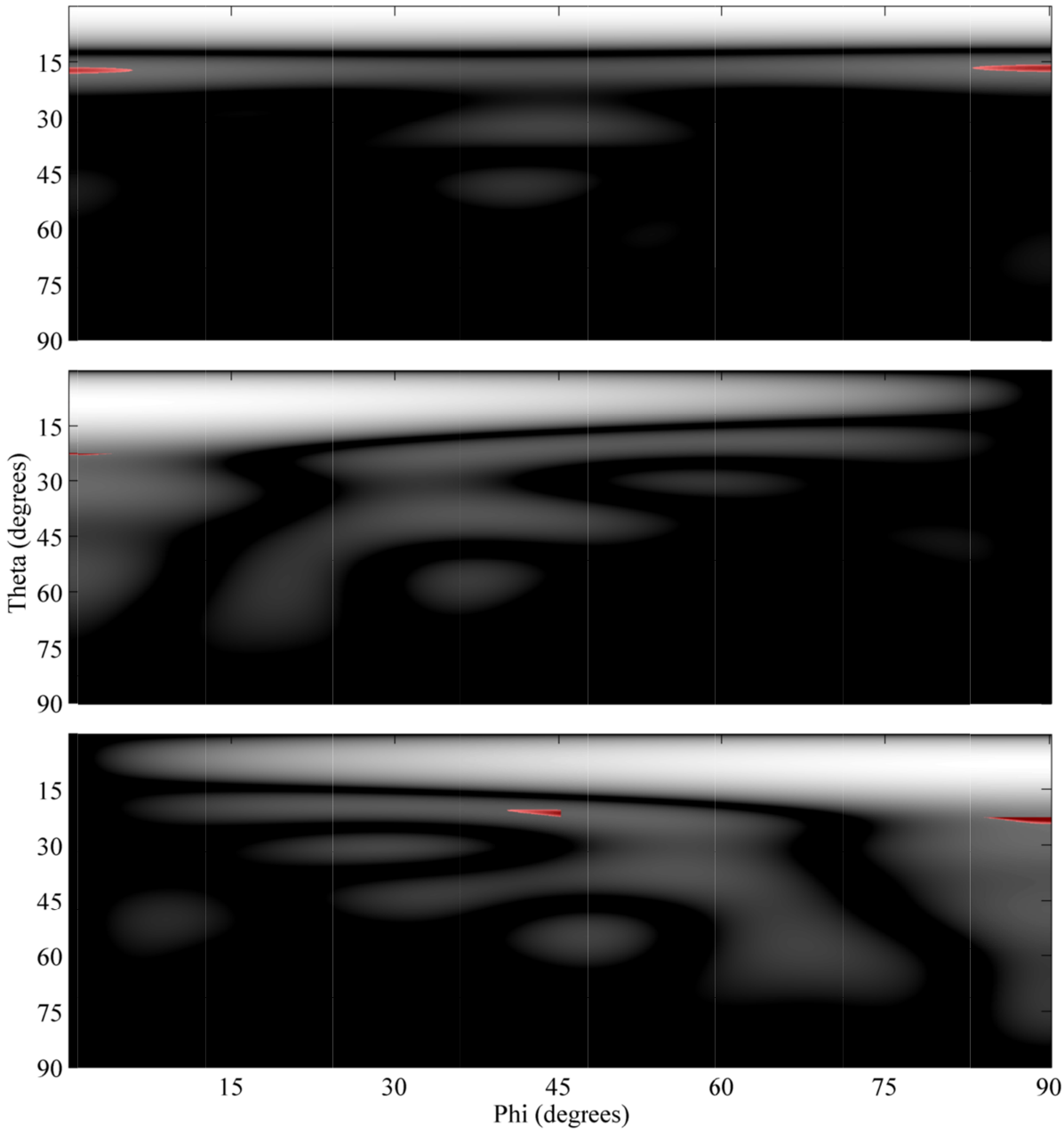

Figure 3.41. Areas where the best performing genetic algorithm run failed to meet the mask requirements. From top to bottom is sum, azimuth difference and elevation difference patterns.

From the required excitation vector (calculated by the sequential quadratic programme), and using equation (3.40) the required dipole radiation resistances are calculated, and shown below in Figure 3.42.

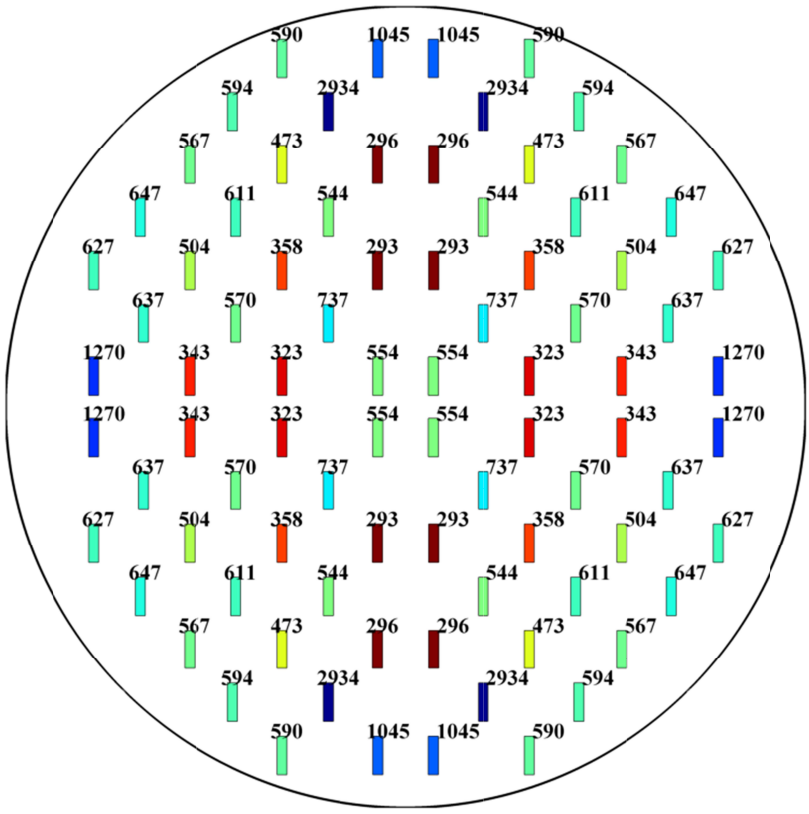

Figure 3.42. Radiation resistances presented by each dipole to produce the required weights and antenna input impedance.

The antenna geometry with the element excitation is shown in Figure 3.37. Once again the dipole numbering is as per Figure 3.5. The dipoles are optimized to be resonant, and have the required radiation resistance. The results are shown in Table 3.7. The radiation resistance is the resistance measured at the dipole edge.

Table 3.7. Resultant Dipoles with their simulated radiation resistances and dimensions.

Dipole Number	Radiation Res. [Ω]	Dipole Length [mm]	Dipole Width [mm]	Dipole Number	Radiation Res. [Ω]	Dipole Length [mm]	Dipole Width [mm]
1	554	5.355	1.5831	11	627	5.406	1.4089
2	323	5.173	2.4794	12	544	5.348	1.6098
3	343	5.189	2.3709	13	611	5.396	1.4443
4	1270	5.730	0.6571	14	647	5.419	1.3667
5	737	5.472	1.2019	15	296	5.151	2.6422
6	570	5.367	1.5420	16	473	5.295	1.8232
7	637	5.413	1.3871	17	567	5.365	1.5496
8	293	5.148	2.6638	18	2934	6.070	0.2000
9	358	5.202	2.2912	19	594	5.348	1.4835
10	504	5.319	1.7244	20	1045	5.638	0.8120
				21	590	5.381	1.4930

Next, the modules were designed and optimized. The modules were first individually optimized for phase. The H-modules are optimized first. The I-modules have the same dipole dimensions as their corresponding free resonating dipole prototypes and their feed lengths are then adjusted so that the phase of S_{11} is 180°. The T-module dipole lengths are adjusted first to show resonance at the operating frequency. Thereafter their feed lengths are adjusted to provide a 180° phase differential between the ports. The U-modules are optimized in the same way as the T-modules but with a 0° phase requirement. The module dimensions are given in Table 3.8.

Table 3.8. Individual optimized module dimensions.

Module Number	Dipole Length [mm]	Dipole Width [mm]	Feed Length [mm]	Dipole Number [mm]	Dipole Length [mm]	Dipole Width [mm]	Feed Length [mm]
1	5.355	1.5831	3.160	11	5.406	1.4089	3.150
2	5.674	2.4794	2.400	12	7.798	1.6098	2.345
3	5.695	2.3709	2.434	13	7.715	1.4443	2.439
4	5.730	0.6571	3.150	14	5.544	1.3667	3.179
5	7.598	1.2019	2.579	15	5.380	2.6422	2.760
6	7.763	1.5420	2.384	16	7.910	1.8232	2.225
7	7.687	1.3871	2.472	17	5.915	1.5496	2.670
8	5.380	2.6638	2.760	18	7.191	0.2000	3.124
9	7.200	2.2912	2.300	19	5.527	1.4835	3.141
10	7.857	1.7244	2.280	20	5.638	0.8120	3.150
				21	5.934	1.4930	2.687

Next, the microstrip wire grid array is constructed. In order to do this, the common horizontal spacing D_x must be determined first. D_x is found by the average of the H-module horizontal dimensions, but because the feed module phasing is more important than the other modules for impedance bandwidth [3], D_x is found by first calculating the average horizontal dimensions for the H-modules only. The average of this value and the horizontal dimension of the feed module then results in D_x which is 6.600 mm in this case. When the average horizontal dimension is enforced on the H-modules, the phasing of the H-modules changes. For the H-modules, S_{21} is fixed because of the horizontal constraint, but S_{31} and S_{41} can be re-optimized to 0°. This is done by changing the dipole lengths of the H-modules. The new lengths for these dipoles are shown in Table 3.9 below.

Table 3.9. Updated dimensions of the H-modules to account for the change in their feed lengths.

Module Number	Dipole Length [mm]	Dipole Width [mm]	Feed Length [mm]
5	7.5352	1.202	2.6991
6	7.4631	1.542	2.5290
7	7.4138	1.387	2.6065
9	7.2000	2.664	1.968
10	7.5251	1.724	2.4378
12	7.4864	1.610	2.4951
13	7.4312	1.444	2.5779
16	7.5534	1.823	2.3884
18	7.0684	0.2	3.2000

Once these new lengths of the H-modules are found, the vertical spacing which is the average of the H-module heights can be calculated. D_y is calculated to be 7.409 mm. The dipole lengths and widths in Table 3.8 are used to construct the wire grid array, with D_x and D_y already determined from the H-modules. Using the same idea as was done for the equally excited antenna, the T-modules are now re-examined. For the tapered antenna, the feed lengths between dipole 2 and 5 as well as dipole 2 and 6 are measured on the constructed wire grid antenna. The sum of these lengths minus the feed length allocation from the H-modules of dipole 5 and 6 yields twice the feed length of dipole 2. Half of this value is therefore used to re-optimize the T-module of dipole 2. The concept is shown in Figure 3.43 below.

$$L52_{Measured} + L62_{Measured} - L5_{feed\ length} - L6_{feed\ length} = 2L2_{feed\ length} \qquad (3.41)$$

This is an iterative process, because as soon as a new T-module length is found, this will affect the measured feed length on the constructed wire grid antenna. Normally, after around 3 iterations convergence is reached between the feed lengths and dipole lengths.

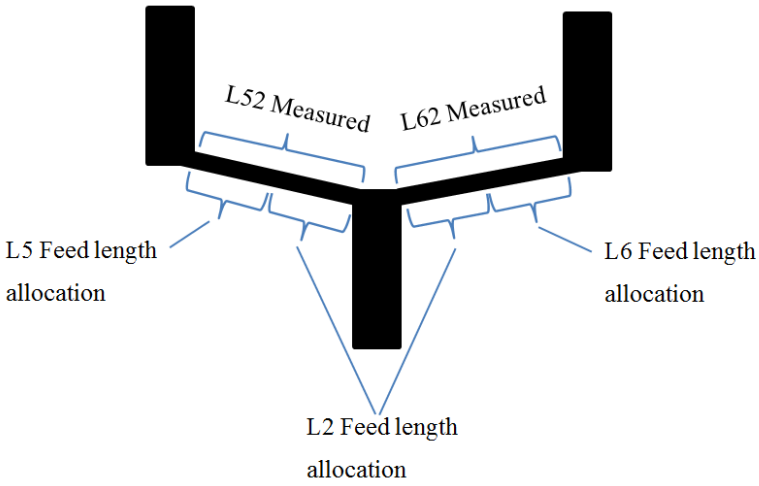

Figure 3.43. Determining the feed line length allocated to the T-module of dipole 2.

The same is done for the T-Modules of dipole 3, 17 and 21. The new dimensions of the T-modules are listed in Table 3.10.

Table 3.10. Updated lengths of the T-modules to account for the change in their feed lengths.

Module Number	Dipole Length [mm]	Dipole Width [mm]	Feed Length [mm]
2	6.1090	2.4794	2.1364
3	6.1040	2.3709	2.1882
17	6.025	1.5496	2.6000
21	5.984	1.4930	2.6538

Lastly, the spacings for the U- and I-modules are adjusted on the constructed wire grid antenna (as was done for the equally excited antenna) until the measured feed lengths equal

the feed lengths calculated during the individual module optimization step. The final dipole spacing parameters are shown in Table 3.11.

Table 3.11. Final dipole spacing parameters.

Parameter	Dimension [mm]
D_x	6.6000
D_{x1}	3.8163
D_{x4}	3.3851
D_{x8}	3.9267
D_{x11}	3.7290
D_{x14}	3.7302
D_{x15}	3.9805
D_{x19}	3.8247
D_{x20}	3.4314
D_y	7.4050
$Feed_x$	17.300
$Feed_y$	19.100

3.7.2 Input match simulation results

A full wave 3D simulation shows that the single quadrant wire grid antenna is resonant at 17.71 GHz. Therefore, the grid spacing parameters, as well as the dipole lengths need to be scaled to get the resonance frequency to be at 18 GHz as required.

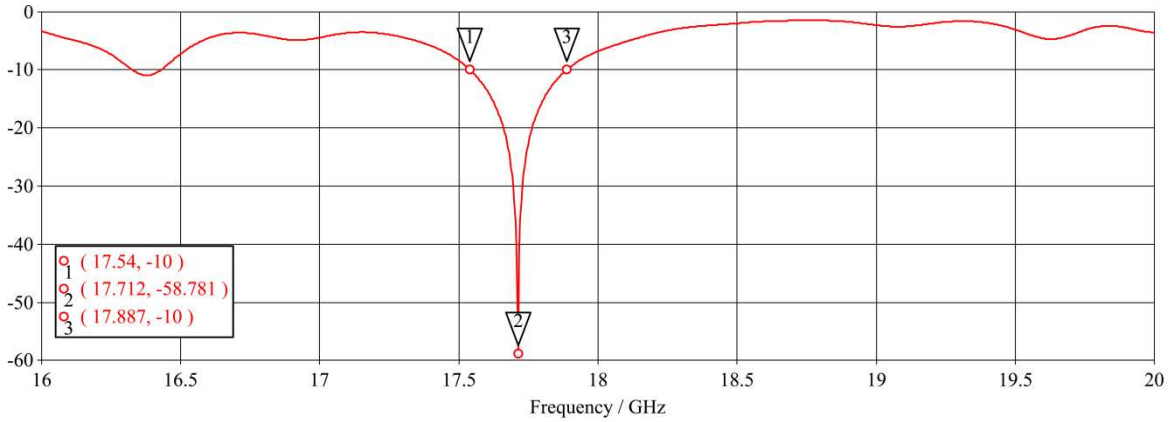

Figure 3.44. Full wave simulation, showing the resonance frequency of the antenna.

The scaling factor is simply 17.71/18, and the values of Table 3.8, Table 3.10 and Table 3.11 are scaled accordingly.

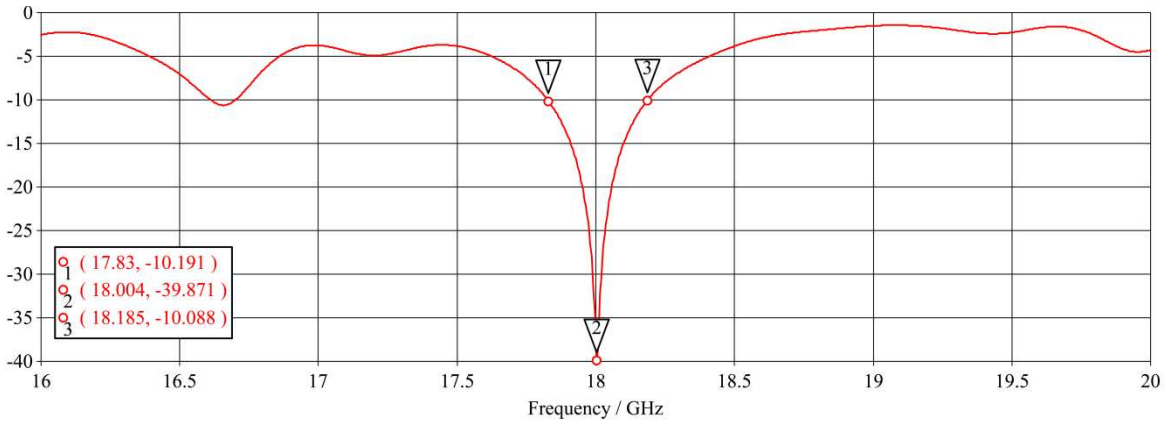

Figure 3.45. Input match of the scaled single quadrant microstrip wire grid antenna.

3.7.3 Second iteration design

The resultant scaling and adjustment of the spacing parameters to yield optimal phasing for the modules means that the layout of the antenna differs from the layout used to find the optimal weights. Therefore, the current antenna geometry is used to find the optimal weights again in a second iteration of the design. The differences in radiation resistances are shown in Table 3.12. It is clear that the general trend remains the same as far as the aperture weights are concerned; however, there are significant differences at some dipoles, such as dipole 4. Therefore, a second iteration of the design is done. The second iteration is done in exactly the same manner as the preceding section, but based on the new dipole radiation resistances. The final antenna parameters are shown in Table 3.13 and Table 3.14.

Table 3.12. Original dipole radiation resistance vs. dipole radiation resistance based on the scaled antenna geometry.

Dipole Number	Original Radiation Resistance [Ω]	New Radiation Resistance [Ω]	Dipole Number	Original Radiation Resistance [Ω]	New Radiation Resistance [Ω]
1	554	514	11	627	525
2	323	326	12	544	480
3	343	353	13	611	453
4	1270	2040	14	647	684
5	737	879	15	296	314
6	570	638	16	473	593
7	637	586	17	567	604
8	293	284	18	2934	2114
9	358	362	19	594	735
10	504	490	20	1045	1120
			21	590	496

Table 3.13. Final antenna dipole dimensions for the second iteration design.

Dipole Number	Dipole Length [mm]	Dipole Width [mm]	Dipole Number [mm]	Dipole Length [mm]	Dipole Width [mm]
1	5.327	1.695	11	5.335	1.663
2	5.855	2.462	12	7.591	1.801
3	5.822	2.316	13	7.584	1.892
4	5.983	0.299	14	5.550	1.292
5	7.285	0.995	15	5.392	2.532
6	7.433	1.385	16	7.465	1.486
7	7.470	1.502	17	5.678	1.460
8	5.377	2.723	18	7.092	0.256
9	6.800	2.271	19	5.568	1.205
10	7.530	1.768	20	5.673	0.744
			21	5.848	1.749

Table 3.14. Final antenna grid spacing parameters.

Parameter	Dimension [mm]
D_x	6.518
D_{x1}	3.709
D_{x4}	3.050
D_{x8}	3.774
D_{x11}	3.662
D_{x14}	3.636
D_{x15}	3.764
D_{x19}	3.602
D_{x20}	3.284
D_x	7.315
$Feed_x$	17.300
$Feed_y$	19.100

3.7.4 Input match of the second iteration design

Once again, the resonance of the antenna is lower than the expected 18 GHz by 150 MHz; therefore the antenna is scaled again by a factor of 17.85/18 to achieve the required resonance at 18 GHz.

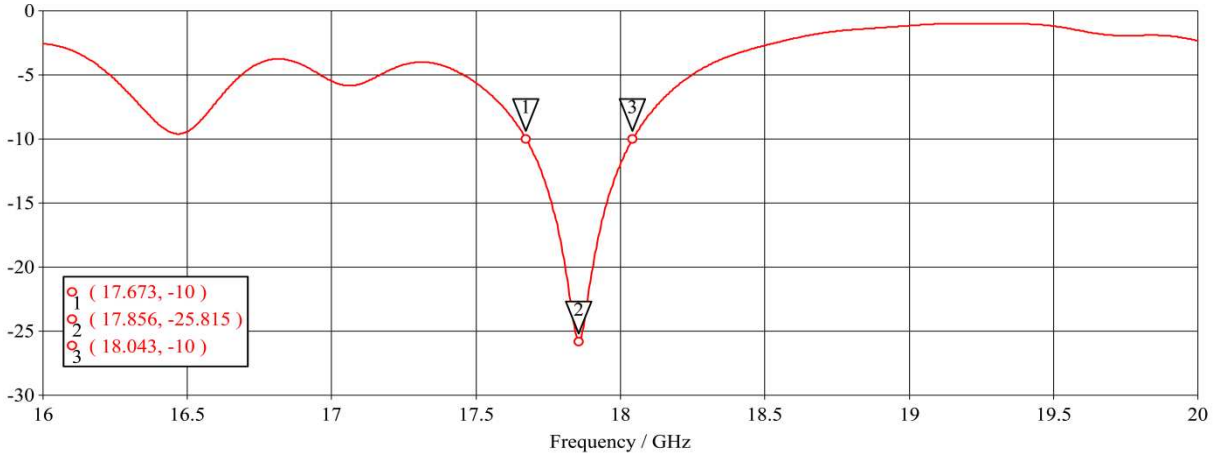

Figure 3.46. $|S_{11}|$ showing the resonance frequency of the second iteration design.

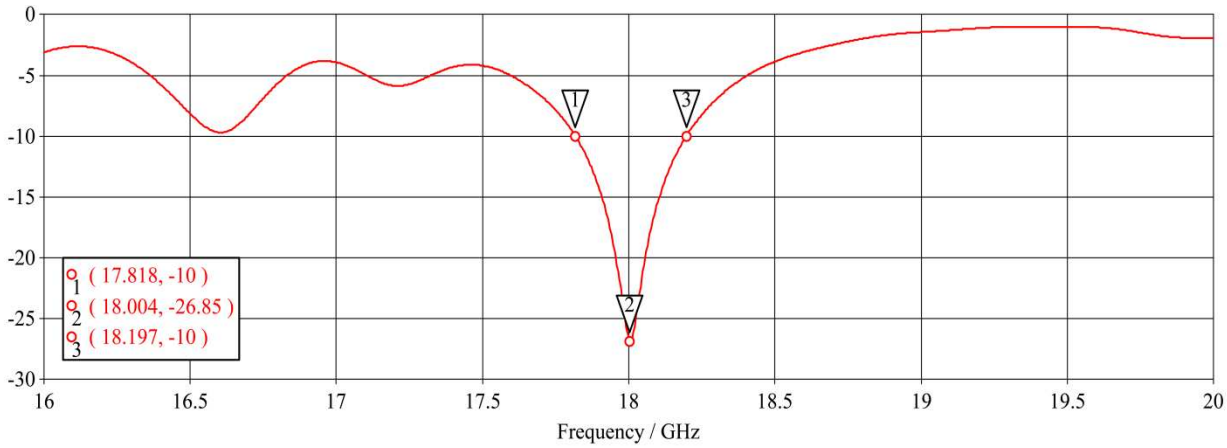

Figure 3.47. $|S_{11}|$ showing the resonance frequency of the second iteration design (Scaled).

3.7.5 Surface current simulation

The vertical currents are shown in Figure 3.48 below. A measurement was made regarding the phase the currents by measuring the phase at the center of each dipole. The results are shown in Table 3.15.

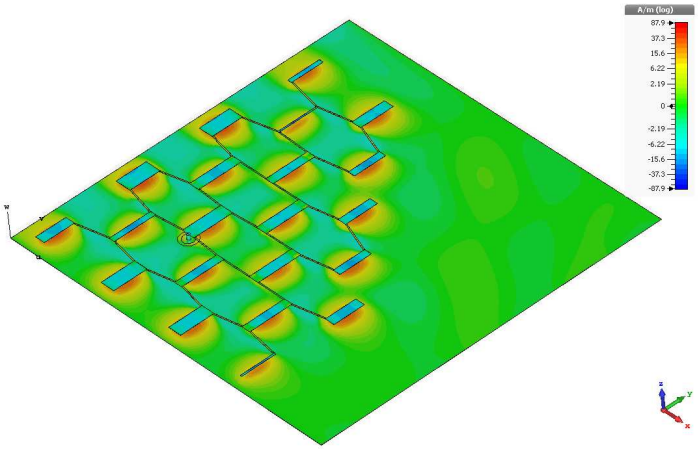

Figure 3.48. Vertical currents of the tapered microstrip wire grid array section.

Table 3.15. Dipole current phase.

Dipole Number	Dipole Phase (°)	Dipole Number	Dipole Phase (°)
1	167	11	173
2	172	12	168
3	177	13	172
4	167	14	168
5	163	15	186
6	166	16	170
7	169	17	173
8	178	18	168
9	145	19	174
10	170	20	169
		21	179

As can be seen, the currents are relatively in phase, with a total phase range of 15° for non-feed elements. The feed element has a phase of 145° which is not easily changeable. This is considerably different to the average phase of 167°. The feed element might therefore produce significant spurious radiation as a result. The resulting radiation patterns shows that the required masks are generally met, however, especially in the azimuth difference pattern the required mask is exceeded significantly. The radiation patterns in the principle planes for the tapered versus the equally excited design are shown in Figure 3.49, and detailed radiation patterns are shown in Figure 3.50. For the sum pattern shown in Figure 3.50, the mask is only exceeded at a single point by a maximum of 0.3 dB. For practical purposes the sum pattern therefore meets the mask requirements. The azimuth difference mask exceeds the mask requirements at various places. The biggest differences are at (θ, ϕ) = (31, 0)° and (31, 180)°. Here the mask requirements are exceeded by 2.1 dB. At (θ, ϕ) = (59, 0)° and (59, 180)° the mask is exceeded by 0.7 dB, while at (θ, ϕ) = (19, 60)° , (19, 120)° , (19, 240)° and (19, 300)° the mask is exceeded by 2 dB. Although the mask is exceeded, the overall side lobe level is still better than for the equally excited case. The elevation difference mask exceeds the mask requirements at couple of places. The biggest differences are at (θ, ϕ) = (21, 45)° , (21, 135)° , (21, 225)° and (21, 315)° .Here the mask requirements are exceeded by 1 dB.

At (θ, ϕ) = (80, 90)° and (80, 270)° the mask is exceeded by 0.5 dB. The elevation difference pattern is much better than the azimuth difference pattern. Once again, the pattern is better than for the equally excited case.

As a reference, and to show the improvement in both difference patterns, the equally excited patterns are shown in Figure 3.51. Tables with the value differences are also included.

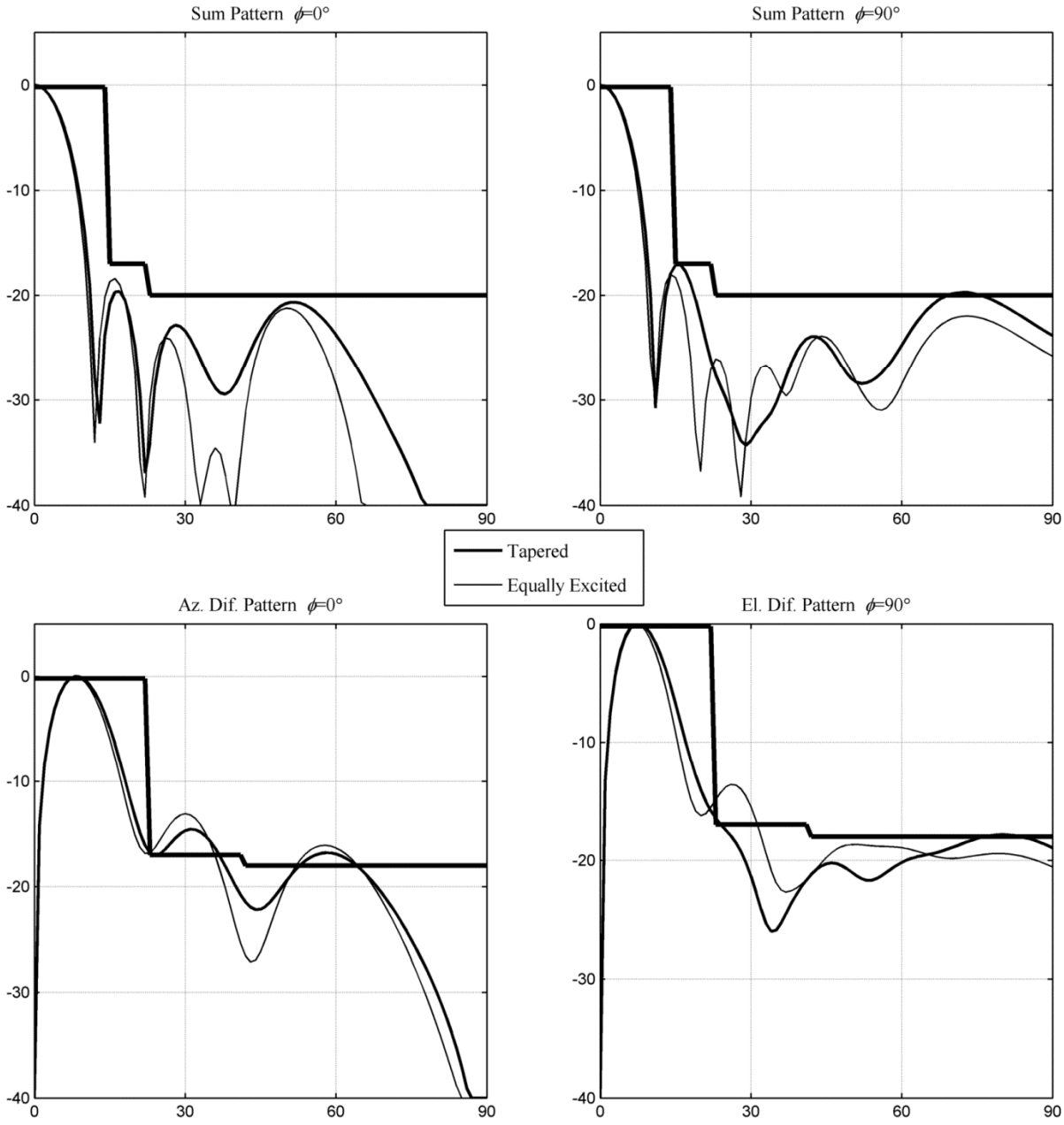

Figure 3.49. Principal plane patterns showing the differences between the equally excited antenna and the tapered antenna. The thick black lines represent the mask constraints in the principal planes.

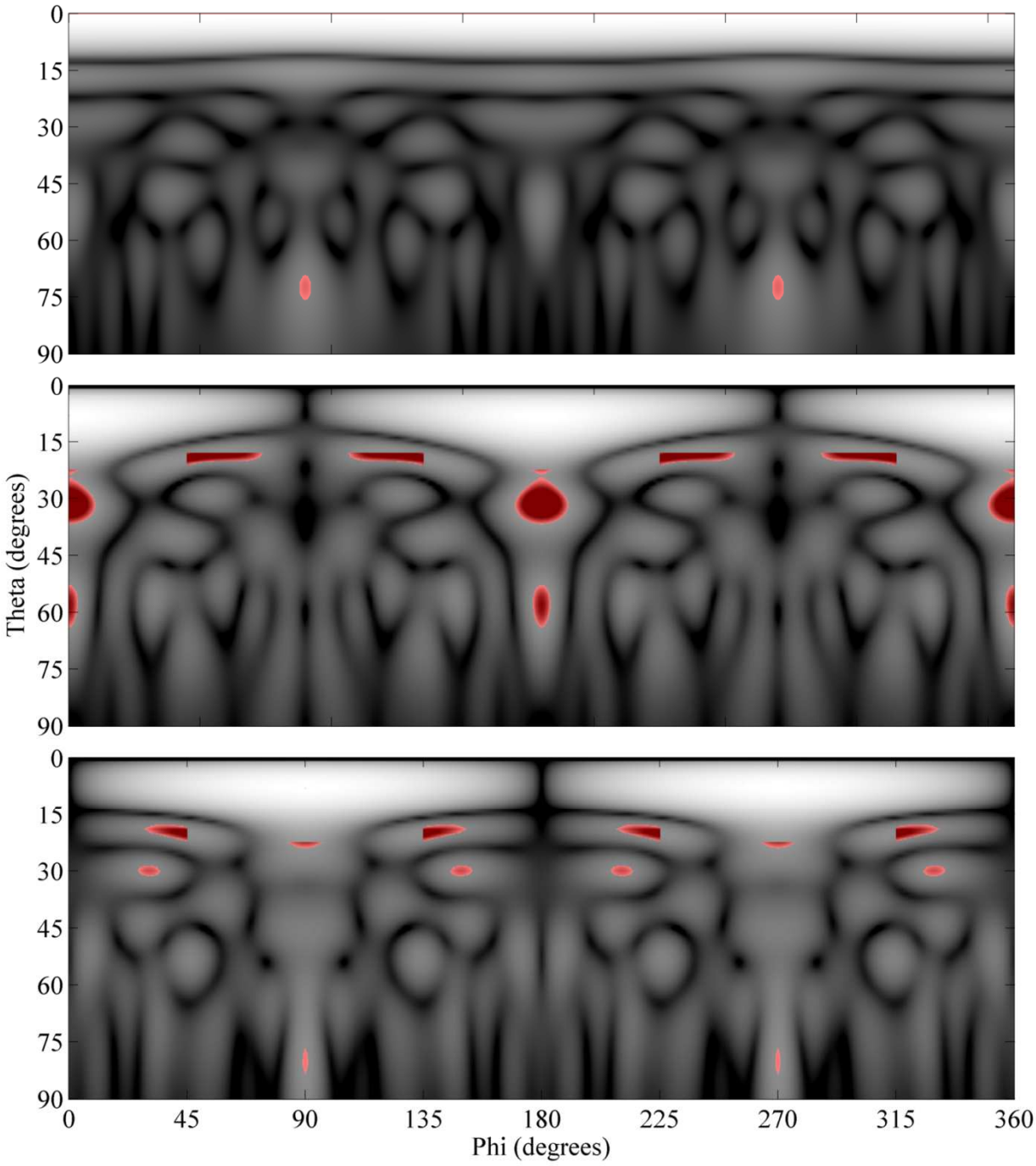

Figure 3.50. The resulting patterns for the tapered monopulse microstrip wire grid array. Red areas indicate the places where the required mask is exceeded. Top to bottom is sum, azimuth difference and elevation difference patterns.

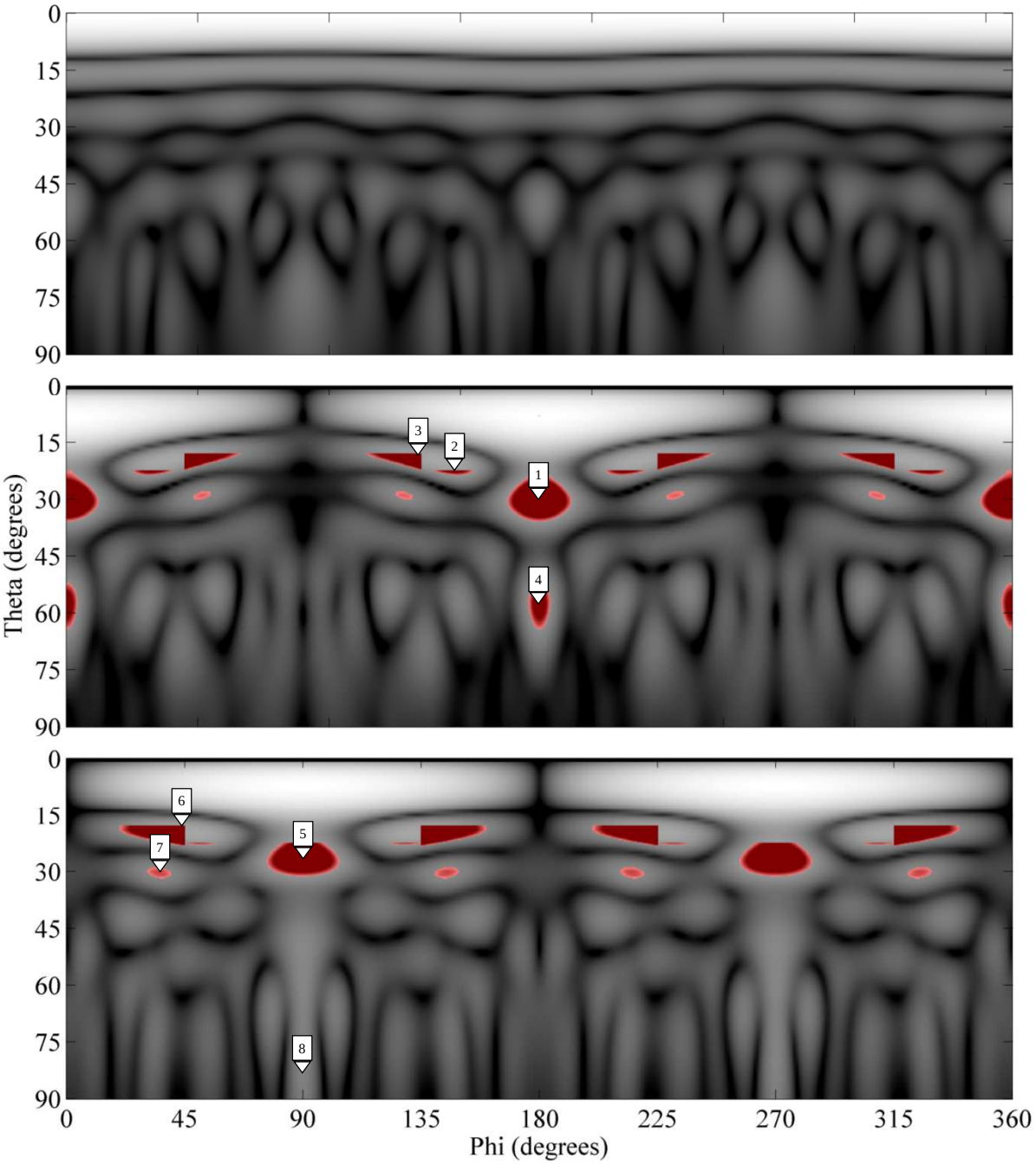

Figure 3.51. The resulting patterns for the equally excited monopulse microstrip wire grid array. Red areas indicate the places where the required mask is exceeded. Top to bottom is sum, azimuth difference and elevation difference patterns.

Table 3.16 shows a comparison between the equally excited antenna and the tapered antenna with respect to how much they exceed the required azimuth difference mask. These differences are indicated at key markers shown in in Figure 3.51.

Table 3.16. Comparisons of by how much the equally excited and tapered antennas exceed the azimuth difference mask requirement.

Nr.	Equally Excited [dB]	Tapered [dB]
1	3.9	2.1
2	1.3	<=0
3	4.8	1.9
4	1.9	0.8

Table 3.17 shows a comparison between the equally excited antenna and the tapered antenna with respect to how much they exceed the required elevation difference mask. These differences are indicated at key markers shown in in Figure 3.51.

Table 3.17. Comparisons of by how much the equally excited and tapered antennas exceed the elevation difference mask requirement.

Nr.	Equally Excited	Tapered
5	3.4	<=0
6	5.2	1
7	0.6	<=0
8	<=0	0.5

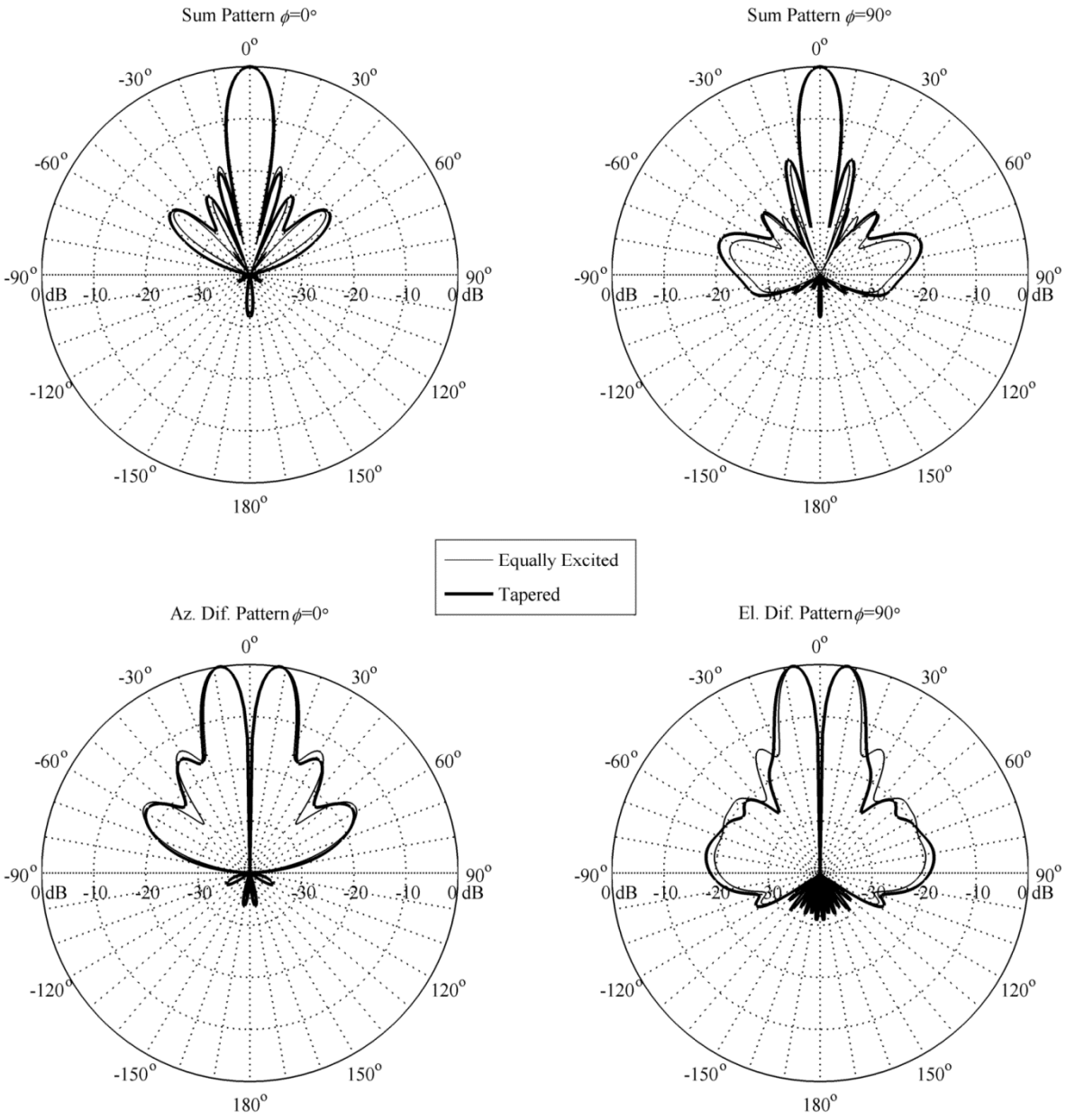

Figure 3.52. Full wave simulation showing the principal plane differences between the equally excited and tapered antennas.

Figure 3.52 shows that there is improvement between the equally exited and tapered design. The only place where the equally excited design shows better lobe levels, and where the mask is exceeded is for the elevation difference pattern at $\theta = 80°$.

3.8 COMPARATOR DESIGN

The comparator was designed in microstrip and simulated as per Figure 2.3. First, a 90° hybrid was implemented. Then a 90° microstrip line was added and simulated. Lastly, four of these hybrids plus quarter wave combinations were assembled to construct the complete comparator circuit.

3.8.1 90° hybrid coupler

A 90° hybrid coupler was designed and constructed in CST microwave studio on a Rogers 5880 substrate of thickness 0.127 mm

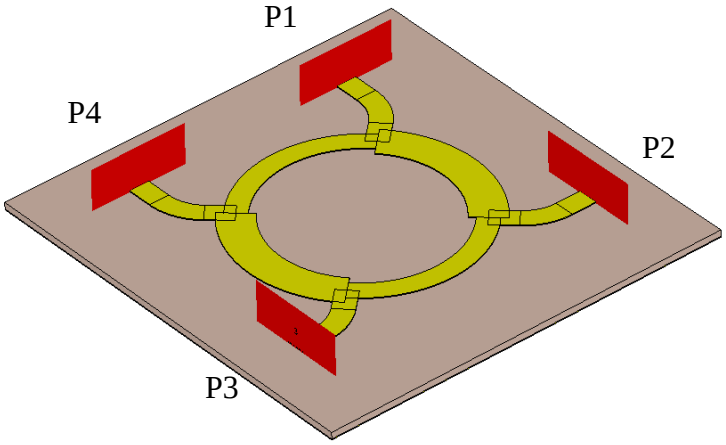

Figure 3.53. A 90° hybrid coupler constructed on Rogers 5880 with dielectric thickness of 0.127 mm.

The magnitude of the S-parameters of the Hybrid coupler is shown in Figure 3.54. From this figure it is clear that the input is well matched at 18 GHz. S_{11} is represented by the red trace, and is measured at -33 dB. The isolation between ports 1 and 4 is also excellent at 18 GHz. S_{41} is represented by the orange trace. The through and coupled ports S_{21} and S_{31} shows excellent balance with both S_{21} and S_{31} equals to -3.3 dB. Figure 3.55 shows the phase differential between S_{21} and S_{31}. The phase differential is equal to 89.98°.

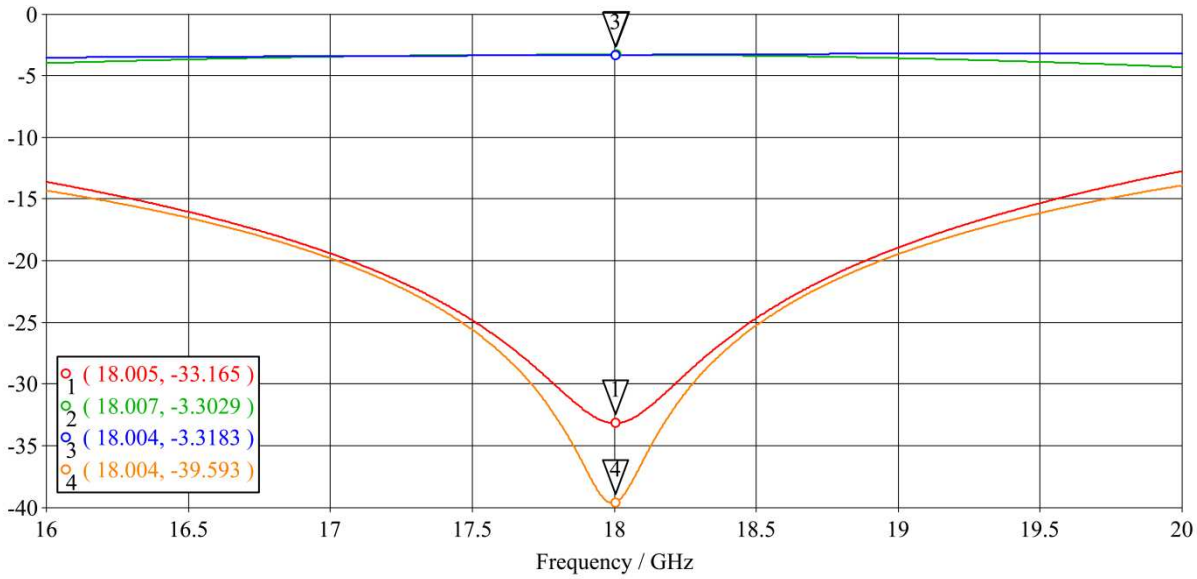

Figure 3.54. Magnitude of the S-parameters of the 90° hybrid coupler.

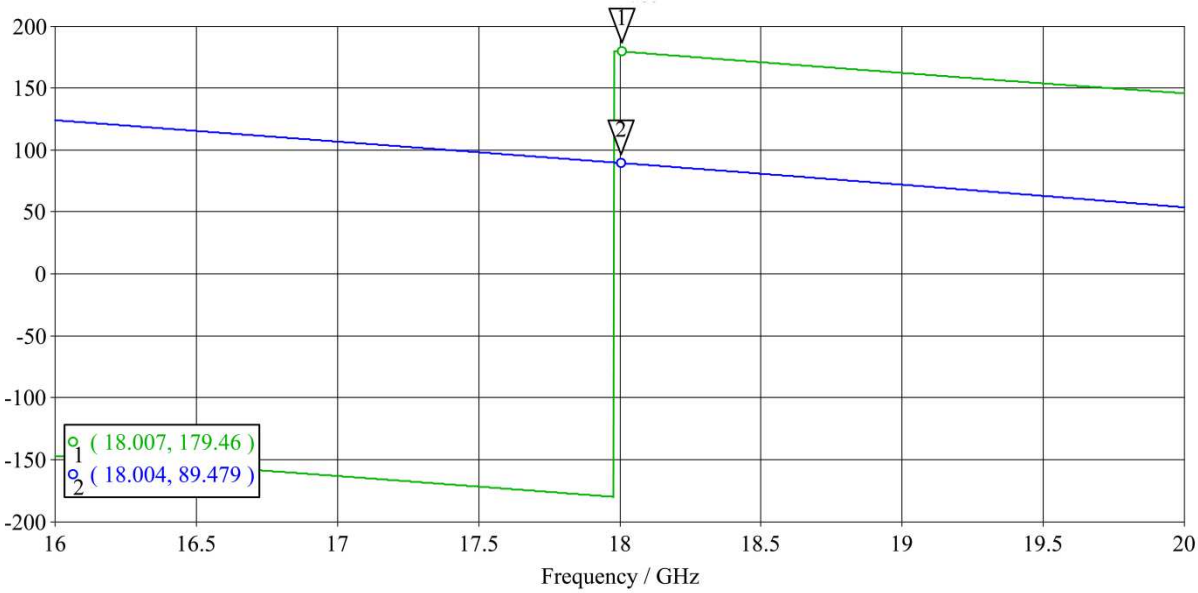

Figure 3.55. Phase of the S-parameters of the 90° hybrid coupler.

Next, a quarter wave transmission line is added to the 90° hybrid as follows.

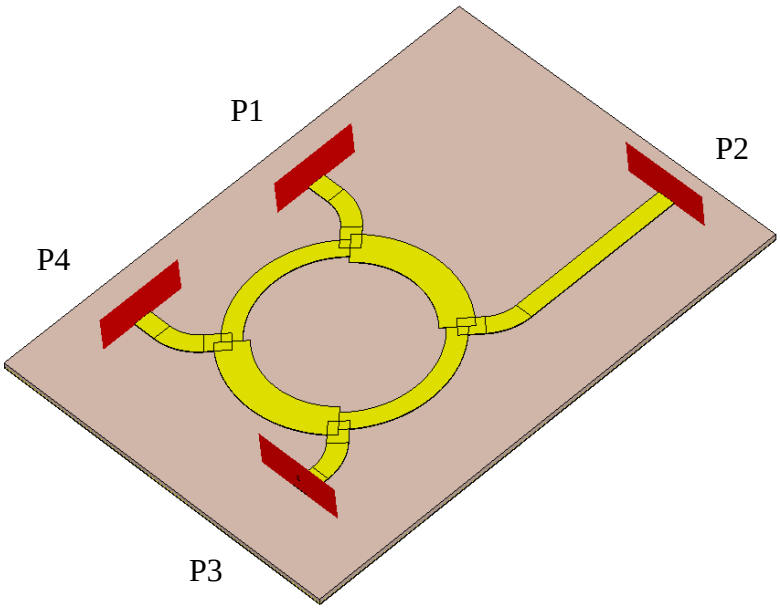

Figure 3.56. A 90° hybrid coupler plus quarter wave line constructed on Rogers 5880 with dielectric thickness of 0.127 mm.

The magnitude of the S-parameters shows some shift regarding input match and isolation, but these parameters are still perfectly acceptable. More importantly, both S_{21}, S_{31}, S_{24} and S_{34} are still equal to -3.3 dB. Also, it can be seen than the phase differential between S_{21} and S_{31} is 0°, while the phase differential between S_{24} and S_{34} is 0.4°.

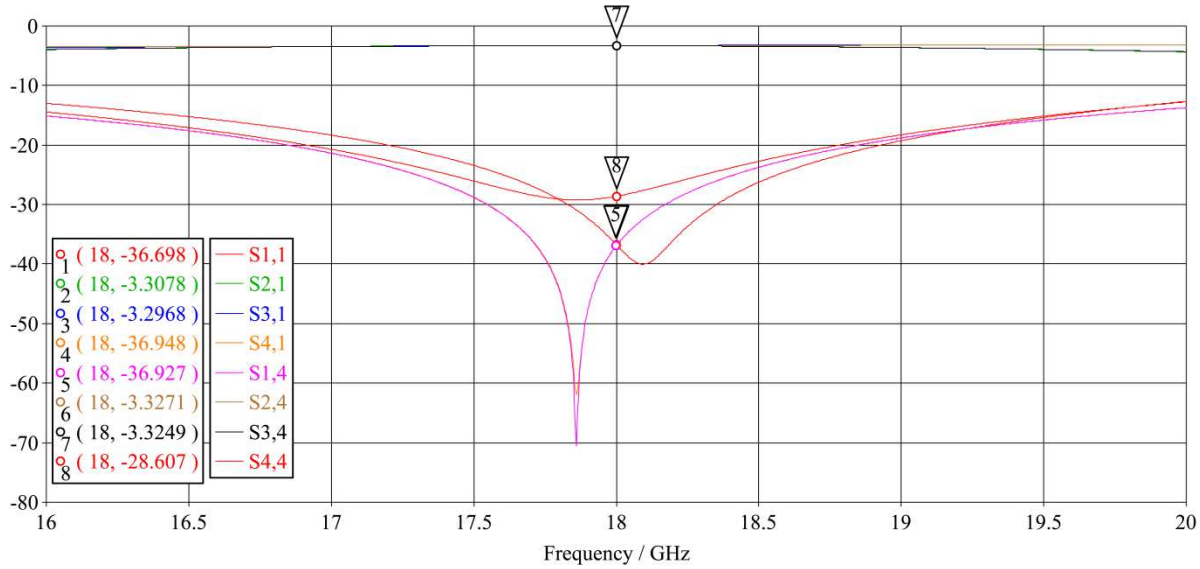

Figure 3.57. Magnitude of the S-parameters of the 90° hybrid coupler plus quarter wave section.

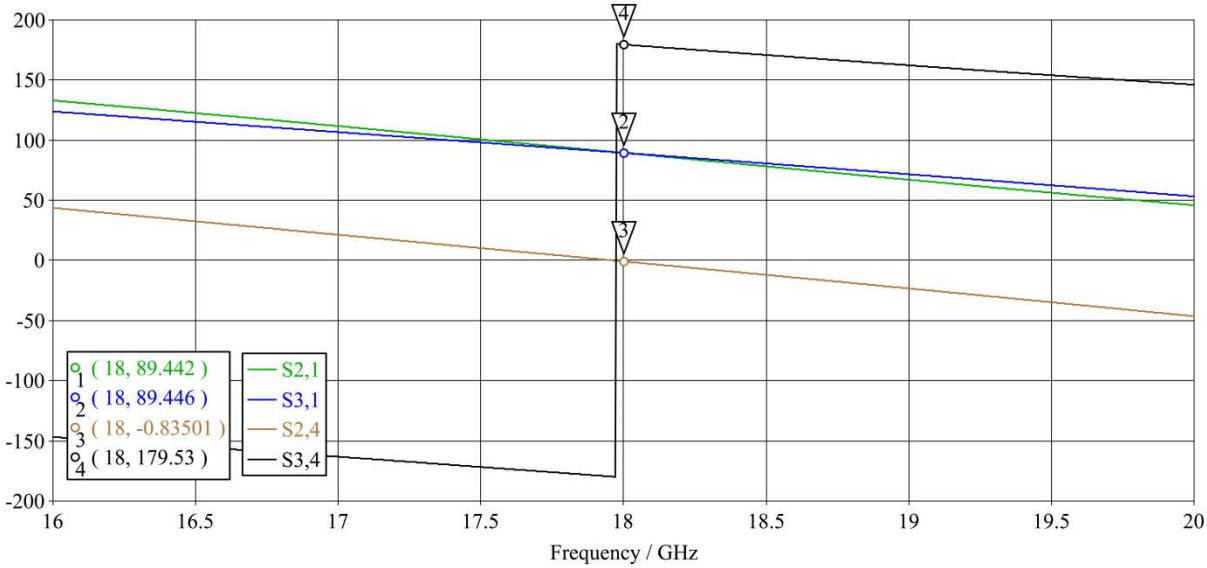

Figure 3.58. Phase of S_{21}, S_{31}, S_{24} and S_{34} for the 90° hybrid plus quarter wave section.

3.8.2 The complete monopulse comparator

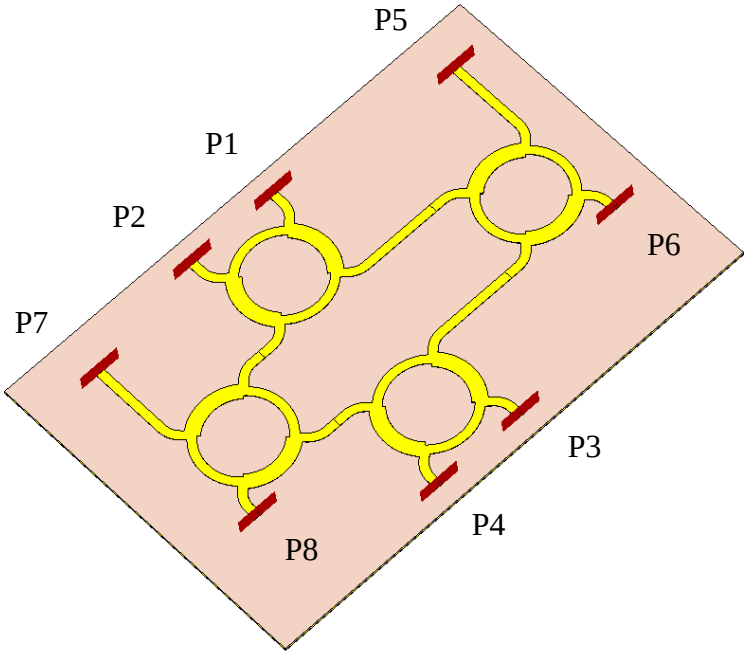

Figure 3.59. The complete monopulse comparator constructed on Rogers 5880 with dielectric thickness of 0.127mm.

From the magnitude of the S-parameters, it can be seen that the power to each port is around -6.5 dB. Therefore, the loss through the comparator is 0.5 dB. It can also be seen that the difference in the S_{x5}, S_{x6}, S_{x7} and S_{x8} parameter is less than 0.5 dB over the span 17.5 GHz to 18.5 GHz. Also, the isolation between any of the driving ports of the comparator (port1 to port4) is more than 30 dB over at least a 500 MHz bandwidth at 18 GHz. With port 1 as driving port, the expected mode of the antenna will be elevation difference. Here, the maximum phase error is 1.3° at 18 GHz. Port 2 is expected to the double difference channel and will not be used. Port 3 represents the azimuth difference channel. Here S_{53} and S_{63} show a maximum error of 1.1°, while S_{53} and S_{83} shows an error of 1.8°. Lastly for Port 3 as driving port, S_{63} and S_{73} show an error of 0.1°.

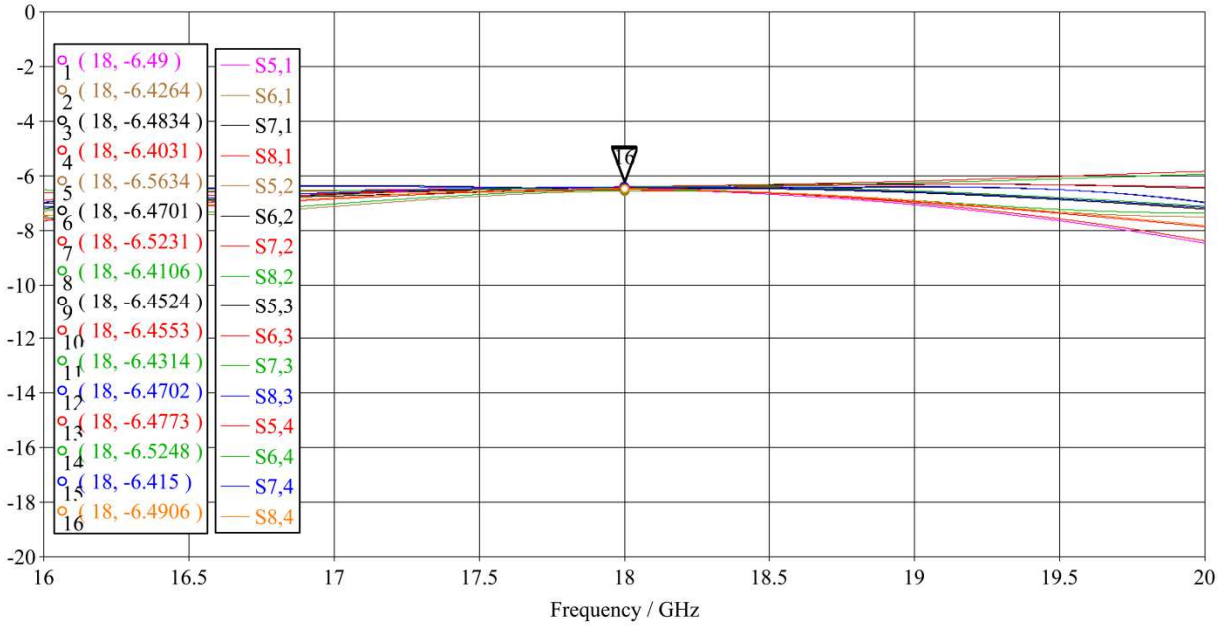

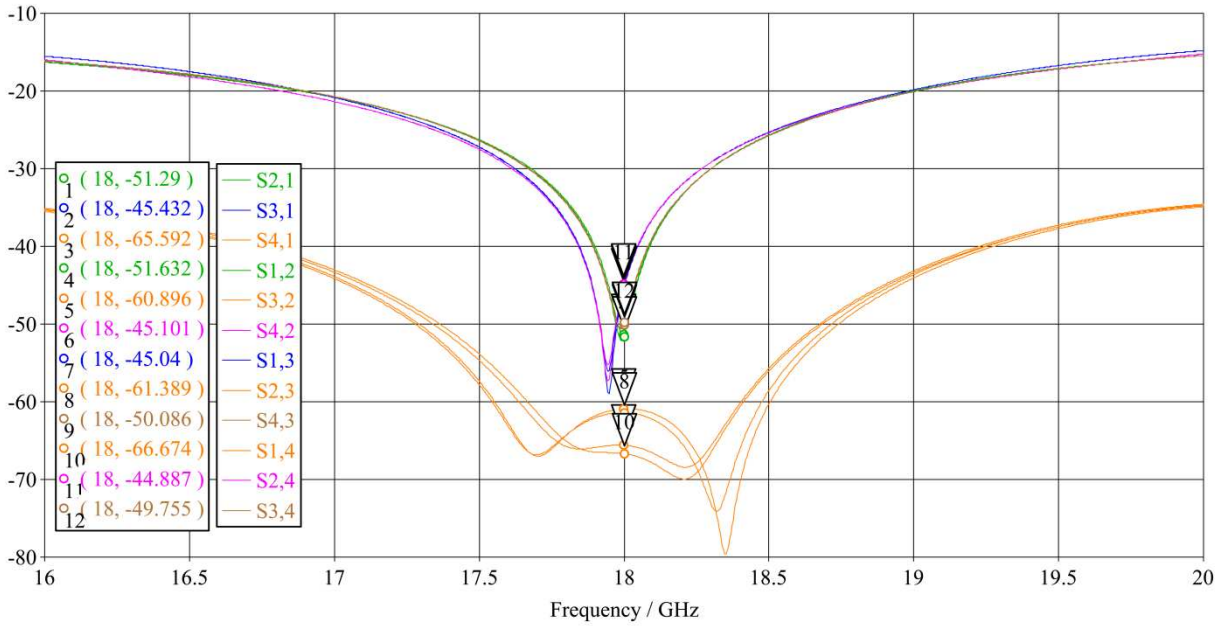

Figure 3.60. Magnitude of key S-parameters of the complete comparator.

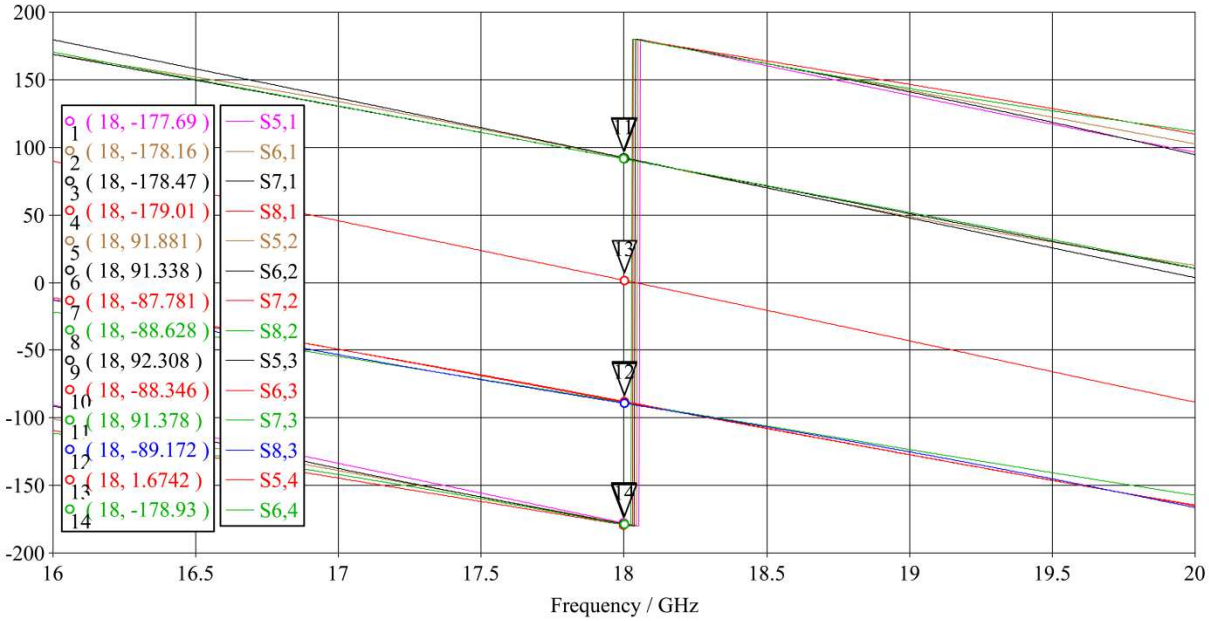

Figure 3.61. Phase of key S-parameters of the complete comparator.

The sum channel is expected to be formed when driving Port 4. The phase error between S54 and S64 is 0.6° and the phase error between S54 and S84 is 0.4°. Lastly the phase error between S64 and S74 is 0.6°. The comparator can therefore be used to drive the monopulse antenna array.

3.9 CONSTRUCTION OF THE COMPLETE MONOPULSE MICROSTRIP WIRE GRID ARRAY

The complete monopulse microstrip wire grid array is constructed on a compound substrate, with stack up as shown below. The monopulse comparator sits at the back of the antenna, and feeds the antenna at the same locations as was done during the previous simulations.

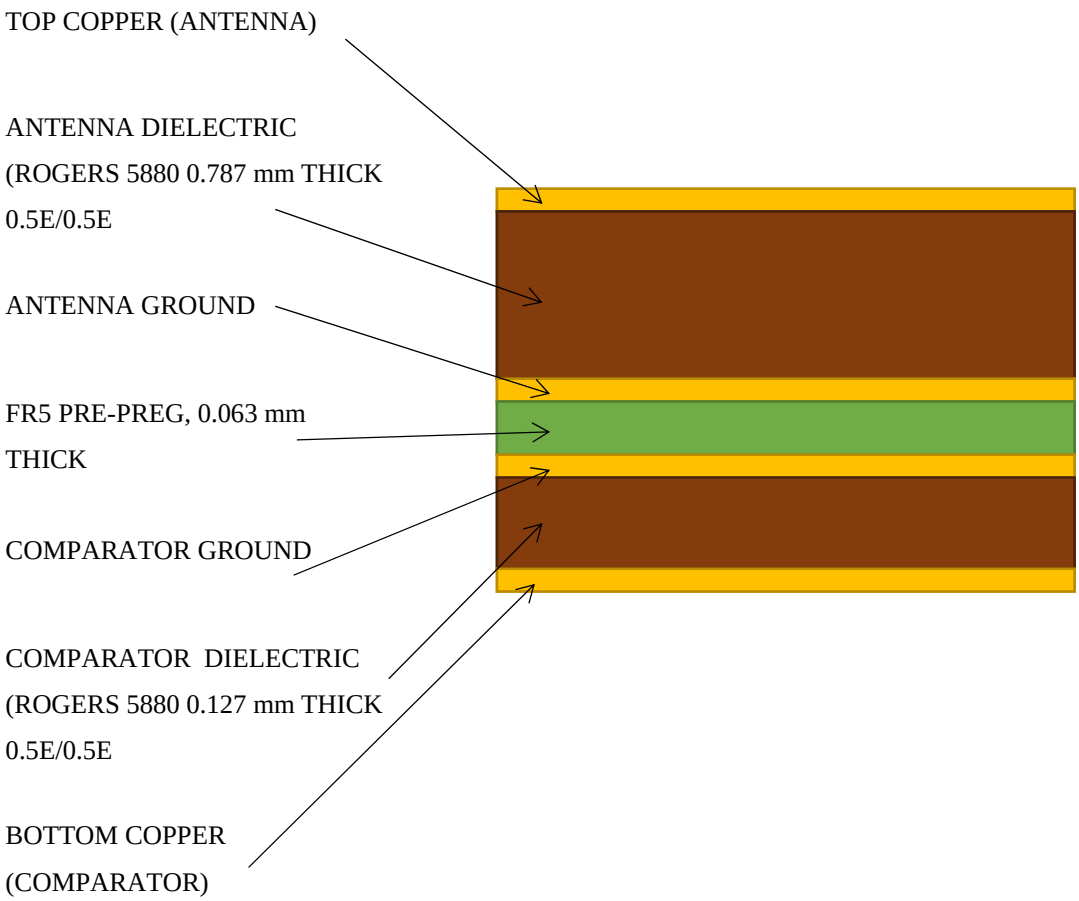

Figure 3.62. Substrate used for the complete antenna design and manufacturing.

Circuitry on the back of the antenna like the monopulse comparator is referenced to the ground plane on the bottom, while the antenna is referenced to the ground plane on the top. These ground planes need to be connected by vias, preferably at the spots where the back circuitry connects to the antenna. The first step is to check that the feed will still work properly when the coaxial probe feeds are replaced by the microstrip to coax transition as shown below. The microstrip running at the back of the substrate, and referenced to the ground plane forming part of the bottom dielectric is connected to the probe, which runs through the substrate and is connected to the microstrip wire grid array. Around the clearance is arranged 5 vias which drills through to the ground plane on the antenna substrate. The ground planes are therefore connected at these points. The coaxial clearing was adjusted to yield optimal results

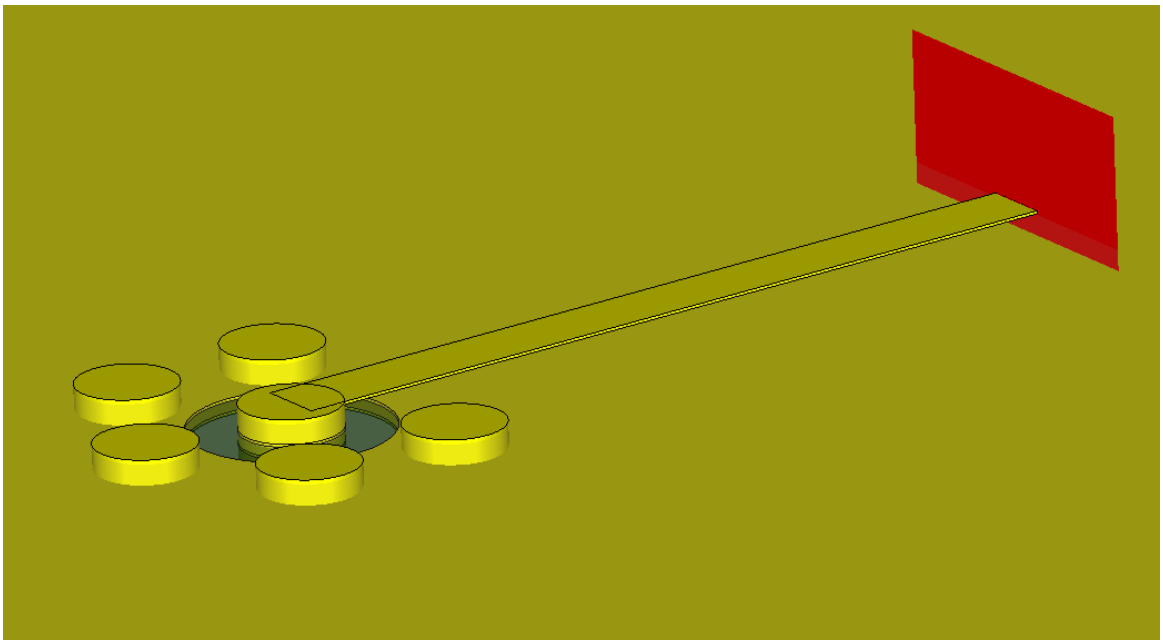

Figure 3.63. Microstrip to probe transition.

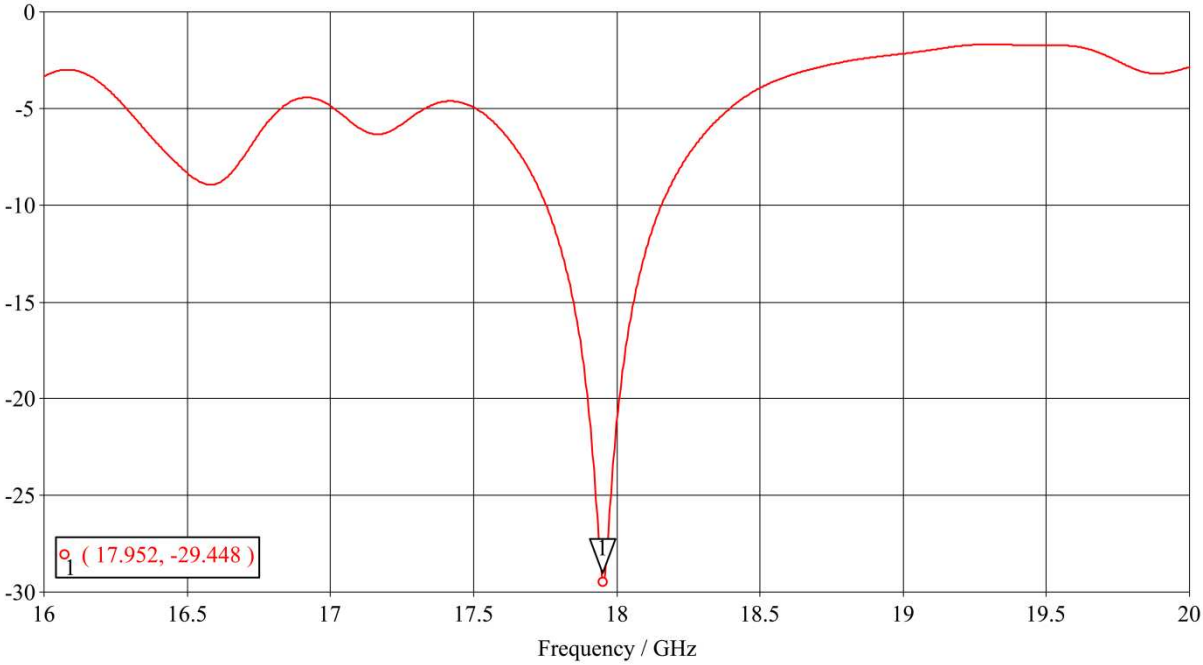

Figure 3.64. Input match to the antenna with the microstrip-probe transition.

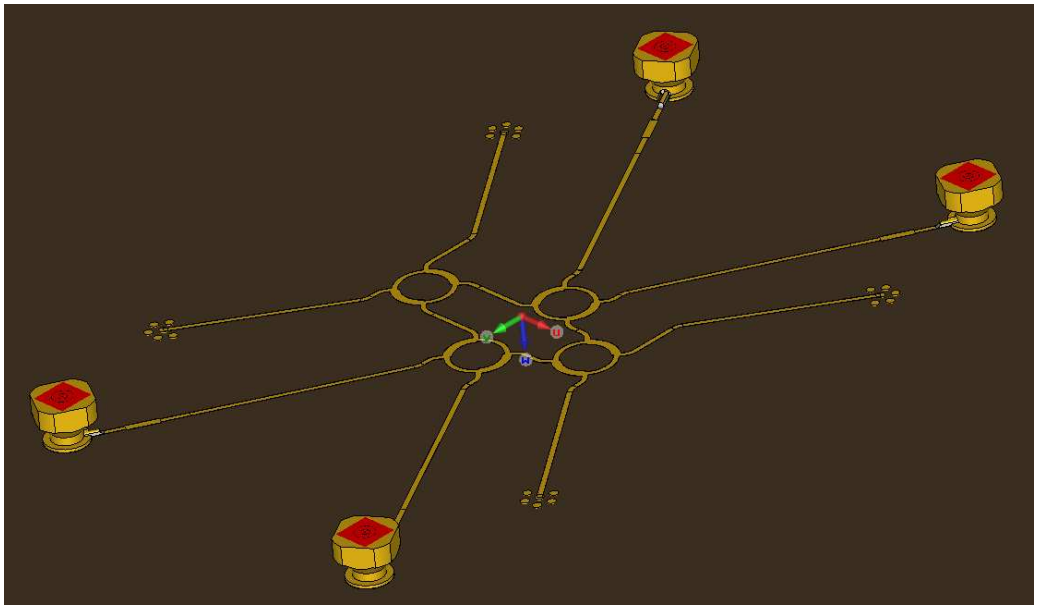

Figure 3.65. Comparator constructed on the back of the antenna.

The comparator was constructed on the back of the antenna. The comparator is driven with four Corning Gilbert GPPO connectors. Because the return loss of these connectors starts to degrade from 20 GHz and higher, a quart wave section was implemented at each connector to improve the return loss. The figure below shows the antenna side where the feeds connect to the antenna.

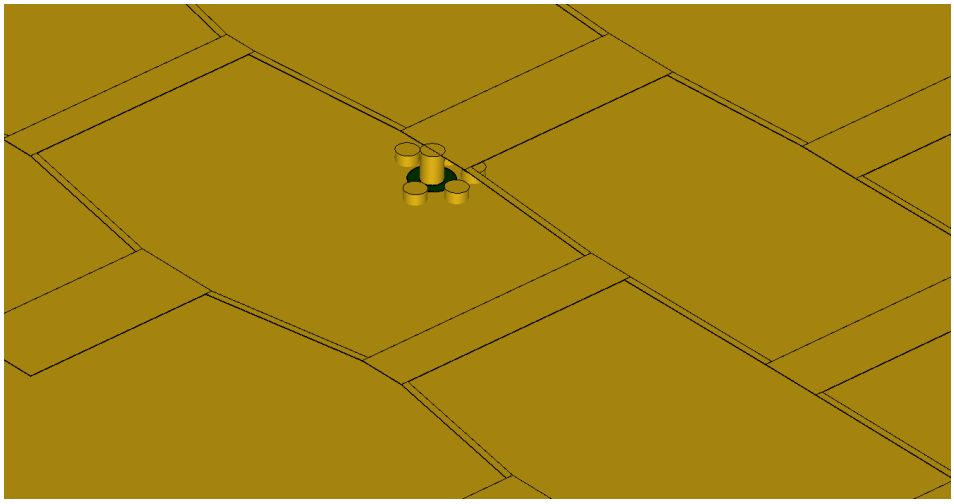

Figure 3.66. Area where the probe feed connects to the antenna.

3.10 CHAPTER CONCLUSION

This chapter has outlined a design process for a monopulse microstrip wire grid antenna. The chapter starts off with a derivation of the directivity for a monopulse antenna in general. Next, a wire grid monopulse antenna of equal excitation was designed, following the methodology proposed by Palmer [3]. Some expansion of the methodology was done, by observing that dipole lengths for two port dipoles could be found by looking at the magnitude of the s-parameters. The magnitude clearly shows where the dipole is resonant. Doing this eliminates the ambiguity of finding a single phase parameter with multiple variables that can be tuned to find this parameter. A comparison between the analytical model and a full wave simulation already shows some discrepancies in the expected side lobe level. This could be due to mutual coupling, feed radiation and surface waves. These phenomena are amongst the factors limiting the synthesis of exact side lobe levels. A sequential quadratic programme, based on the work of McNamara [7], and expanded to a monopulse antenna with azimuth and elevation difference patterns, as well as arbitrary element arrangement was developed. The results were checked with a simple genetic algorithm with the same constraint levels. The results of this optimization were applied to the design of a tapered monopulse microstrip wire grid antenna. Even though the resulting tapered antenna did exceed the mask requirement at a couple of key coordinates, the resulting tapering did lower these key side lobe levels by an average of 2 dB over the equally excited antenna.

CHAPTER 4 SIMULATED AND MEASURED RESULTS

4.1 INTRODUCTION

This chapter outlines the results for the final tapered monopulse microstrip wire grid antenna including the comparator network. The first results discussed are the full wave electromagnetic simulation results. After this, the actual measured results are given.

4.2 3D EM SIMULATION RESULTS OF THE COMPLETE MONOPULSE WIRE GRID ANTENNA

4.2.1 Input match

The input match for all three modes of operation (sum, azimuth difference and elevation difference) is shown below. The 10 dB bandwidth is 450 MHz, or around 2.5%.

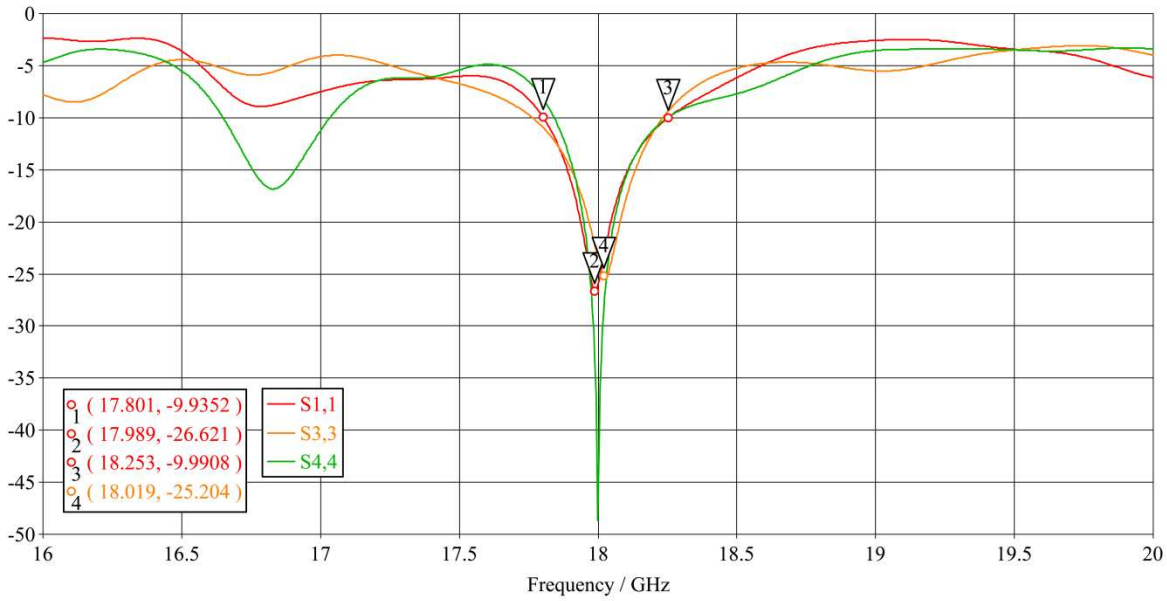

Figure 4.1. Input match for all three modes of operation.

4.2.2 Side lobe levels

The results of the complete monopulse wire grid antenna is shown in Figure 4.3 and Figure 4.3. Adding the comparator network shows some degradation in side lobe levels over the simulations where the quadrants were fed in perfect anti-phase with four different ports. For the sum pattern, the side lobes are degraded at (θ, ϕ) = (90°, 15°), where the mask is exceeded by 0.8 dB. The other point remains the same as the four quadrant simulation at (θ, ϕ) = (90°, 73°) where the mask is exceeded by 0.3 dB. The azimuth pattern shows the worst results, where the mask is exceeded at (θ, ϕ) = (0°, 32°) and (θ, ϕ) = (0°, 58°), by 2.9 dB and 2.1 dB respectively in the azimuth plane. The elevation difference pattern matches the mask in the elevation plane, but exceeds the mask by 2.2 dB and 1.9 dB at (θ, ϕ) = (20°, 45°) and (θ, ϕ) = (30°, 30°) respectively. It is clear however, that the tapered design does yield better side lobe levels than the equally excited antenna, which is included in the principle plane pattern plots of Figure 4.3.

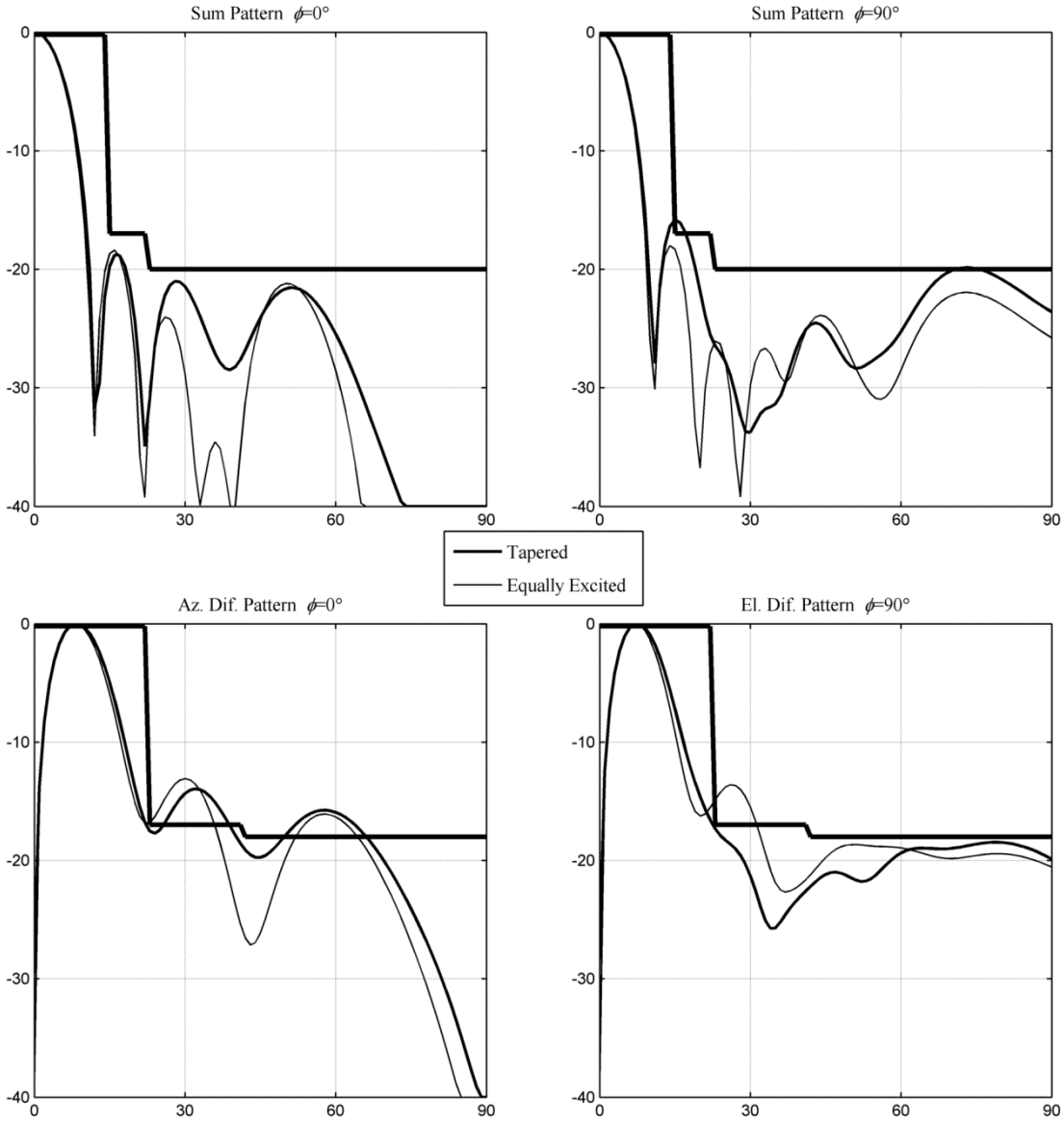

Figure 4.2. Principal plane radiation patterns showing where the mask is exceeded. The thick black lines represent the mask constraints in the principal planes.

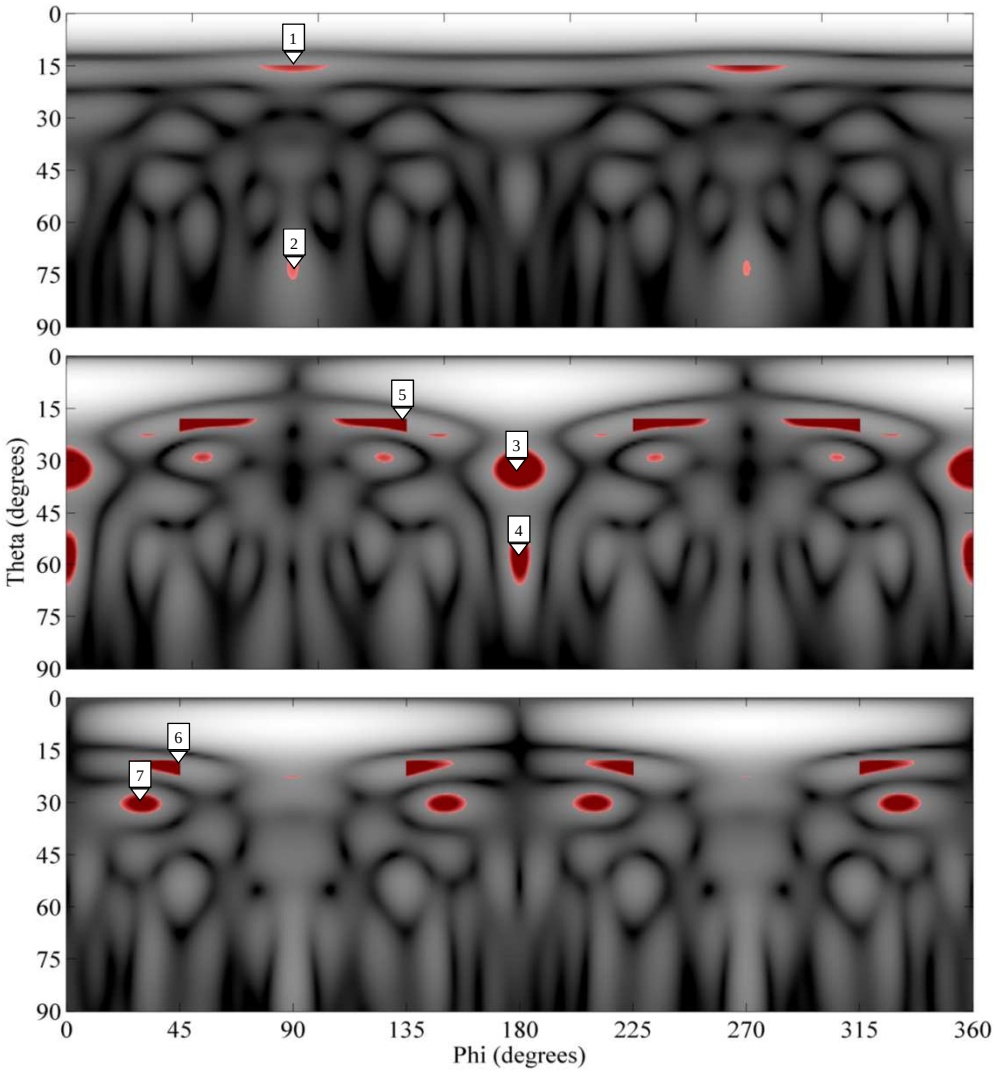

Figure 4.3. Resulting normalized radiation patterns for the final tapered monopulse wire grid array. Areas in red are where the mask is exceeded. From top to bottom is sum, azimuth difference and elevation difference patterns.

The places where the difference patterns significantly exceed the masks are shown in the table below, and the markers are indicated on the figures above. As can be seen, even though the masks are exceeded, the side lobe levels are generally still better than what could be achieved for the equally excited case.

Table 4.1. Comparison between how much the equally excited and tapered antenna exceeds the mask requirements.

Nr.	Equally Excited Array [dB]	Complete microstrip monopulse wire grid array with tapered excitation [dB]
1	<=0	0.8
2	<=0	0.3
3	3.8	2.9
4	1.9	2.1
5	4.8	3.1
6	5.2	2.2
7	0.6	1.9

4.2.3 General comments on the resultant pattern

From the table above it is clear that the mask requirements could not be met by the realized antenna. Further degradation is observed from the 4 independent quadrant simulation results of Chapter 3. Even so, it should be noted that generally, at the key indicated places where the mask requirement are exceeded, it is generally equal or better than an equally excited antenna. On the sum pattern, it is clear that the mask is exceeded by less than 1 dB. The only place where the tapered solution delivers worse side lobe levels than the equally excited antenna is at marker 8. The results in Chapter 3 and Chapter 4 show that even though it is possible to lower side lobe levels when tapering the dipole currents by varying their widths, the microstrip wire grid array poses some significant challenges when trying to synthesize specific side lobe levels. This is especially true when trying to synthesize side lobe levels on all three patterns for a monopulse microstrip wire grid array.

4.2.4 Monopulse null

Another important metric for monopulse antennas is the null depth and direction. The null depth is mainly determined by how well the monopulse comparator balances the amplitudes to the 4 quadrants. The phasing will have an influence on the null direction. As can be seen from the difference patterns shown in Figure 4.4 and Figure 4.5 below, the difference nulls for both azimuth and elevation patterns are around -30 dB, while the null position is around 0.1°

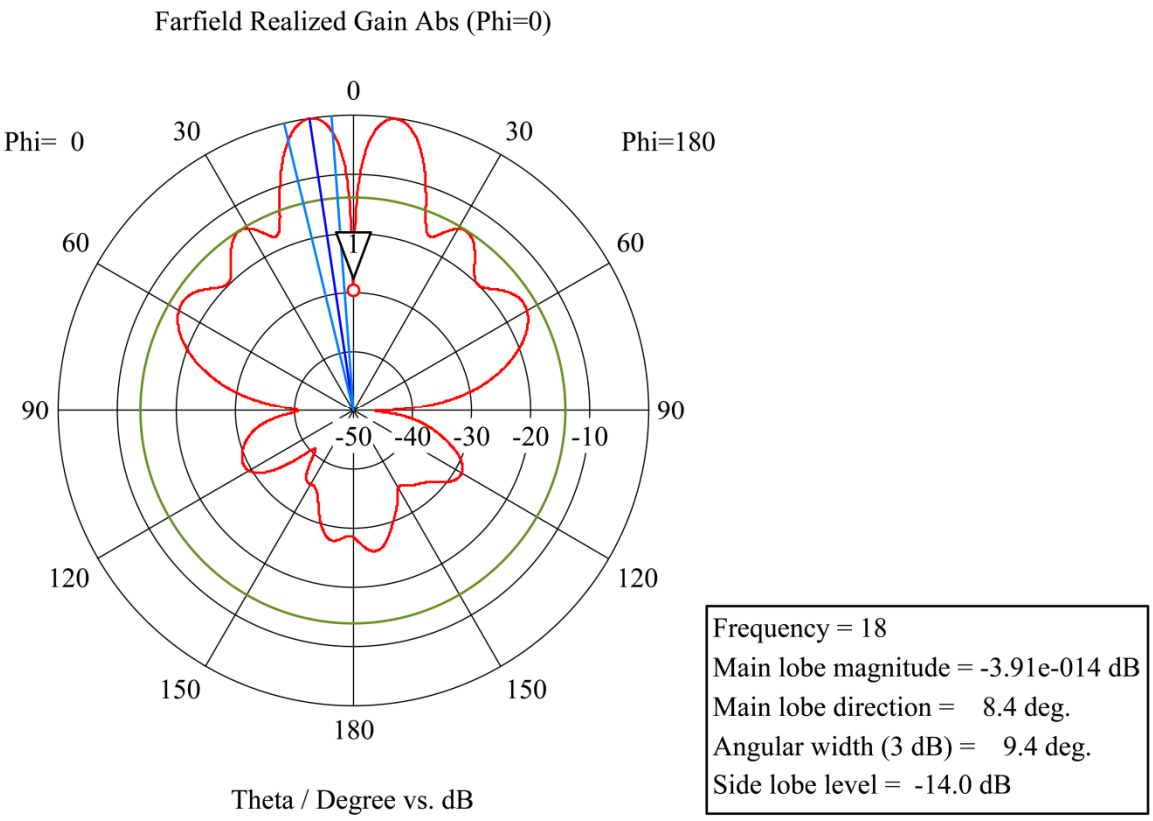

Figure 4.4. Difference null for the azimuth difference pattern.

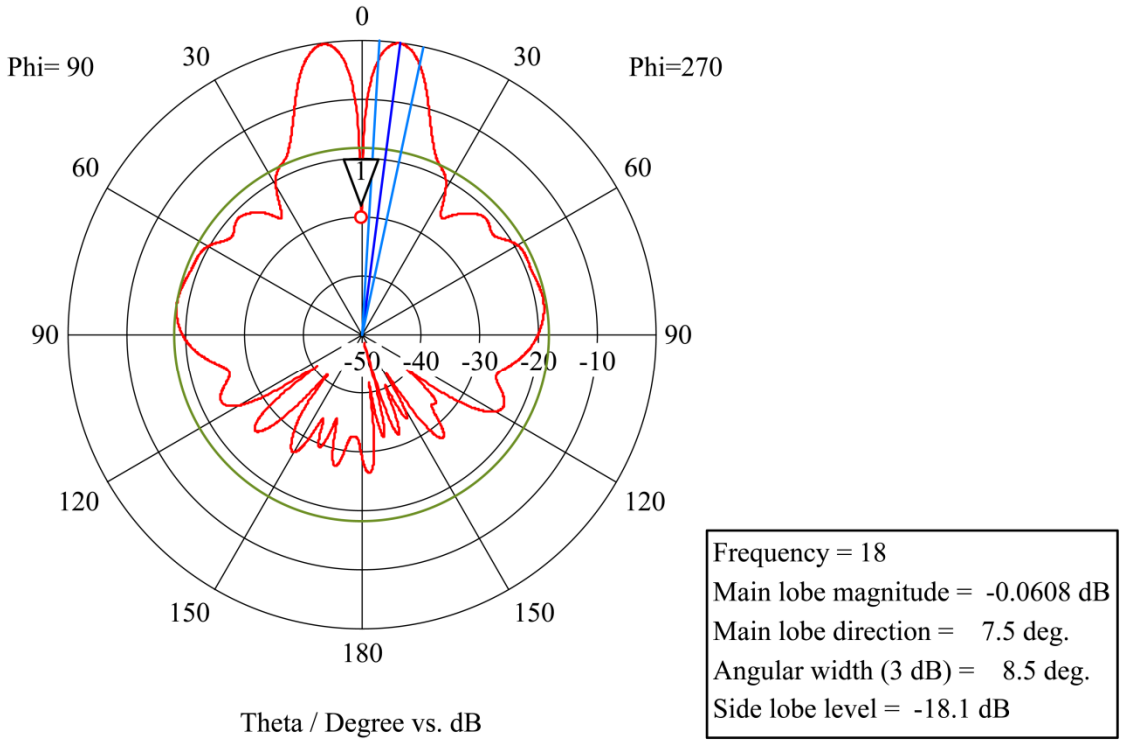

Figure 4.5. Difference null for the elevation difference pattern.

4.3 MEASURED RESULTS OF THE MANUFACTURED MONOPULSE MICROSTRIP WIRE GRID ARRAY

The antenna was manufactured using the layer stack-up as shown in Figure 3.62. The resulting antenna is shown in Figure 4.6.

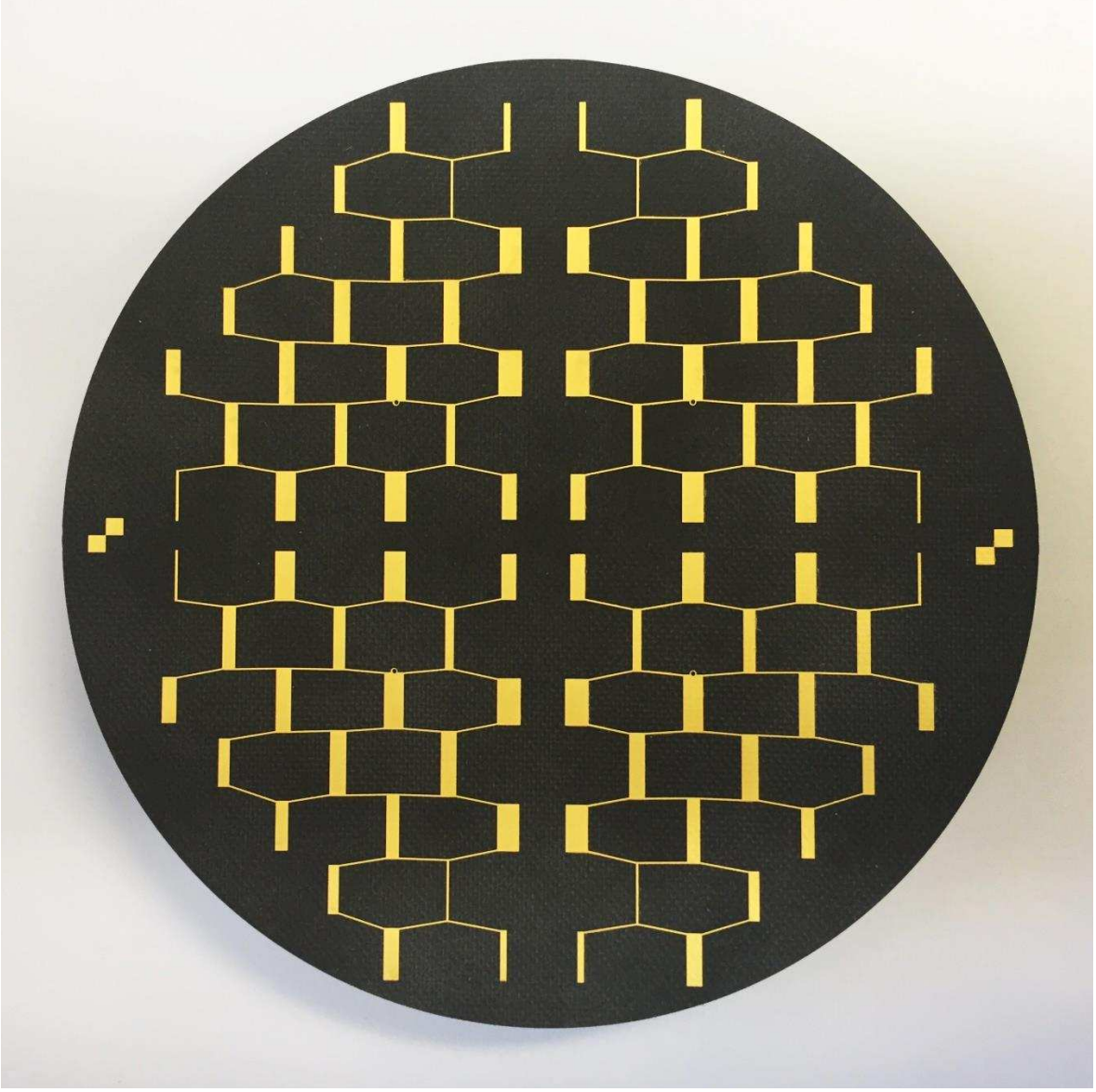

Figure 4.6. The front side of the manufactured monopulse microstrip wire grid antenna.

4.3.1 S-parameters

The S-parameters for the sum, azimuth and elevation channels are shown in Figure 4.7 to Figure 4.11 below. It is clear that the measured S-parameters are different from the simulated S-parameters shown in Figure 4.1. The main reason here is that the GPPO connectors used could not be characterized accurately. When moving the connectors, there was huge response difference detected. The curves below are the curves that resulted most of the times when the connectors were adjusted. In future, it is highly recommended to use screw-in connectors. The sum channel -10 dB input match bandwidth is measured at 1.41 GHz, while the -15 dB match bandwidth is 780 MHz. The sum channel input match bandwidth is usually more important than the azimuth and elevation channels input match bandwidths, because the radar transmitter is located at this channel. The isolations between the sum and two difference channels are better than 20 dB over the span 17 GHz to 18.7 GHz. These isolations are shown in Figure 4.10 and Figure 4.11. Isolation results show good correlation between measurements and simulation, indicating that the connectors are the main contributor to differences in reflection coefficient measurements.

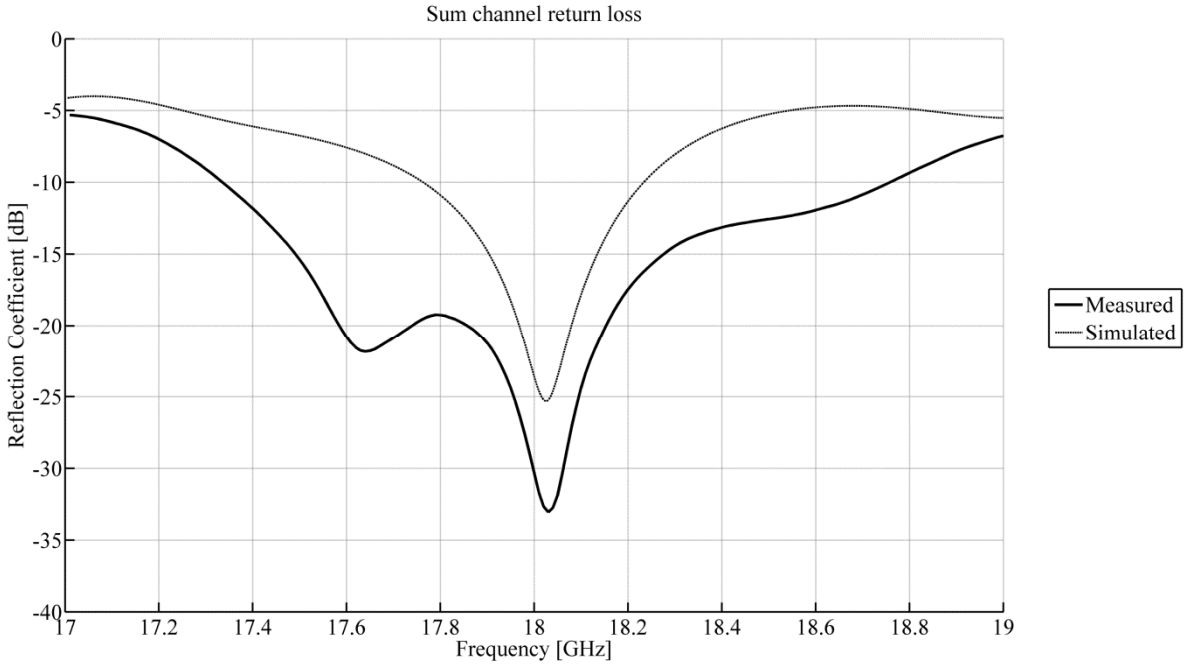

Figure 4.7. Measured sum channel reflection coefficient.

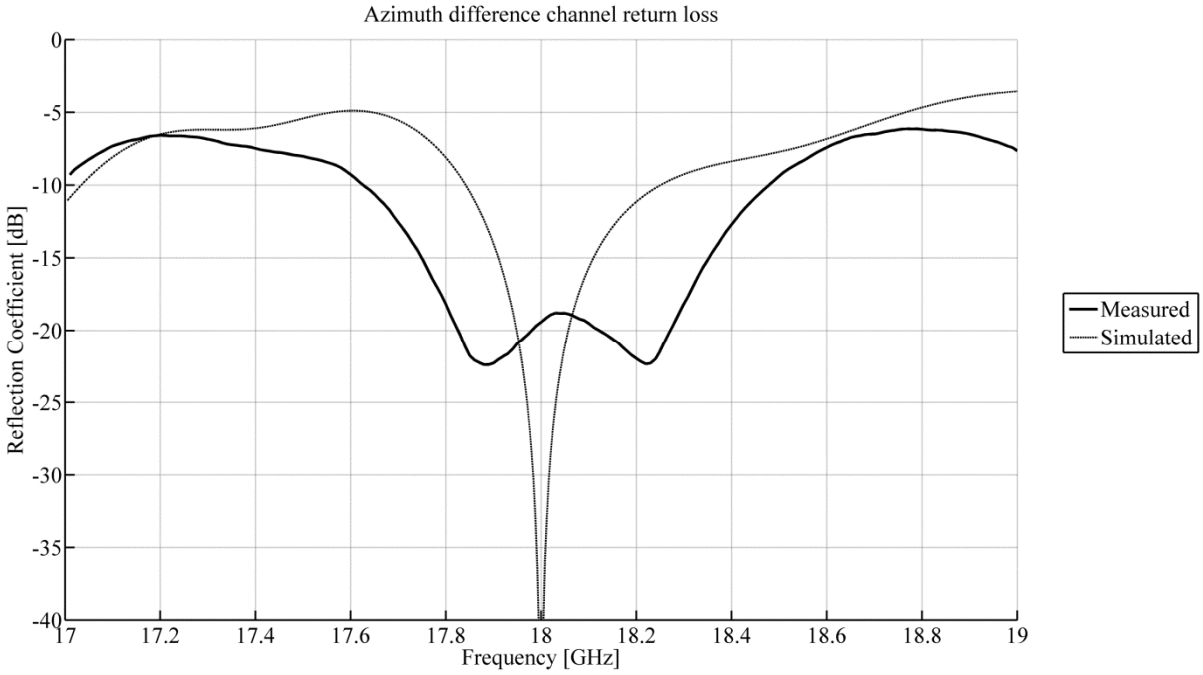

Figure 4.8. Measured azimuth difference channel reflection coefficient.

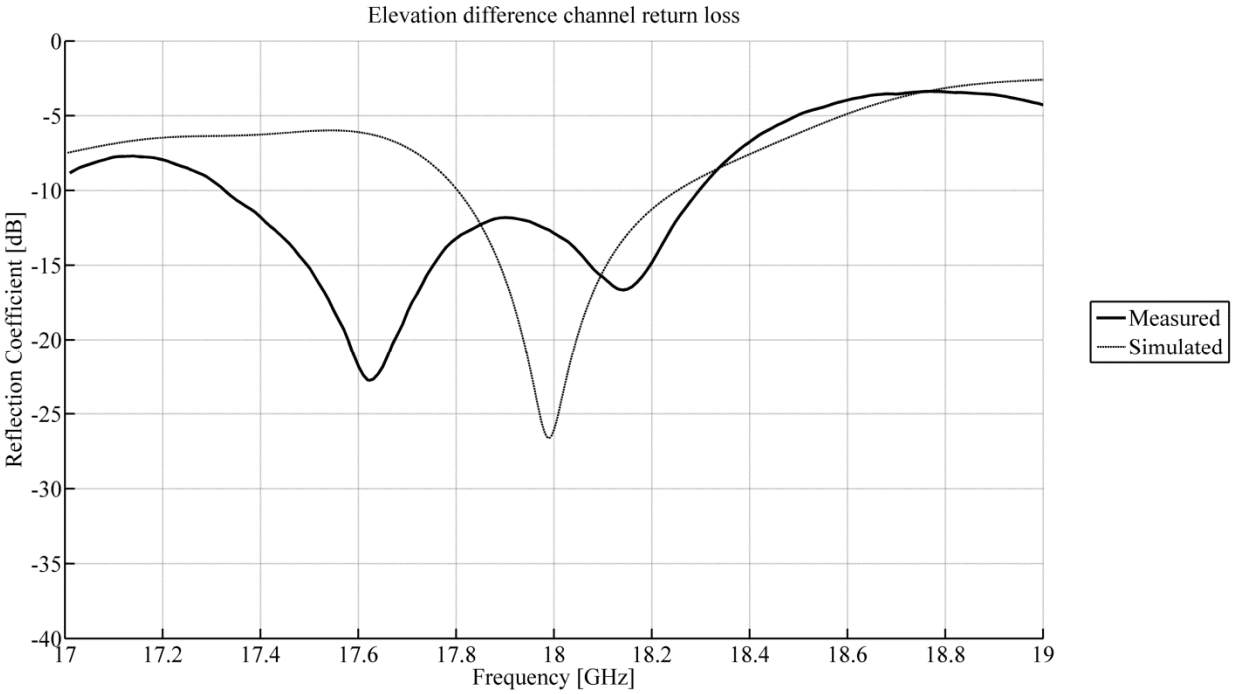

Figure 4.9. Measured elevation difference channel reflection coefficient.

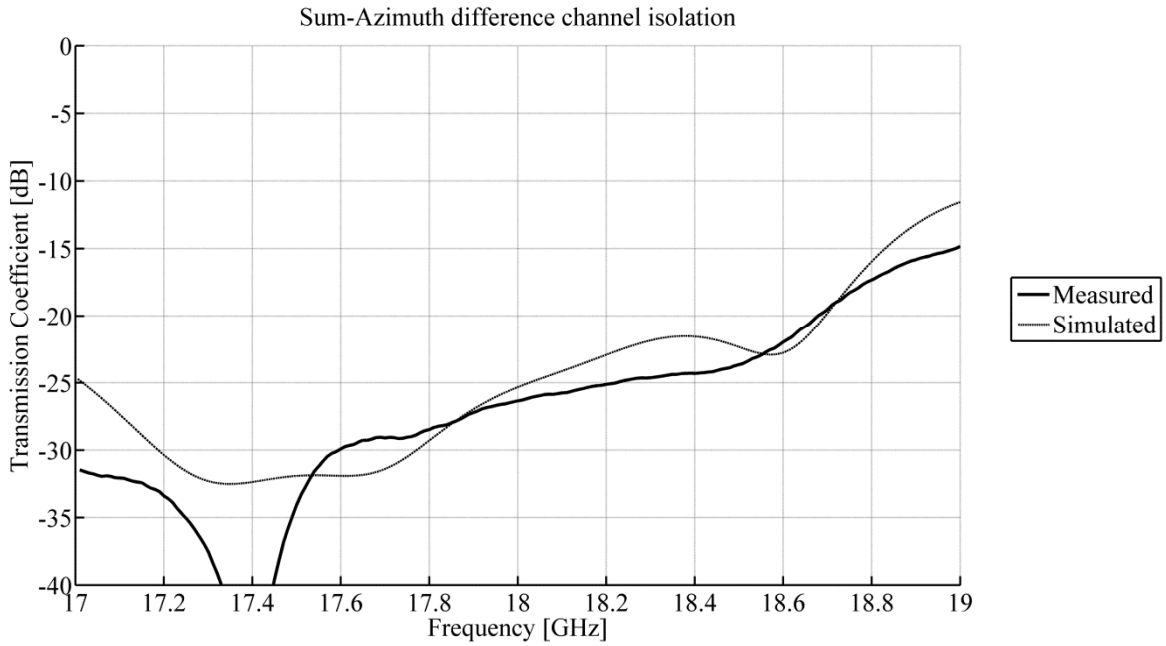

Figure 4.10. Measured isolation between the sum and azimuth difference channels.

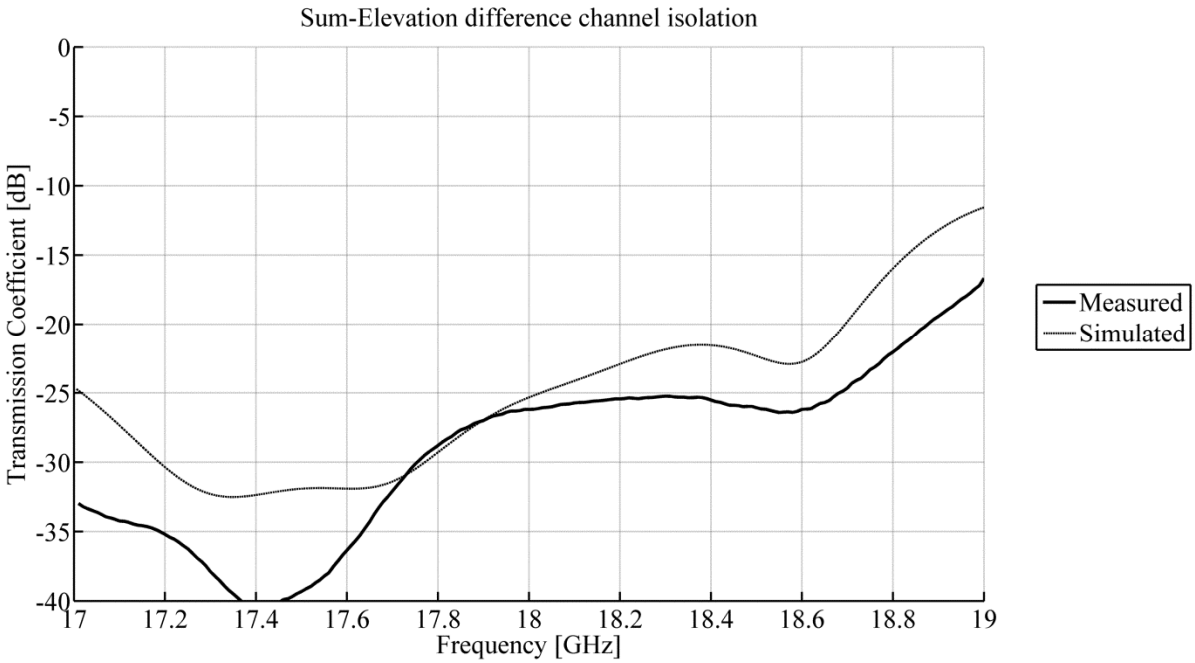

Figure 4.11. Measured isolation between the sum and elevation difference channels.

4.3.2 Radiation patterns

Time constraints did not allow the full 3D measurement of the radiation patterns. Instead, the radiation patterns were measured in the principal planes only. The radiation patterns were measured at the compact range at the University of Pretoria. Figure 4.12 to Figure 4.15 show the radiation patterns in the azimuth and elevation planes of the antenna. As can be seen the measured results generally agree well with the simulated results. The sum pattern in the azimuth plane is the only pattern where a measured side lobe at θ=18° exceeds the simulated side lobe by 1.7 dB.

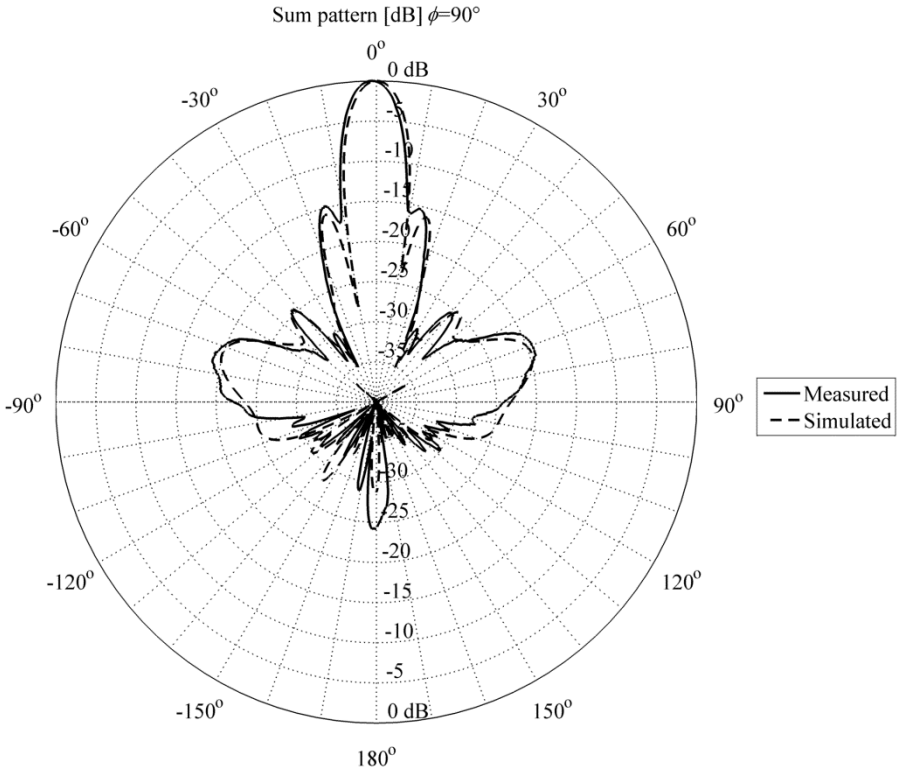

Figure 4.12. Sum pattern in the elevation plane.

The null depth for the elevation difference pattern is better than 30 dB, and the direction is better than 1° off boresight. Although the direction was very difficult to measure accurately, since the antenna itself is not very stiff and generally warped to some extent.

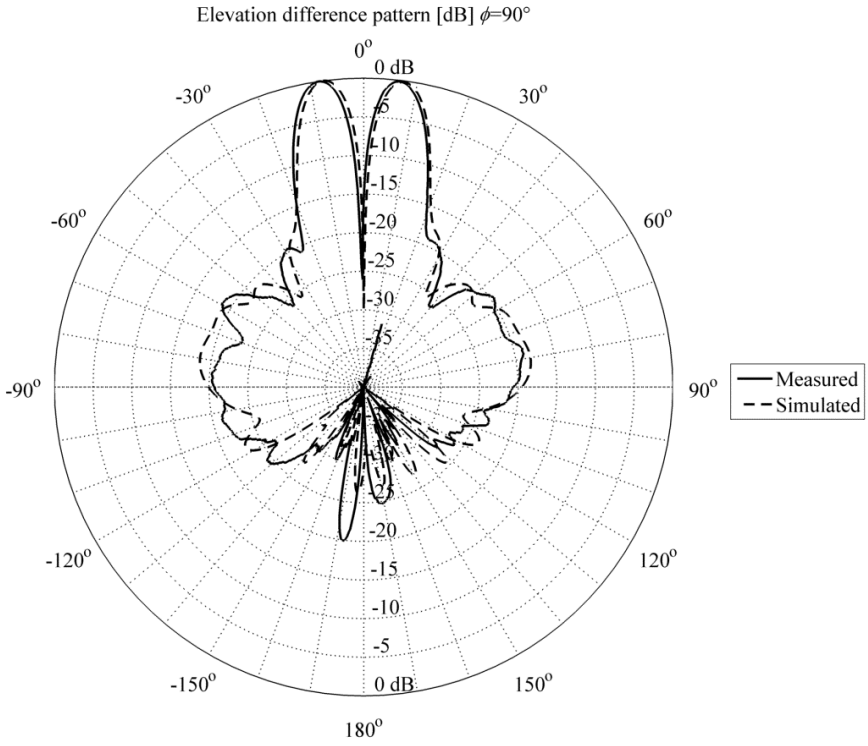

Figure 4.13. Elevation difference pattern.

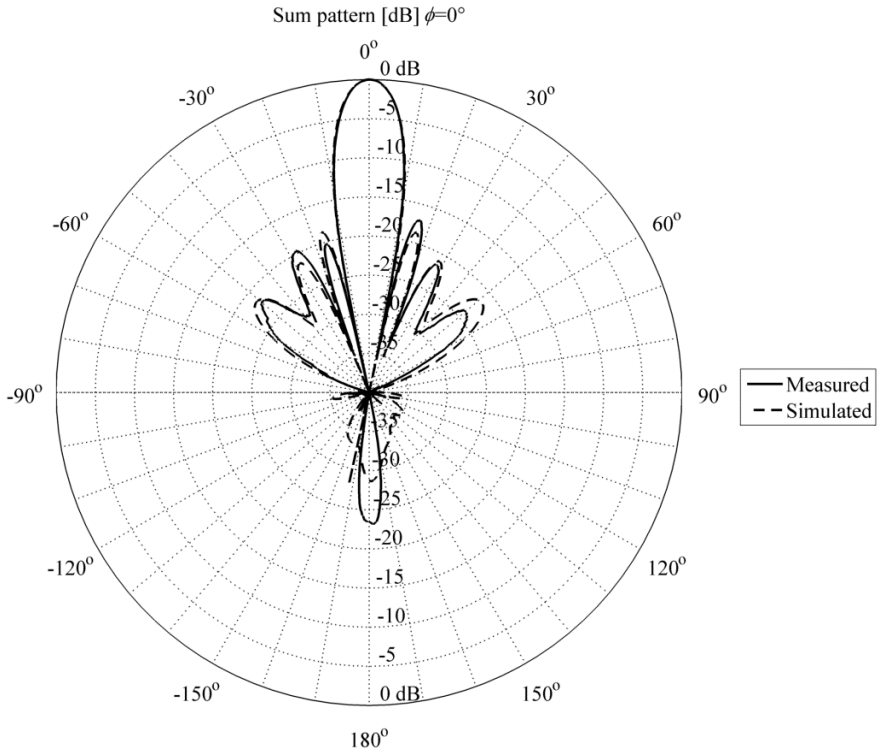

Figure 4.14. Sum pattern in the azimuth plane.

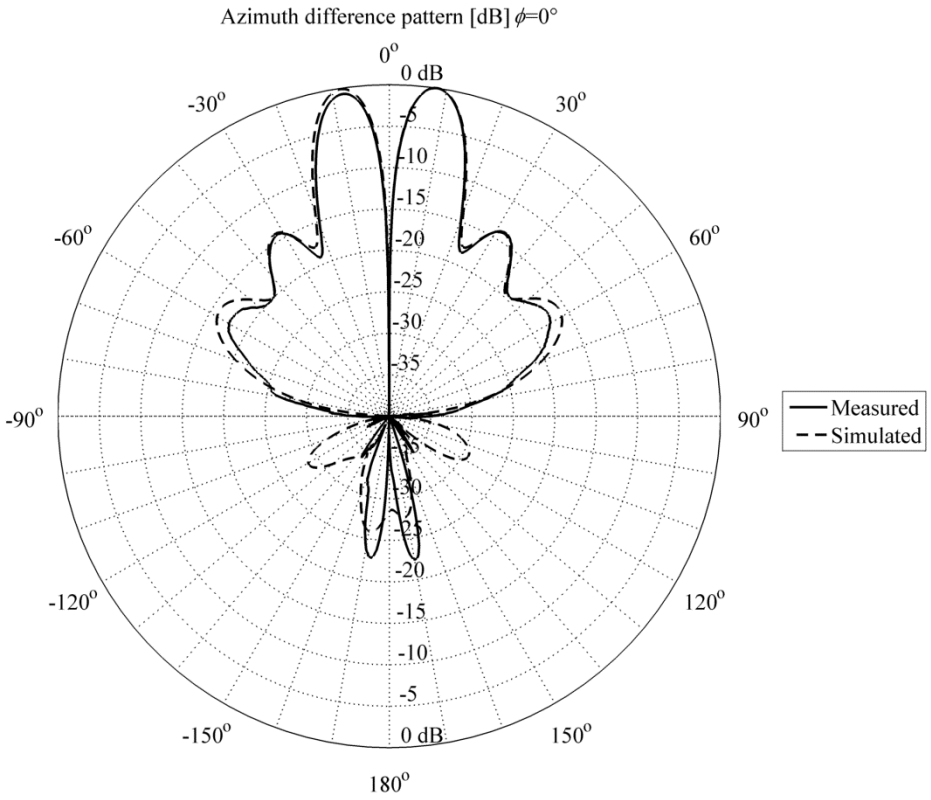

Figure 4.15. Azimuth difference pattern.

The null depth for the azimuth difference pattern is better than 40 dB, and its direction is also less than 1° off boresight. To better measure the null directions for the difference patterns in future, a better jig needs to be designed to secure the antenna in a very flat position. The measured sum channel gain vs. frequency is shown in Figure 4.16. The measured gain is roughly 2 dB lower than the simulated gain. This can be attributed to the cable used for the measurement. Since the antenna utilizes GPPO connectors, the SMA to GPPO cable was not included in the calibration. The cable employed was a Huber-Suhner Minibend cable with SMA-SMA interfaces of 250 mm length. The cable has a specified loss of 4 dB/m at 18 GHz. This cable has been retrospectively measured to have a loss of 1 dB using a vector network analyser. What could not be measured was the loss of the SMA-GPPO adapter and GPPO-GPPO snap-in interface to the antenna circuit board. Therefore, the difference between measured gain and simulated gain is less than 1 dB.

The 3dB gain bandwidth extends from 17.7 GHz to 18.9 GHz. Combining this with the impedance bandwidth makes the antenna useable from 17.7 GHz to 18.3 GHz.

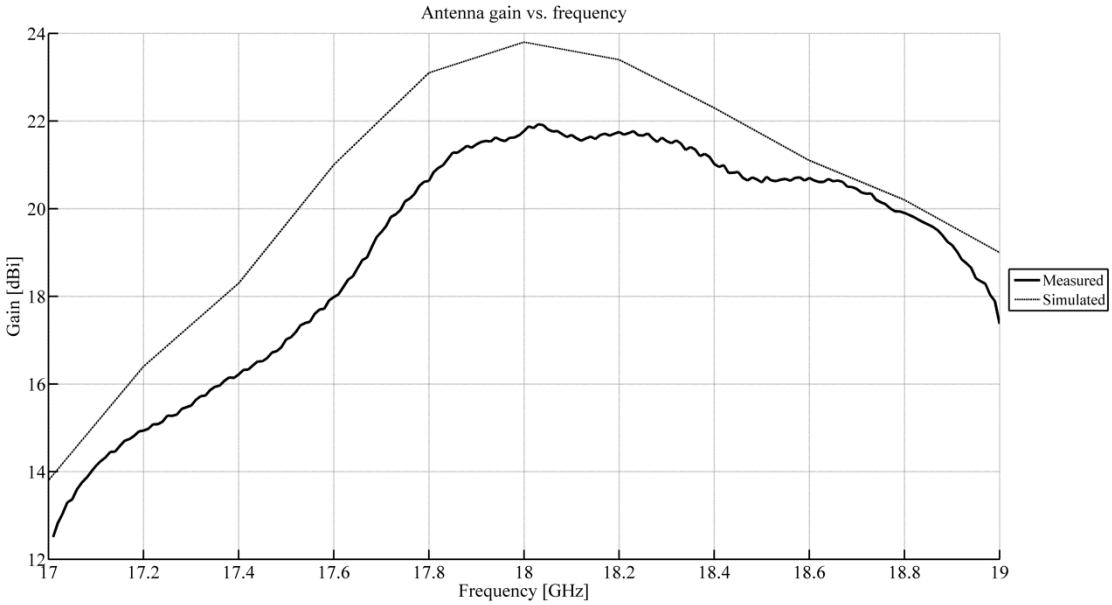

Figure 4.16. Measured sum-channel gain vs. frequency.

4.4 CHAPTER CONCLUSION

This chapter outlined the results of the final monopulse microstrip wire grid antenna. It shows that it is quite a challenge to synthesize exact side lobe levels in all three patterns simultaneously and realise the design using the microstrip wire grid array. The GPPO connectors presented difficulties especially with the measurement of the S-parameters. The manufactured antenna exhibited very good impedance bandwidth of 780 MHz for -15 dB input match. The gain bandwidth is also very respectable at 1.2 GHz and the combined bandwidth of 600 MHz is 3.33%. It is highly recommended to use screw-in connectors in future to eliminate changes in S-parameters when the feed connectors and cables are moved. There is generally good agreement between the measured and simulated radiation patterns in the principal planes. Although an equally excited antenna was not physically manufactured, the full wave results shows that the tapered antenna did achieve better side lobe levels than the equally excited antenna.

CHAPTER 5 CONCLUSION

The design of a monopulse wire grid antenna with simultaneous synthesized sum, azimuth and elevation difference patterns is presented. Firstly, an analytical model was developed to calculate the radiation pattern of a monopulse antenna of arbitrary arrangement. Next, the design procedure based on the work done by Palmer [3] was used to design an equally excited monopulse array. The work by Palmer was expanded somewhat by noting that the dipole lengths for two-port modules can easily be found by looking at the magnitude of the s-parameters first. Examining the magnitude of S21 for the two-port modules reveals the resonance frequency of the dipole. Therefore the dipole lengths can be set first, before the feed arm lengths are adjusted for optimal module phasing. This procedure eliminates ambiguity when optimizing a single phase parameter if two variables (dipole length and feed arm length) are available for tuning. The design was implemented in CST Studio Suite which is a commercial finite difference time domain solver. The 3D full wave simulation was then compared to the analytical model. During this step it became clear that effects such as mutual coupling, feed point radiation and surface waves contribute to the degradation of side lobe levels, which would make the synthesis of exact side lobe levels for all three radiation patterns of the monopulse antenna difficult. Large differences were noted, especially where low side lobes in the order of -22 dB and lower were predicted by the analytical model. The method as proposed by McNamara [7] to find simultaneously optimally low side lobes for the sum and difference patterns of an equally spaced linear array was adapted for monopulse antennas of arbitrary arrangement, and having azimuth and elevation difference patterns. This code was then used to find mask constraints for the sum and two difference patterns. In order for this to work, the integral equations needed to evaluate the directivity are kept numerical. In a few special cases, exact solutions to these integrals may be found, but generally, no close form expressions for these integrals exist. A simple genetic algorithm was developed to check the validity of the sequential quadratic programme. The cost function of the genetic algorithm was optimized somewhat to allow many differences to the mask constraint, but the differences should be small. This was done by modifying the cost function in such a way that a single large difference to the

mask is penalised more severely than a large amount of small differences. This is easily achieved by raising the cost function to some exponent. Although not much effort was spent on optimizing the genetic algorithm cost function, adequate performance was achieved, and after 50 runs of the genetic algorithm having 250 generations, the results of the genetic algorithm came extremely close to those obtained by the sequential quadratic programme. This gave great confidence that the sequential quadratic programme does indeed yield lowest possible simultaneous side lobes. The calculated excitation taper was then implemented in the design of a monopulse microstrip wire grid antenna. The dipole widths were changed in accordance with the excitation taper as proposed by Palmer [3], where the dipole widths are almost directly proportional to the excitation weight. During this design, the phases of the vertical currents at the centre of each dipole were all distributed within 15° from an average of 167°, except for the feed dipole which was off by around 23° from the average dipole current phase. The main reason for the poor phase performance is the asymmetric probe feed employed. This feed makes it impossible to satisfy all the port phasing relationships required for the feed module. Since the phasing relationships at the feed cannot be satisfied, this creates problems throughout the wire grid array. Palmer [3] also noted that the feed model is the most important module, and will have serious ramifications for the rest of the array if problems arise at this module. Since the currents are not all exactly in phase, it is expected to degrade the side lobe levels in addition to effects such as mutual coupling. Nevertheless, the tapered antenna did improve the simultaneous side lobe level in all three radiation patterns by an average of 2 dB over the equally excited antenna at key coordinates. A comparator network was designed to feed the four quadrants of the monopulse antenna. The comparator network has four channels, where each channel generates phasing relationships between the antenna quadrants that will result in sum, elevation difference, azimuth difference and double difference patterns. The double difference pattern channel was not used and simply terminated.

Full wave simulations have shown that feeding any of the input ports of the comparator, resulted in an average power to each antenna quadrant of -6.5 dB lower than the input power at the port. The power spread between the antenna quadrants is less than 0.16 dB

between all feed ports, while the phase error between the quadrants is generally less than 1.8° for all feed ports. Isolation between channels is more than 30 dB over a 500 MHZ span around 18 GHz.

The antenna was manufactured according to the design and measured. The connectors used was Corning GPPO snap-in connectors, and these connectors made measurements of the S-parameters difficult, as small movement of the feed cables and connectors resulted in large variations in the observed S-parameters. Nevertheless, it was possible to determine the S-parameters after making lots of cable movements and observing the resulting S-parameters on the vector network analyser. As a result of the connectors, and not being able to include the connector effects effectively in the 3D full wave simulation, the S-parameters did not agree very well with the simulated results, although it was clear that the antenna is resonant at 18 GHz. The measured radiation patterns in the main antenna axes agreed very well with the simulated results, but the overall gain was down by about 2 dB. The feed cable having the SMA-GPPO interface could not be included in the gain calibration of the anechoic chamber. The feed cable have an expected loss of around 1 dB at 18 GHz, while the SMA-GPPO interface, and the GPPO-GPPO snap in connection have a further unknown loss. Therefore differences between simulated and measured gain is less than 1 dB.

The main contributions of this work can therefore be summarized as follows:

1.) Expansion of the design method proposed by Palmer [3] by removing ambiguities in the design process for all two-port modules. Furthermore, this design process is outlined in detail using a tapered excitation design.
2.) The sequential quadratic programme using simultaneous constraints proposed by McNamara [7] has been expanded to allow for the design of 2D monopulse antennas of arbitrary arrangement, and having azimuth and elevation difference patterns.
3.) This work found that it is not trivial to design the microstrip monopulse wire grid array for exact side lobe level requirements. It is important to control the phase of the vertical currents, which is very difficult due to the asymmetrical nature of the

feed module. This together with mutual coupling between dipoles causes degradation in the radiation pattern response.

REFERENCES

[1] J.D. Kraus, “A backward angle end fire antenna,” *IEEE Trans. Antennas Propagat.*, vol. AP-12, pp.48-50, Jan. 1964.

[2] M. Tiuri, S. Tallqvist, and S. Urpo, “Chain Antennas”, *IEEE Antennas and Propagation Symposium Digest.,* Atlanta, Georgia, pp. 274-277, June 1974.

[3] K.D. Palmer, ”The Design of the Microstrip Grid Array”, Ph.D. dissertation, Dept. Elect. Eng., University of Stellenbosch, Western Cape, South Africa, 1997.

[4] R. Conti, J. Toth, T.Dowling, J.Weiss, “The Wire Grid Microstrip Antenna,” *IEEE Trans. Antennas Propogat.*, vol. AP-29, no. 1, pp. 157-166, Jan. 1981.

[5] P. Lopez, J.A. Rodriguez, F. Ares, and E. Moreno, “Subarray weighting for difference patterns of monopulse antennas: Joint optimization of subarray configurations and weights,” *IEEE Trans. Antennas Propogat.*, vol. 49, no. 11, pp. 1606-1608, Nov. 2001.

[6] T.S. Lee, T.K. Tseng, “Subarray-synthesized low-side-lobe sum and difference patterns with partial common weights”, *IEEE Trans. Antennas Propagat*., vol. 41, no. 6, pp.791-800, 1993

[7] D.A. McNamara, "Synthesis of sum and difference patterns for two-section monopulse arrays," *IEE Proc.*, vol. 135, no. 6, pp. 371-374, 1988.

[8] David K. Barton, Sergey A. Leonov, *Radar Technology Encyclopedia*, Norwood, MA: Artech House, 1998.

[9] Hao Wang, Da-Gang Fang, X.G. Chen, "A Compact Single Layer Monopulse Microstrip Antenna Array," *IEEE Trans. Antennas Propogat.*, vol. 54, no. 2, pp. 503-509, Feb. 2006.

[10] L.T. Hildebrandt, "The Analysis of Microstrip Wire grid Antenna Arrays", M.eng. dissertation, Dept. Elect. Eng., University of Pretoria, Gauteng, South Africa, 1992.

[11] Ramesh Garg, Prakash Bhartia, Inder Bahl, Apisak Ittipiboon, *Microstrip Antenna Design Handbook*, Norwood, MA: Artech House, 2001.

[12] R. Haupt, *Antenna Arrays A Computational Approach*, Hoboken, New Jersey: Wiley, 2010.

[13] D. Cheng, "Maximization of Directive Gains for Circular Arrays," *Proc. IEE*, vol. 114, no. 5, pp. 589-514, May 1967.

[14] D.A. McNamara, "On the synthesis of optimum monopulse antenna array distributions", Ph.D. dissertation, Dept. Eng., University of Cape Town, Western Cape, South Africa, 1986.

[15] E. Botha, "Contributions to the Synthesis of Planar and Conformal Arrays", Ph.D. dissertation, Dept. Elect. Eng., University of Pretoria, Gauteng, South Africa, 2000.

[16] J.R. Mohammed, "Synthesizing Sum and Difference Patterns with Low Complexity Feeding Network by Sharing Element Excitations", *International Journal of Antennas and Propagation*, vol. 2017, Article 2563901, Jan. 2017

[17] O. Einarsson, “Optimization of Planar Arrays”, *IEEE Trans. Antennas Propagat.*, vol. AP-27, no. 1, pp. 86-92, Jan. 1979.

[18] R. L. Haupt and W. H. Douglas, *Genetic Algorithms in Electromagnetics*, Hoboken, New Jersey: IEEE Press, 2007.

[19] R. L. Haupt and S. E. Haupt, *Practical Genetic Algorithms, second edition*, Hoboken, New Jersey: Wiley, 2004.